Spring 2024

Adaptive Control of an Aeroelastic System for Active Flutter Suppression and Disturbance Rejection

Patrick Sterling Downs
Embry-Riddle Aeronautical University, downsp1@my.erau.edu

ADAPTIVE CONTROL OF AN AEROELASTIC SYSTEM FOR ACTIVE FLUTTER SUPPRESSION AND DISTURBANCE REJECTION

By

Patrick Sterling Downs

A Dissertation Submitted to the Faculty of Embry-Riddle Aeronautical University

In Partial Fulfillment of the Requirements for the Degree of

Doctor of Philosophy in Aerospace Engineering

April 2024

Embry-Riddle Aeronautical University

Daytona Beach, Florida

ACKNOWLEDGMENTS

First, I would like to extend enormous appreciation to my advisor, Dr. Richard Prazenica, for his tremendous support, patience, and guidance throughout this process. His feedback and encouragement have been crucial in strengthening the quality of my work. In addition, Professor Glenn Greiner for recognizing my potential and providing me opportunities to succeed both academically and professionally throughout my career at Embry-Riddle. His mentorship has had a profound impact on shaping me into the engineer that I am today.

I would like to thank Dr. Hever Moncayo, Dr. K. Merve Dogan, Dr. Marc Compere, and Paul Taylor for their insightful comments and valuable suggestions on my work. Each member of my committee brought a unique perspective, enriching my understanding and elevating the quality of my work.

I would also like to acknowledge my friend Jacqueline Taylor who played an integral role in developing me as a writer and was a constant source of support. In addition, the countless number of friends and colleagues who have contributed in various capacities, whether through discussions, feedback, or simply supporting me through the ups and downs of this process.

Furthermore, I would like to express my appreciation to my family for their constant love, encouragement, and understanding throughout this journey. Their support has been essential to my perseverance and success.

Finally, my father Shawn. Although he is no longer with us, I am forever grateful for the passion for learning and the drive for excellence that he instilled within me from a young age. While he may not have been here to witness this journey, I know he is watching over me with pride.

ABSTRACT

The future of aircraft design strives for lighter weight, more aerodynamically efficient structures. These improvements may come with the drawback of increased structural flexibility and elevated aeroelastic effects, often resulting in a lower flutter speed. This motivates the implementation of advanced control methods to control aeroelastic systems over a range of flight conditions, suppress and delay the onset of flutter, and compensate for disturbances, actuator dynamics, and unmodeled nonlinear dynamics.

This dissertation first develops a novel method for constructing time-domain simulation models of two and three-dimensional aeroelastic systems, resulting in models that are suitable for the implementation of state-space control algorithms. Then, model reference adaptive control strategies are implemented on the aeroelastic systems with the objective of controlling these systems over a range of pre- and post-flutter flight conditions subject to disturbances, nonlinear dynamics, and actuator dynamics. To model the aeroelastic systems, the structural dynamics equations of motion are first developed for a two-dimensional pitch-plunge-flap airfoil section with nonlinear torsional stiffness, first- and second-order actuator dynamics, and actuator freeplay. This system utilizes quasi-steady aerodynamic forcing to develop an open-loop flutter model upon which direct model reference adaptive control is applied. Next, the structural dynamics equations of motion for a three-dimensional wing are developed using energy methods and modal solutions to the forced vibration problem. For the three-dimensional system, an unsteady vortex-lattice solver is implemented to calculate real-time unsteady aerodynamic forces and aerodynamic control force inputs. This is coupled with the flexible equations of motion to form the full aeroelastic equations of motion, which are then validated against a Nastran model. Finally, the elastic wing is coupled to a longitudinal -rigid body aircraft dynamics model to understand the relationship between rigid-body dynamics and flexible motion in the presence of a controller.

Direct model reference adaptive control (MRAC) strategies are then implemented on the two- and three-dimensional aeroelastic systems, and the performance is compared to

that obtained using a standard linear quadratic regulator (LQR). The simulation studies demonstrate that MRAC provides more effective aeroelastic control and flutter or limit-cycle oscillation suppression over a wider range of flight conditions compared to the standard LQR controller. In addition, the MRAC is shown to provide robustness to nonlinear stiffness, first-order and second-order actuator dynamics, and actuator freeplay. The effect of varying actuator bandwidth on the MRAC performance is studied for several cases, with the objective of determining minimum bandwidth requirements.

TABLE OF CONTENTS

LIST OF FIGURES

Figure **Page**

LIST OF TABLES

Table **Page**

1 Introduction

As aircraft manufacturers set more aggressive targets for payload, range, speed, and emissions, maximizing aerodynamic and structural efficiency becomes paramount. One solution that becomes immediately evident is reducing the structural weight of the airframe. This can be detrimental to the structural stiffness and consequently the flutter speed. Aeroelastic tailoring can be performed to optimize load paths and improve stiffness with minimal increase in weight, but this method can yield very complex structures that are not practical for manufacturing.

Another possible solution is using a control system to add artificial stiffness to the system as well as improve the damping characteristics. While there are a variety of controllers used in aeroelastic suppression, this research focuses on model-reference adaptive control. Using a reference model gives the control system designer flexibility to dictate the behavior of the system, independent of the flight condition. In addition, including adaptation in the control law can provide a level of fault tolerance to unmodeled dynamics, nonlinearities, and disturbances.

This dissertation describes the process required to develop aeroelastic models in a control-theoretic framework for time-domain simulation. This includes the derivation of the equations of motion for an aeroelastic typical section with linear stiffness, followed by the option to include nonlinear torsional stiffness, first-order actuator dynamics, second-order actuator dynamics, and actuator freeplay. Furthermore, the derivation of three-dimensional wing equations of motion for N modes of vibration are developed. For this three-dimensional case, aerodynamic forces are calculated using an unsteady vortex-lattice code, written so as to be integrated into the aeroelastic solution.

The first step in the aeroelastic solution sequence is understanding the structure. This requires knowledge of the unforced vibratory characteristics, i.e. the mode shapes, so the structure can be transformed into modal coordinates. One method for calculating structural mode shapes is an iterative solution to the eigenvalue problem posed by the unforced oscilla-

tory system. Flexibility influence coefficients are used in lieu of structural stiffness because in most cases they are more easily calculated.

The next step in the process is calculating the unsteady aerodynamic forces and moments. While Navier-Stokes solutions for fluid-structure interaction (FSI) problems do exist, the computation time can be orders of magnitude greater than more basic aerodynamic solution methods. Thus, less expensive computational approaches such as panel methods are used in this work.

While frequency-domain methods like doublet-lattice provide fast and accurate solutions, applying a control system in tandem with the aerodynamic solution is very limited. Due to the formulation of the aerodynamics, these solutions are only suitable for frequency based or classical controllers. In this case, opting for a more computationally expensive time-domain solution, such as time-marching unsteady vortex lattice, allows for any time-domain control system to be used.

After the dynamics of the structure are fully understood, a control system can be implemented. Due to the formulation of the model-reference adaptive controller, this research develops a time-domain implementation of the aeroelastic solution. Simple two-dimensional test cases will utilize quasi-steady aerodynamics, while the three-dimensional cases will utilize unsteady vortex-lattice aerodynamics. The solution process is illustrated in Figure 1.1.

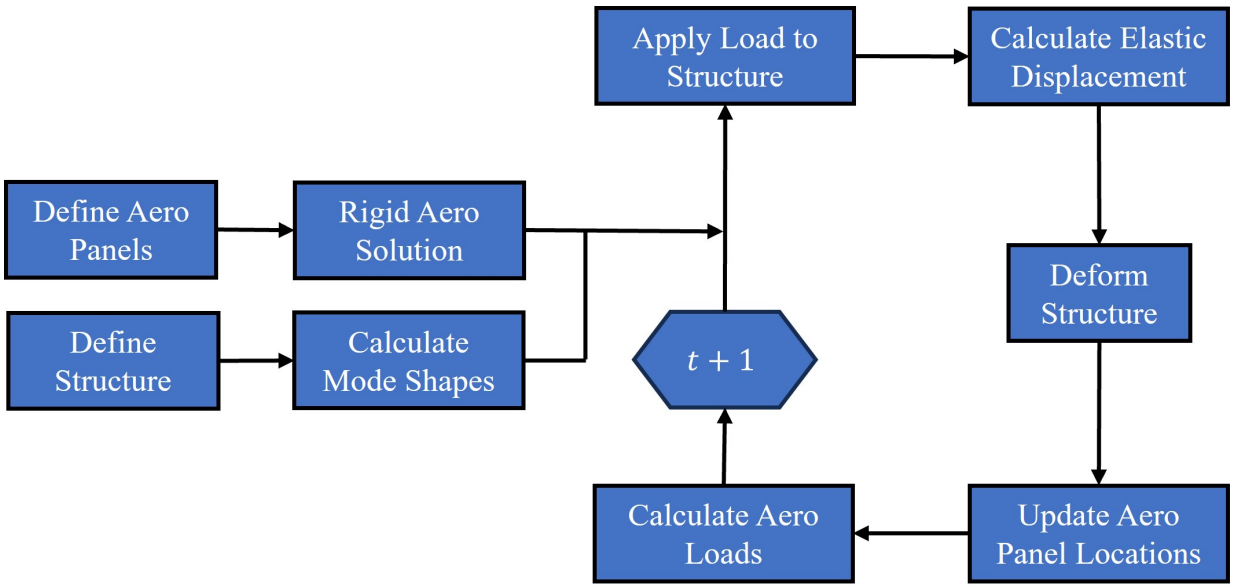

Figure 1.1 Solution Sequence for Three-Dimensional Aeroelastic System

To begin the solution sequence, the structure is defined as a lumped parameter system with structural cross section properties and mass properties defined at each station, allowing for computation of either the normal modes or uncoupled modes. This research utilizes the uncoupled modes of the system. Next, the edges of the lifting surface and its discretizations are defined so an unsteady vortex-lattice solution can be executed.

Once the mode shapes and aerodynamic panels are defined, the aeroelastic simulation can begin. Initially, a rigid solution is performed to establish the wake. Then, the steady-state elastic deformation of the structure is determined by simulating the structural dynamics, but with artificially high damping such that the structure quickly settles. Finally, a fully aeroelastic simulation is performed.

To incorporate more realism into the simulations, actuator freeplay, hardware limitations, and sensor requirements are included. Actuator freeplay allows for the evaluation of control system performance in the event the control surface is free to float. Hardware limitations such as first-order and second-order actuator dynamics are then implemented to allow for the evaluation of control system performance when delay between the input and actuator

response is introduced. Investigating sensor requirements provides insight into the number of sensors required and their placement such that enough information is available to the feedback controller.

1.1 Motivation

There exists a need for an active flutter suppression system that can be applied over a wide range of flight conditions. Using a model reference adaptive controller allows the engineer to dictate the behavior of the system regardless of flight condition. Implementing an adaptive control law provides a level of fault tolerance to unmodeled dynamics, nonlinearities, and disturbances.

1.2 Objectives

The primary objective of this work is to develop and implement adaptive control strategies for flutter and limit cycle oscillation (LCO) suppression, evaluate their performance over a range of airspeeds on a pitch-plunge aeroelastic model, and demonstrate their application to a flexible aircraft. Supporting objectives include:

- Develop a high-fidelity flexible wing model and flexible-wing aircraft using the unsteady vortex-lattice method for time domain simulation, and then validate the model using Nastran.

- Investigate and evaluate the performance of adaptive control strategies that are able to compensate for, and potentially estimate, unmodeled dynamics such as flexible dynamics, structural nonlinearities, actuator dynamics, and freeplay.

- Study the effects of actuator bandwidth on controller performance and assess mitigation strategies.

1.3 Dissertation Outline

The remainder of this dissertation is organized as follows: Chapter 2 discusses relevant literature, Chapter 3 derives the structural dynamics equations of motion, Chapter 4 develops

the unsteady vortex-lattice aerodynamics, Chapter 5 validates the aeroelastic model used for control law development, Chapter 6 formulates the direct model reference adaptive control law used in this research, Chapter 7 shows the results from two-dimensional and three-dimensional simulation studies, and Chapter 8 summarizes the work and provides concluding remarks.

2 Literature Review

This chapter reviews the literature in several key areas related to this research. This includes; structural dynamics, aerodynamic modeling, aeroelastic systems, flutter suppression, and control systems.

2.1 Structural Dynamics Modeling

Bisplinghoff, Ashley, and Halfman (BAH) [1] describe the use of Euler-Bernoulli beam bending theory to develop flexibility influence coefficients for a tapered cantilevered beam. Scanlan and Rosenbaum [3] discuss various energy methods that can be used to develop flexbility influence coefficients for more complex structures such as an aircraft empennage.

Once the flexibility influence coefficients are known, the mode shapes and frequencies can be calculated. The method used to calculate the mode shapes is introduced by Flomenhoft [4] in which an iterative matrix solution is presented to solve the structural dynamics eigenvalue problem. Clough and Penzien discuss extensions of this method as well as its limitations in calculating the structural dynamic characteristics of the given structure [5].

2.2 Aerodynamic Modeling

One of the first theories of unsteady aerodynamics was introduced by Theodorsen in NACA TR 496 [6]. This work was expanded to include an aerodynamically balanced flap by Theodorsen and Garrick in NACA TR 736 [7]. Smilg and Wasserman built on the works of Theodorsen and Garrick to include an unbalanced flap in [8], as well as developing complex coefficients to help describe the oscillatory motion of an airfoil in incompressible flow.

The equations that describe compressible unsteady flow that use perturbation velocity potential is discussed in [1]. Another method for direct computation of unsteady aerodynamic coefficients for compressible flow utilizes kernel function approximations as described in [9]. Concurrently, Ashley and Zartarian created Piston Theory, a method that uses the integration of isentropic pressure waves to calculate the unsteady airloads for an airfoil in supersonic flow [10].

For three-dimensional lifting surfaces, various forms of panel methods exist. Katz and Plotkin describe many of the vortex based solutions for subsonic flows in [2]. Albano and Rodden introduce doublet-lattice lattice method for solving unsteady flow problems in [11],

2.3 Aeroelastic Systems and Flutter Suppression

Various flutter solutions exist including the k-method, p-method, pk-method, and augmented states method [12]. The k-method assumes the system is oscillating with simple-harmonic motion and the aerodynamic forces are calculated for a range of reduced frequencies [13]. The p-method assumes the system is oscillating at some reduced frequency k, and decay rate specified by the complex eigenvalue $p = \gamma + ik$. The pk-method is a combination of the two methods and assumes a p-method solution for the structural dynamics and a k-method solution for the unsteady aerodynamics [14]. The augmented states method utilizes rational function approximations of the unsteady aerodynamic forcing, which allows for direct computation of the airloads at specified reduced frequencies. These rational function approximations (RFAs) are defined in the Laplace domain and allow for a root locus or frequency-based solution [15].

2.4 Control Systems

There are few instances of control methods for active flutter suppression being applied in practice. One of the earliest was a modified B-52 which used additional control surfaces to suppress a 2.4Hz flutter mode. More recently, the Boeing 787-10 employed a system to add artificial damping to a poorly damped symmetric wing/nacelle/fuselage mode. Although this case is not classified as active flutter suppression, it uses a control system to increase damping.

The first step in understanding the flutter characteristics and dynamic response of a vehicle is modeling both the rigid body and flexible dynamics. The processes for deriving the equations of motion for an aeroelastic typical section are well understood and can be found in literature such as Bisplinghoff et al. [1] and Fung [13]. However, the most common methods for flutter solutions are frequency based, such as the pk-method as described by

Hodges and Pierce in [16], for which the mathematical models do not lend themselves to feedback control development.

The rigid body dynamics are modeled using the nonlinear aircraft equations of motion in [17]. The flexible or elastic dynamics begin with the equations of motion for an aeroelastic typical section as introduced by Theodorsen [18]. Then, a modal weighting process, similar to the Rayleigh type flutter solution method, is used to form dynamics that represent a finite span wing, which is described in [1] and [3]. This process requires prior knowledge of the system's modes of vibration or the use of assumed modes. In this analysis, the mode shapes and frequencies are calculated using a matrix iteration process first introduced by Flomenthoft in [4] with extensions in [5]. This method utilizes flexibility influence coefficients that are calculated using unit load analysis and Euler-Bernoulli beam bending theory [1]. Alternative methods for determining the uncoupled modes of the system include: Rayleigh Energy, Rayleigh-Ritz, Stodola, Holzer, and Myklestad [3].

Haddadpour and Firouz-Abadi show the Rayleigh type modal weighting method of extending an aeroelastic typical section and evaluate the flutter characteristics for unsteady and quasi-steady aerodynamics [19]. Unsteady aerodynamic formulations are not amenable to direct time domain simulation due to their frequency dependence. This introduces the need for rational function approximations such as Roger's Approximation [20]. Karpel discusses other methods for rational function approximations including linear least-squares, the minimum-state method, and Padé approximations in [15].

The final modeling step is to combine the rigid body equations of motion with those of the flexible wing. Butrill et al. derive the equations of motion for a flexible aircraft in maneuvering flight [21]. However, the authors employed a mean axis system that decoupled the elastic motion from the rigid body motion. Waszak and Schmidt develop the equations of motion in a similar fashion but incorporate aerodynamic strip theory to derive closed form integral solutions of generalized forces.

Once the system dynamics are fully described, an adaptive controller can be employed.

Initially, a direct model reference adaptive control algorithm is used following the process described by Behal et al. [22] and Nguyen [23].

Other adaptation algorithms were also studied, as many have shown promise in aeroelastic control. Ko et al. use a linearized partial feedback adaptive controller to provide an unstable nonlinear pitch-plunge system with local asymptotic stability [24]. Behal et al. show that a nonlinear adaptive output feedback controller is effective in suppressing limit-cycle oscillation (LCO) flutter of a two dimensional lifting surface in [22]. Adrighettoni and Mantegazza develop a multi-input, multi-output (MIMO) adaptive flutter suppression system for a wing with leading-edge and trailing-edge control surfaces [25]. The stabilizing controller uses a full-state eigenstructure design method and shows a significant increase in aeroelastic damping and flutter speed. Mattaboni et al. show that a recurrent neural network can be used to improve the boundaries of the flutter free envelope by 15%. In this case, the modeling approach involved a finite element stick model with doublet-lattice aerodynamics panels [26].

The ride quality aspect is discussed by Nyugen in [27] where a multi-objective cost function is used to develop a single control system that provides stability augmentation, flutter suppression, and load alleviation. Leatherwood et al. quantify ride quality in [28] where the authors discuss the ranges for lateral and vertical vibration that cause the greatest level of passenger discomfort. While low frequency vibrations tend to go unnoticed, vertical vibration near 18Hz cause the greatest level of passenger discomfort [27].

There are instances of adaptive control algorithms implemented on aeroelastic systems, a basic example being that of Behal et al. who used partial state feedback of a linear model to drive the pitch displacement to a set point while only using measurements of the pitch state in the controller [22]. Li et al. use an $\mathcal{L}_1$ adaptive controller to suppress LCO of an airfoil with two structural nonlinearities [29]. Zeng and Singh show the success of a variable structure model reference adaptive control in tracking a reference model under stable conditions [30]. Zhang et al. show that for a 4-DOF airfoil subjected to unsteady airloads, a partial state feedback adaptive controller drastically reduced settling time of the system for $V < V_f$ and

stabilized the system for $V > V_f$, where V_f is the flutter speed [31]. Nguyen et al. present the use of an adaptive linear-quadratic-Gaussian controller to suppress unstable aeroelastic modes on a reduced order aircraft model at two points in the flight envelope [32].

3 Dynamic Modeling

This chapter discusses the dynamics modeling efforts of this research. This includes a two-dimensional pitch-plunge-flap airfoil section, a three-dimensional elastic wing model, and the development of rigid-body aircraft equations of motion with their coupling to the elastic wing. This chapter also outlines the implementation of a nonlinear torsional stiffness and actuator freeplay.

The equations of motion for an aeroelastic typical section are derived using energy methods. In this analysis, given N degrees-of-freedom, Lagrange's Equation takes the form

$$\frac{d}{dt}\left(\frac{\partial \mathcal{L}}{\partial \dot{\xi}_i}\right) - \left(\frac{\partial \mathcal{L}}{\partial \xi_i}\right) = Q_i \qquad\qquad i = 1, \cdots, N \tag{3.1}$$

where $\mathcal{L}$ is the Lagrangian of the system, ξ_i are the generalized coordinates, and Q_i are generalized non-conservative forces or moments. The Lagrangian $\mathcal{L}$ is the difference between the kinetic energy of the system T and the potential energy of the system V. Mathematically this is given by

$$\mathcal{L} = T - V \tag{3.2}$$

The kinetic energy of the system is purely dependent on generalized rates and the potential energy is purely dependent on generalized displacements. Therefore, Equation (3.1) can be written as

$$\frac{d}{dt}\left(\frac{\partial T}{\partial \dot{\xi}_i}\right) + \left(\frac{\partial V}{\partial \xi_i}\right) = Q_i \tag{3.3}$$

which results in N linear differential equations that describe the dynamics of a given system. For an aeroelastic typical section, this will result in three coupled equations; one that describes the plunging motion, one that describe the pitching motion, and one that describes the flap motion.

3.1 Simplified Airfoil Model

This section discusses the modeling of a two-dimensional pitch-plunge-flap airfoil section. As detailed in Chapter 2, many different implementations of the two-dimensional pitch-plunge airfoil section exist. The classical formulation is first presented by Theodorsen in NACA TR-496 [6], expanded in NACA TR-736 [7], and further developed by Smilg and Wasserman in ACTR 4798 [8] to include an unsealed gap. This work uses the symbols and nomenclature consistent with that of Theodorsen with the addition of a nonlinear torsional stiffness term $k_\alpha(\alpha)$. Figure 3.1 shows the typical section used in this research.

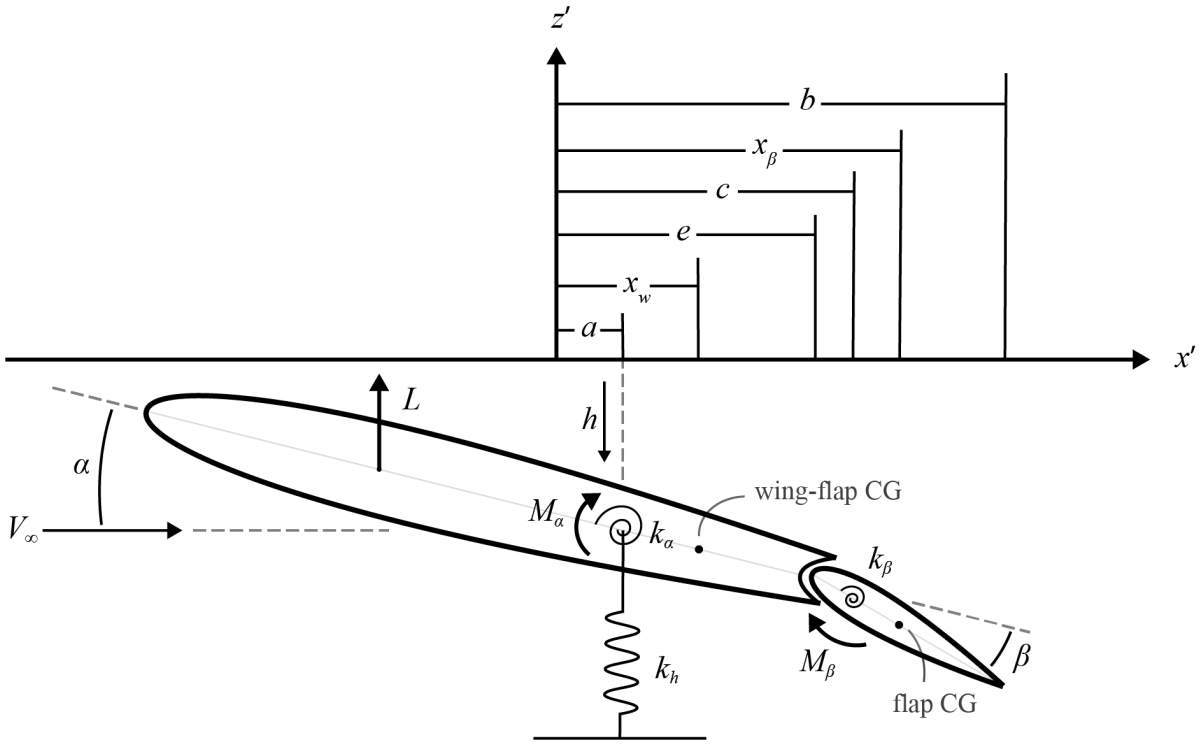

Figure 3.1 Typical Section with Unsealed Gap

The origin is defined at the midchord with the positive x' direction in the direction of flow and the leading edge is located at $-b$ in the x' direction. The lengths shown in Figure 3.1 are non-dimensionalized with respect to the semichord b. The parameters in Figure 3.1 are as follows: a is the non-dimensional distance from the origin to the elastic axis; x_w is the non-dimensional distance from the origin to the center of gravity of the wing-flap system; e is

the non-dimensional distance from the origin to the flap break point; c is the non-dimensional distance from the origin to the flap hinge line; x_β is the non-dimensional distance from the origin to the center of gravity of the flap; and β is flap deflection.

The section is constrained such that it can oscillate in the z' direction and rotate in the $x'-z'$ plane. A linear spring with stiffness k_h simulates bending stiffness, a linear or nonlinear torsional spring with stiffness $k_\alpha(\alpha)$ simulates torsional stiffness, and a linear torsional spring with stiffness k_β simulates the flap stiffness. Positive plunge h is defined in the negative z' direction, positive pitch α is defined as leading-edge upward, and positive flap angle β is defined as flap trailing-edge downward.

Now the equations of motion that describe the typical section are derived using Eq. (3.3). The vertical position of a point on the wing section is given by

$$z_w(t) = -\left(h(t)\, b\right) - b\left(x' - a\right)\alpha(t) \tag{3.4}$$

The position of a point on the flap section in the airfoil coordinate frame is given by

$$z_f(t) = -\left(h(t)\, b\right) - b\left(c - a\right)\alpha(t) - b\left(x' - c\right)\left(\alpha(t) + \beta(t)\right) \tag{3.5}$$

The kinetic energy of the wing section is

$$T_w(t) = \int_0^{be} \rho_w(x')\, \dot{z}_w^2(t)\, dx' \tag{3.6}$$

where $\rho_w(x')$ is the wing section mass per unit length. Evaluating and simplifying yields

$$T_w(t) = \frac{1}{2} m_w b^2 \dot{h}^2(t) + \frac{1}{2} I_w \dot{\alpha}^2(t) + b S_w \dot{h}(t)\dot{\alpha}(t) \tag{3.7}$$

The kinetic energy of the flap section is

$$T_f(t) = \int_{be}^{b} \rho_\beta(x')\, \dot{z}_f^2(t)\, dx' \tag{3.8}$$

Evaluating and simplifying yields

$$T_f(t) = \tfrac{1}{2} m_f b^2 \dot{h}^2(t) + \tfrac{1}{2} I_f \dot{\alpha}^2(t) + \tfrac{1}{2} I_\beta \dot{\beta}^2(t) + b S_f \dot{h}(t)\dot{\alpha}(t) + b S_\beta \dot{h}(t)\dot{\beta}(t) + P_{\alpha\beta}\dot{\alpha}(t)\dot{\beta}(t) \tag{3.9}$$

Then, the total kinetic energy of the wing-flap system is

$$T(t) = T_w(t) + T_f(t) \tag{3.10}$$

In general, the potential energy is a result of elastic energy stored in the system by the structure. For the two-dimensional system, the energy is stored in the springs. Therefore, the potential energy of the wing-flap system is

$$V(t) = \frac{1}{2} k_h h^2(t) + \frac{1}{2} k_\alpha^2(t, \alpha) + \frac{1}{2} k_\beta \beta^2(t) \tag{3.11}$$

Applying Eq. (3.3) yields the following equations of motion for an airfoil section:

$$m b \ddot{h}(t) + S_\alpha \ddot{\alpha}(t) + S_\beta \ddot{\beta}(t) + k_h b h(t) = Q_h(t) \tag{3.12}$$

$$S_\alpha b \ddot{h}(t) + I_\alpha \ddot{\alpha}(t) + [I_\beta + S_\beta b(c-a)]\, \ddot{\beta}(t) + k_\alpha \alpha(t) = Q_\alpha(t) \tag{3.13}$$

$$S_\beta b \ddot{h}(t) + [I_\beta + S_\beta b(c-a)]\, \ddot{\alpha}(t) + I_\beta \ddot{\beta}(t) + k_\beta \beta(t) = Q_\beta(t) \tag{3.14}$$

where $Q_h(t)$, $Q_\alpha(t)$, and $Q_\beta(t)$ are the generalized non-conservative forces due to the plunge, pitch, and flap degrees-of-freedom respectively. Furthermore, the wing section mass per unit span is defined as

$$m'_w = \int_{-b}^{be} \rho_w(x')\, dx' \tag{3.15}$$

The wing section static moment per unit span about the elastic axis is defined as

$$S'_w = \int_{-b}^{be} b\,(x' - a)\rho_w(x')\,dx' \tag{3.16}$$

The wing section mass moment of inertia per unit span about the elastic axis is defined as

$$I'_w = \int_{-b}^{be} b^2\,(x' - a)^2\rho_w(x')\,dx' \tag{3.17}$$

The flap section mass per unit span is defined as

$$m'_\beta = \int_{be}^{b} \rho_\beta(x')\,dx' \tag{3.18}$$

The flap section static moment per unit span about the hinge line is defined as

$$S'_\beta = \int_{be}^{b} b\,(x' - c)\,\rho_\beta(x')\,dx' \tag{3.19}$$

The flap section mass moment of inertia per unit span about the hinge line is defined as

$$I'_\beta = \int_{be}^{b} b^2\,(x' - c)^2\,\rho_\beta(x')\,dx' \tag{3.20}$$

The flap section static moment per unit span about the elastic axis is defined as

$$S'_f = \int_{be}^{b} b\,[(c - a) + (x' - c)]\rho_\beta(x')\,dx' \tag{3.21}$$

or

$$S'_f = \int_{be}^{b} b\,(x' - a)\rho_\beta(x')\,dx' \tag{3.22}$$

The flap mass moment of inertia per unit span about the elastic axis is defined as

$$I'_f = \int_{be}^{b} b^2\,[(c - a) + (x' - c)]^2\rho_\beta(x')\,dx' \tag{3.23}$$

or

$$I'_f = \int_{be}^{b} b^2 \, (x' - a) \rho_\beta(x') \, dx' \tag{3.24}$$

The flap rotational imbalance is defined as

$$P'_{\alpha\beta} = \int_{be}^{b} (I_\beta + b(c - a) S_\beta) \, dx' \tag{3.25}$$

The total typical section mass per unit span is defined as

$$m' = m'_w + m'_f \tag{3.26}$$

The total typical section static moment per unit span about the elastic axis is defined as

$$S'_\alpha = S'_w + S'_f \tag{3.27}$$

The total typical section mass moment of inertia per unit span about the elastic axis is defined as

$$I'_\alpha = I'_w + I'_f \tag{3.28}$$

Next, the non-conservative forces Q must be considered. For each mode, these forces are

$$Q_h(t) = -c_h \dot{h}(t) - L_e(t) \tag{3.29}$$

$$Q_\alpha(t) = -c_\alpha \dot{\alpha}(t) + M_e(t) \tag{3.30}$$

$$Q_\beta(t) = -c_\beta \dot{\beta}(t) + T_e(t) \tag{3.31}$$

where c_h is the plunge damping coefficient, c_α is the pitch damping coefficient, c_β is the flap damping coefficient, L_e is the section lift, M_e is the section pitching moment, and T_e is the section hinge moment. Substituting the generalized forces into Eq. (3.12) through Eq.

(3.14) gives the full set of equations that describe the pitch-plunge-flap airfoil dynamics:

$$mb\ddot{h}(t) + S_\alpha \ddot{\alpha}(t) + S_\beta \ddot{\beta}(t) + c_h \dot{h}(t) + k_h bh(t) = -L_e(t) \tag{3.32}$$

$$S_\alpha b\ddot{h}(t) + I_\alpha \ddot{\alpha}(t) + P_{\alpha\beta} \ddot{\beta}(t) + c_\alpha \dot{\alpha}(t) + k_\alpha \alpha(t) = M_e(t) \tag{3.33}$$

$$S_\beta b\ddot{h}(t) + P_{\alpha\beta} \ddot{\alpha}(t) + I_\beta \ddot{\beta} + c_\beta \dot{\beta}(t) + k_\beta \beta(t) = T_e(t) \tag{3.34}$$

which can be written in matrix form as:

$$\begin{bmatrix} m & S_\alpha & S_\beta \\ S_\alpha & I_\alpha & P_{\alpha\beta} \\ S_\beta & P_{\alpha\beta} & I_\beta \end{bmatrix} \begin{Bmatrix} \ddot{h}_e \\ \ddot{\alpha}_e \\ \ddot{\beta} \end{Bmatrix} + \begin{bmatrix} c_h & 0 & 0 \\ 0 & c_\alpha & 0 \\ 0 & 0 & c_\beta \end{bmatrix} \begin{Bmatrix} \dot{h}_e \\ \dot{\alpha}_e \\ \dot{\beta} \end{Bmatrix} + \begin{bmatrix} k_h & 0 & 0 \\ 0 & k_\alpha(\alpha_e) & 0 \\ 0 & 0 & k_\beta \end{bmatrix} \begin{Bmatrix} h_e \\ \alpha_e \\ \beta \end{Bmatrix} = \begin{bmatrix} -L_e \\ M_e \\ T_e \end{bmatrix} \tag{3.35}$$

As the primary focus of this research is the control law development, to simplify the model, it is assumed that the flap is dynamically decoupled from the wing dynamics. In addition, it is assumed that the flap is infinitely stiff such that there are no associated elastic modes. The resulting system of equations is:

$$\begin{bmatrix} m & S_\alpha & 0 \\ S_\alpha & I_\alpha & 0 \\ 0 & 0 & I_\beta \end{bmatrix} \begin{Bmatrix} \ddot{h}_e \\ \ddot{\alpha}_e \\ \ddot{\beta} \end{Bmatrix} + \begin{bmatrix} c_h & 0 & 0 \\ 0 & c_\alpha & 0 \\ 0 & 0 & c_\beta \end{bmatrix} \begin{Bmatrix} \dot{h}_e \\ \dot{\alpha}_e \\ \dot{\beta} \end{Bmatrix} + \begin{bmatrix} k_h & 0 & 0 \\ 0 & k_\alpha(\alpha_e) & 0 \\ 0 & 0 & k_\beta \end{bmatrix} \begin{Bmatrix} h_e \\ \alpha_e \\ \beta \end{Bmatrix} = \begin{bmatrix} -L_e \\ M_e \\ T_e \end{bmatrix} \tag{3.36}$$

Written more compactly, Eq. (3.36) becomes

$$[M_s]\,\underline{\ddot{x}} + [C_s]\,\underline{\dot{x}} + [K_s]\,\underline{x} = \underline{F} \tag{3.37}$$

where $[M_s]$ is the structural mass matrix, $[C_s]$ is the structural damping matrix, $[K_s]$ is the structural stiffness matrix, and $\underline{F}$ is a vector of aerodynamic forces. The aerodynamic forcing

can be written in terms of the elastic displacements and rates

$$\underline{F} = [M_a]\,\underline{\ddot{x}} + [C_a]\,\underline{\dot{x}} + [K_a]\,\underline{x} + \underline{F}_\delta \delta \tag{3.38}$$

where $[M_a]$ is the aerodynamic apparent mass matrix, $[C_a]$ is the aerodynamic damping matrix, $[K_a]$ is the aerodynamic stiffness matrix, and $\underline{F}_\delta$ is a vector of aerodynamic forces due to the commanded flap deflection δ. Combining Eq. (3.36) and Eq. (3.38) gives the following:

$$[[M_s] - [M_a]]\,\underline{\ddot{x}} + [[C_s] - [C_a]]\,\underline{\dot{x}} + [[K_s] - [K_a]]\,\underline{x} = \underline{F}_\delta \delta \tag{3.39}$$

where the structural mass matrix is

$$[M_s] = \begin{bmatrix} m & mbx_\alpha & 0 \\ mbx_\alpha & I_\alpha & 0 \\ 0 & 0 & I_\beta \end{bmatrix} \tag{3.40}$$

the structural damping matrix is

$$[C_s] = \begin{bmatrix} c_h & 0 & 0 \\ 0 & c_\alpha & 0 \\ 0 & 0 & c_\beta \end{bmatrix} \tag{3.41}$$

and the structural stiffness matrix is

$$[K_s] = \begin{bmatrix} k_h & 0 & 0 \\ 0 & k_\alpha(\alpha_e) & 0 \\ 0 & 0 & k_\beta \end{bmatrix} \tag{3.42}$$

For quasi-steady airloads, the aerodynamic apparent mass matrix is

$$[M_a] = \begin{bmatrix} 0 & 0 & 0 \\ 0 & 0 & 0 \\ 0 & 0 & 0 \end{bmatrix} \tag{3.43}$$

the aerodynamic damping matrix in coefficient form is

$$[C_a] = \rho U^2 \begin{bmatrix} \frac{b}{U} C_{l_\alpha} & \left(\frac{1}{2} - a\right) \frac{b^2}{U} C_{l_\alpha} & 0 \\ \frac{b^2}{U} C_{m_\alpha} & \left(\frac{1}{2} - a\right) \frac{b^3}{U} C_{m_\alpha} & 0 \\ \frac{b^2}{U} C_{h_\alpha} & \left(\frac{1}{2} - a\right) \frac{b^3}{U} C_{h_\alpha} & 0 \end{bmatrix} \tag{3.44}$$

the aerodynamic stiffness in coefficient form is

$$[K_a] = \rho U^2 \begin{bmatrix} 0 & bC_{l_\alpha} & bC_{l_\beta} \\ 0 & b^2 C_{m_\alpha} & b^2 C_{m_\beta} \\ 0 & b^2 C_{h_\alpha} & b^2 C_{h_\beta} \end{bmatrix} \tag{3.45}$$

and the aerodynamic forcing vector in coefficient form is

$$[F_\delta] = \rho U^2 \begin{bmatrix} bC_{l_\delta} \\ b^2 C_{m_\delta} \\ b^2 C_{h_\delta} \end{bmatrix} \tag{3.46}$$

Next, the two-dimensional dynamics are expanded to represent a three-dimensional wing using a modal weighting technique.

3.2 Structural Dynamics

The method for determining the uncoupled modes of a simplified beam is provided in [33]. The following section restates that work with some minor modifications and is included for completeness. The elastic deformation of the wing can be decomposed into a finite set of

uncoupled bending (ϕ_{h_e}) and torsional (ϕ_{α_e}) modes

$$h_e(y,t) = \sum_{i=1}^{N_h} h_{e_i}(t)\phi_{h_{e_i}}(y) \tag{3.47}$$

$$\alpha_e(y,t) = \sum_{j=1}^{N_\alpha} \alpha_{e_j}(t)\phi_{\alpha_{e_j}}(y) \tag{3.48}$$

where N_h is the number of uncoupled bending modes to be considered in the analysis and N_α is the number of uncoupled torsional modes to be considered in the analysis. These mode shapes are orthogonal such that

$$\phi_{h_{e_m}}^\top \phi_{h_{e_n}} = 0 \qquad \forall \;\; m \neq n$$

and

$$\phi_{\alpha_{e_m}}^\top \phi_{\alpha_{e_n}} = 0 \qquad \forall \;\; m \neq n$$

The mode shapes are calculated using beam flexibility influence coefficients and a matrix iteration process.

For a highly swept wing, the bending and torsion may be strongly coupled. In this case, using uncoupled bending and torsion modes in the elastic analysis can lead to a loss of accuracy. For a strongly coupled system, the elastic deformation can be decomposed into a finite set of normal modes (ϕ_i) such that

$$\eta(y,t) = \sum_{i=1}^{N} \eta_i(t)\phi_i(y) \tag{3.49}$$

where η_i is the ith normal displacement and ϕ_i is the ith normal mode shape. The mode shapes are orthogonal such that

$$\phi_i^\top \phi_j = 0 \qquad \forall \;\; i \neq j$$

The same matrix iteration process can be used to determine the normal modes, with the difference being the normal mode ϕ_i contains all the bending and torsional displacements whereas the uncoupled modes $\phi_{h_{e_i}}$ and $\phi_{\alpha_{e_i}}$ contain only bending and only torsion respectively.

3.3 Mode Shape Determination

The coupled frequencies and mode shapes of the structure are determined using the matrix iteration method for a lumped parameter system developed by Flomenhoft [4]. To determine the modes using this method, the flexibility influence coefficients of each structural component are required. Bisplinghoff, Ashley, and Halfman [1] present the process for deriving the influence coefficients as they discuss the deformation of an elastic airplane under static loads. The following section outlines their method for determining the flexibility influence coefficients of an elastic airplane subjected to a combination of generalized forces. Under the assumption that the structure is perfectly elastic, the deflections of an aircraft under static load can be represented by the linear system

$$\{q\} = [C]\{Q\} \tag{3.50}$$

where $\{Q\}$ is a vector of applied forces, $[C]$ is a matrix of proportionality constants, and $\{q\}$ is a vector of the resulting deflections. Since the system is linear, superposition applies. This means the total deflection of a given point can be written as the sum of deflections caused by the individual forces and moments. Under the assumption of superposition, $\{Q\}$ now represents generalized forces and $\{q\}$ represents generalized coordinates. Eq. (3.50) can then be written as a summation of n generalized forces weighted by their corresponding flexibility influence coefficients, C_{ij}, as follows

$$q_i = \sum_{j=1}^{n} C_{ij} Q_j \qquad (i = 1, 2, \cdots, n) \tag{3.51}$$

Alternatively, the forces can be expressed as functions of displacement by

$$Q_i = \sum_{j=1}^{n} k_{ij} q_j \qquad (i = 1, 2, \cdots, n) \tag{3.52}$$

where k_{ij} are stiffness influence coefficients. Eq. (3.51) and Eq. (3.52) can be written in matrix notation as follows

$$\{q\} = [C]\{Q\} \tag{3.53}$$

$$\{Q\} = [k]\{q\} \tag{3.54}$$

Thus, the stiffness influence coefficients $[k]$ and flexibility influence coefficients $[C]$ are related by the following:

$$[k] = [C]^{-1} \tag{3.55}$$

In most cases, finding the stiffness influence coefficients is a much more involved process than that of finding the flexibility influence coefficients; thus, determining the flexibility influence coefficients is the more common method [1].

The flexibility influence coefficients of a slender wing, as described by Bisplinghoff et al. [1], are found by applying a unit load and unit torque along the structure's elastic axis at location η and measuring the response at location y. Figure 3.2 shows the variable designations for a straight tapered wing, with its elastic axis aligned with the Y axis.

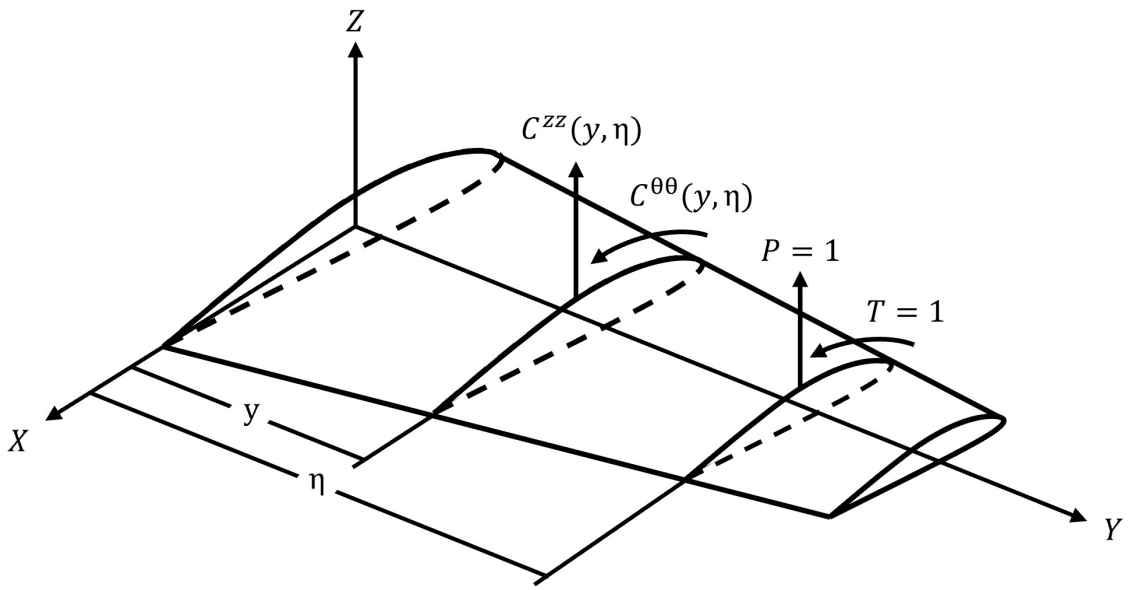

Figure 3.2 Straight Wing Subjected to Unit Load and Torque [1]

For a straight tapered wing with loads applied to the elastic axis and moments about the elastic axis, it is known that there is no bending deflection due to an applied torque and no torsion due to an applied point load. Therefore, the only influence coefficients that need to be calculated are $C^{zz}(y,\eta)$ and $C^{\theta\theta}(y,\eta)$, where $C^{zz}(y,\eta)$ is the bending influence coefficient at y due to a unit load at η and $C^{\theta\theta}(y,\eta)$ is the torsional influence coefficient at y due to a unit torque at η. Bisplinghoff et al. [1] derived the influence coefficients for a straight tapered wing using strain energy. For the case of $\eta \geq y$, the bending influence coefficients are

$$C^{zz}(y,\eta) = \int_0^y \frac{(\eta-\lambda)\,(y-\lambda)}{EI} d\lambda + \int_0^y \frac{d\lambda}{GK} \qquad (\eta \geq y) \tag{3.56}$$

and when $y > \eta$

$$C^{zz}(y,\eta) = \int_0^\eta \frac{(\eta-\lambda)\,(y-\lambda)}{EI} d\lambda + \int_0^\eta \frac{d\lambda}{GK} \qquad (y > \eta) \tag{3.57}$$

In Eqs. (3.56) and (3.57), the first integral represents the deflection due to bending stress and the second integral represents the deflection due to transverse shear stress. Next, the

torsional influence coefficients are defined by BAH. For the case of $\eta \geq y$, the torsional influence coefficients are

$$C^{\theta\theta}(y,\eta) = \int_0^y \frac{d\lambda}{GJ} \qquad (\eta \geq y) \tag{3.58}$$

and when $y > \eta$

$$C^{\theta\theta}(y,\eta) = \int_0^\eta \frac{d\lambda}{GJ} \qquad (y > \eta) \tag{3.59}$$

where in Eqs. (3.56) through (3.59), EI represents the bending stiffness of the structure, GJ represents the torsional stiffness, and GK represents the shear stiffness. In general, the complete set of influence coefficients is defined as

$$[C] = \left[\begin{array}{c:c} C^{zz} & C^{z\theta} \\ \hdashline C^{\theta z} & C^{\theta\theta} \end{array}\right] \tag{3.60}$$

where C^{zz} is a matrix of bending influence coefficients due to point loads, $C^{z\theta}$ is a matrix of bending influence coefficients due to moments, $C^{\theta z}$ is a matrix of rotational influence coefficients due to point loads, and $C^{\theta\theta}$ is a matrix of rotational influence coefficients due to moments.

For an unswept wing, the bending and torsion are largely independent of one another. In other words, a point load on the beam does not cause torsion and torque on the beam does not cause bending. Mathematically, this means that $C^{z\theta} = C^{\theta z} = 0$. For this case, the deformation of the wing is treated as two separate problems: a beam bending-only problem; and a beam torsion-only problem. For beams in which the cross-sectional dimensions are small in comparison to the length, i.e. slender beams, the deformations due to transverse shear may be neglected [1]. Then, Euler-Bernoulli beam bending theory is used to determine the deflection and slope of the cantilevered beam under an applied load. Figure 3.3 shows a cantilevered beam with bending stiffness EI that varies along its length. A point load P is applied at location ξ while the displacement w and slope w' are determined at location x.

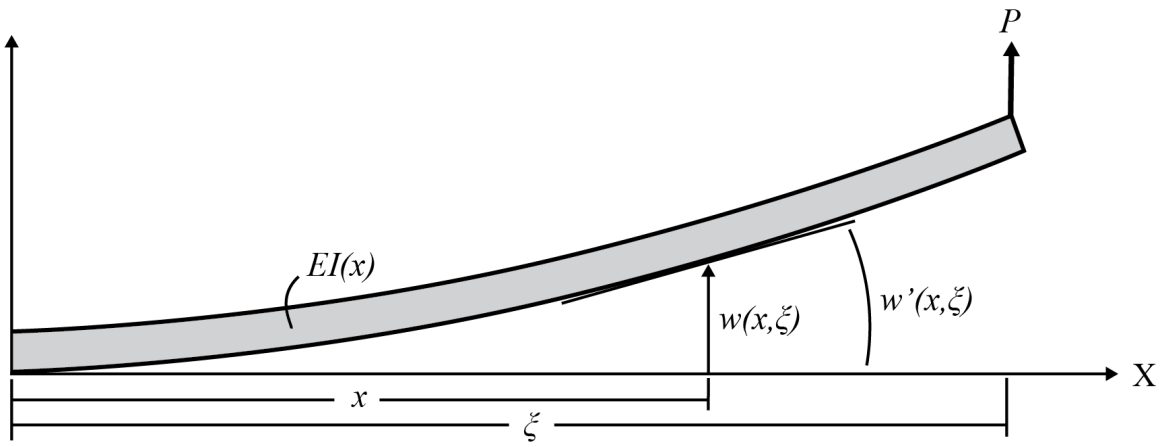

Figure 3.3 Displacement and Slope due to an Applied Load

Strain energy theory is used to determine the rotation of the beam under an applied torque. Figure 3.4 shows a cantilevered beam with torsional stiffness GJ that varies along its length. A torque T is applied at location ξ while the rotation θ is determined at location x.

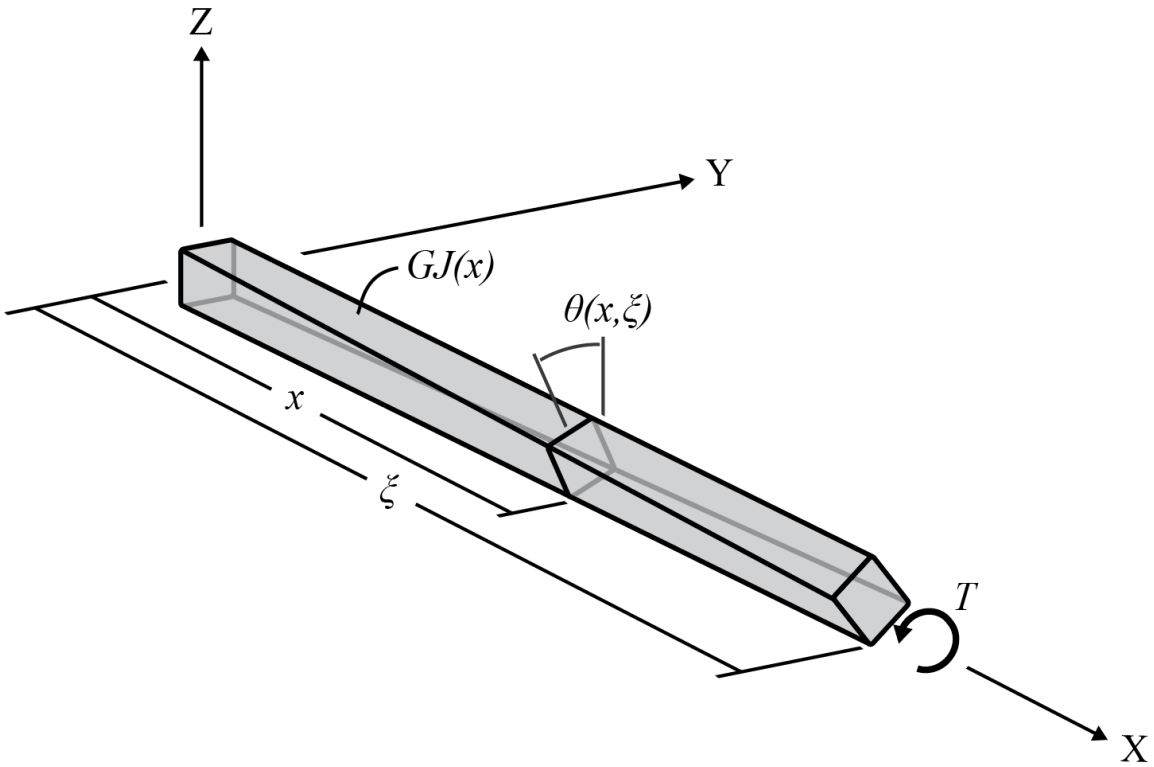

Figure 3.4 Torsion due to an Applied Moment

In many cases, structural data may only be available for discrete parameters that describe the mass properties and section inertial properties. A beam with varying section properties can be idealized as a series of constant cross section beams. Figure 3.5 is a visualization of this representation. This shows a beam discretized into N segments, each with constant EI and GJ. For a sufficiently large number of segments, the properties of the discretized beam become representative of a tapered beam.

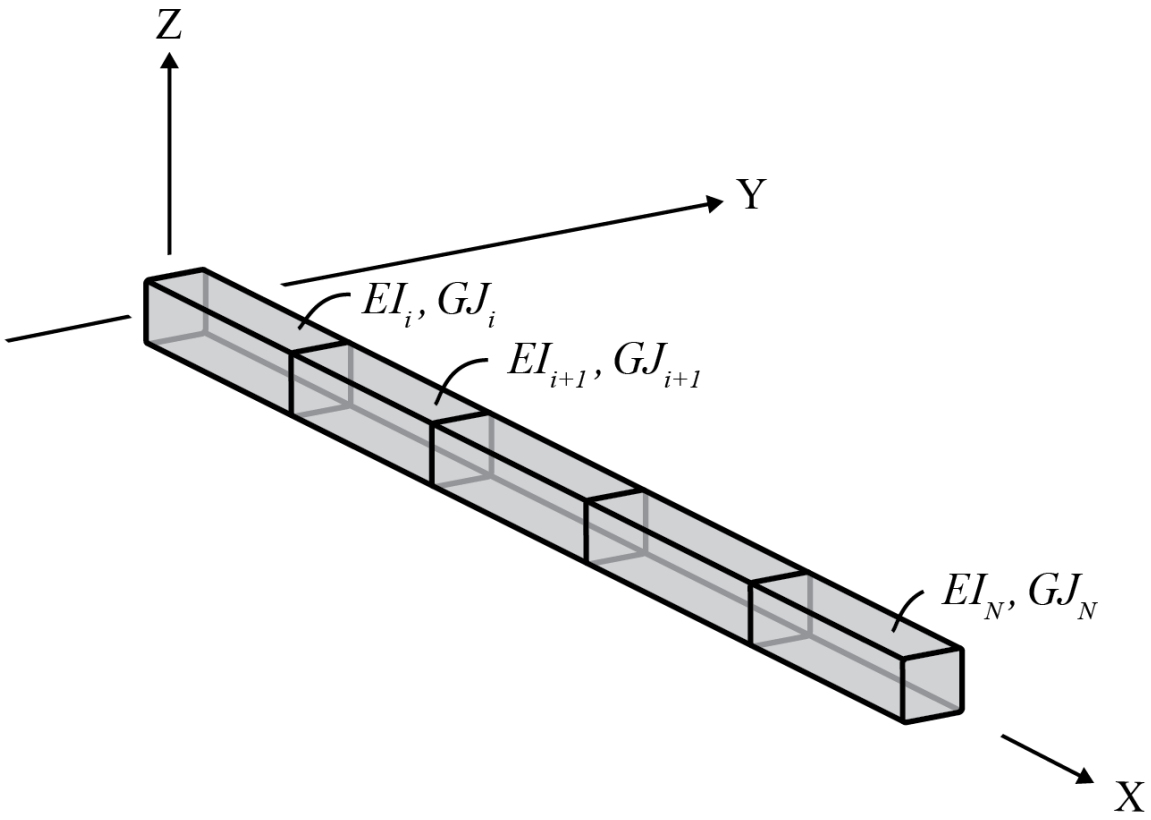

Figure 3.5 Discretized Beam

For such cases, calculating the flexibility influence coefficients begins with Euler-Bernoulli beam bending theory.

$$w''(x,\xi) = \frac{1}{EI(x)} M(x,\xi) \tag{3.61}$$

where $w''(x,\xi)$ is the second derivative of the deflection at point x due to a point load at ξ, $M(x,\xi)$ is the bending moment at point x due to a point load at ξ, and $EI(x)$ is the bending

stiffness of the beam at point x.

The angular rotation of a beam due to an applied torque is given by

$$\theta'(x,\xi) = \frac{1}{GJ(x)} T(x,\xi) \tag{3.62}$$

where $\theta'(x,\xi)$ is the first derivative of the rotation of the beam at point x due to a torque applied at ξ, $T(x,\xi)$ is the torque applied to point ξ, and $GJ(x)$ is the torsional rigidity of the beam at point x.

Two cases must be considered when formulating the moment: $\xi \geq x$ and $x > \xi$. Figure 3.6 shows the internal moment for the case of $\xi \geq x$.

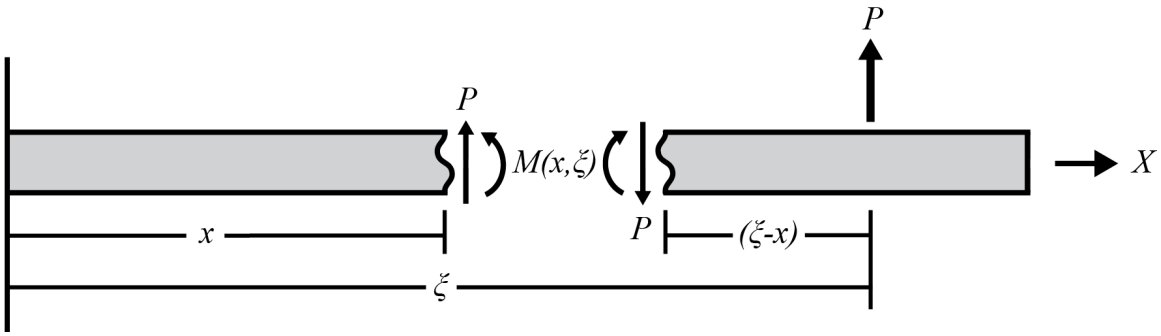

Figure 3.6 Torsion Due to an Applied Moment

For this unit load case, the bending moment is

$$M(x,\xi) = (1)(\xi - x) \tag{3.63}$$

which, when substituted into Eq. (3.61) gives

$$w''(x,\xi) = \frac{1}{EI(x)}(\xi - x) \tag{3.64}$$

For sufficiently small discretized lengths, the bending stiffness is treated as constant along the domain of integration. Integrating once leads to the slope of the beam at point x due to

a point load at ξ. This slope is given by

$$w'(x,\xi) = \frac{1}{EI(x)}\left(\xi x - \tfrac{1}{2}x^2 + c_1\right) \tag{3.65}$$

where c_1 is a constant of integration that is determined by evaluating the slope at the previous segment. Integrating once more yields an equation that describes the displacement of the beam at point x due to a point load at ξ

$$w(x,\xi) = \frac{1}{EI(x)}\left(\tfrac{1}{2}\xi x^2 - \tfrac{1}{6}x^3 + c_1 x + c_2\right) \tag{3.66}$$

where c_2 is a second constant of integration that is determined by evaluating the displacement at the previous segment. Next, an applied torque is considered. Figure 3.7 illustrates the internal torsion at x resulting from an applied torque at ξ for the case of $\xi \geq x$.

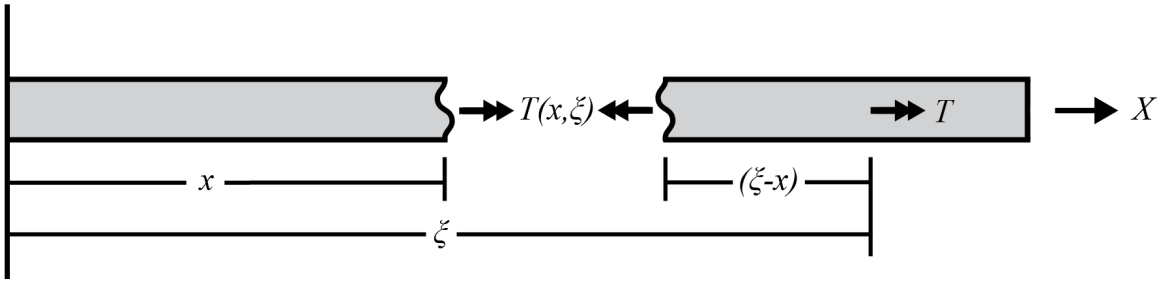

Figure 3.7 Torsion at x Due to an Applied Torque at ξ

For this case, the torsional moment is

$$T(x,\xi) = 1 \tag{3.67}$$

For simplicity, the torsional stiffness is treated as a constant along the domain of integration. Then, for a constant torsional stiffness, Eq. (3.62) becomes

$$\theta'(x,\xi) = \frac{1}{GJ(x)}(1) \tag{3.68}$$

Integrating once gives the rotation of the beam at point x due to a unit torsion at ξ. This is expressed as

$$\theta(x,\xi) = \frac{1}{GJ(x)}\left(x + c_1\right) \tag{3.69}$$

where c_1 is a constant of integration that is determined by evaluating the rotation at the previous segment. For the case of $x > \xi$, the bending moment is

$$M(x,\xi) = 0 \tag{3.70}$$

The resulting slope is

$$w'(x,\xi) = c_1 \tag{3.71}$$

and the displacement is

$$w(x,\xi) = c_1 x + c_2 \tag{3.72}$$

For the case of $x \geq \xi$, the torque is

$$T(x,\xi) = 0 \tag{3.73}$$

The resulting rotation is

$$\theta(x,\xi) = c_1 \tag{3.74}$$

Then, the bending influence coefficients for $\xi \geq x$ become

$$C^{zz}(x,\xi) = w(x,\xi) = \frac{1}{EI(x)}\left(\tfrac{1}{2}\xi x^2 - \tfrac{1}{6}x^3 + c_1 x + c_2\right) \tag{3.75}$$

and the torsional influence coefficients for $\xi \geq x$ are

$$C^{\theta\theta} = \theta(x,\xi) = \frac{1}{GJ(x)}\left(x + c_1\right) \tag{3.76}$$

The bending influence coefficients for $x \geq \xi$ are

$$C^{zz}(x,\xi) = w(x,\xi) = c_1 x + c_2 \tag{3.77}$$

and the torsional influence coefficients for $x \geq \xi$ are

$$C^{\theta\theta}(x,\xi) = \theta(x,\xi) = c_1 \tag{3.78}$$

In the case of a swept wing, the bending and torsion may be coupled together, i.e. $C^{z\theta} = C^{\theta z} \neq 0$. This means an applied force may cause rotation in addition to bending and an applied moment may cause bending in addition to rotation. To simplify the problem, the beam bending and torsion principles are applied in a swept axis system and the resulting bending and torsion are decomposed into a standard Cartesian frame. Figure 3.8 shows a swept wing in a standard aircraft coordinate frame. A swept axis Y_s is aligned with the elastic axis of the wing such that the swept wing can be treated as a straight tapered beam.

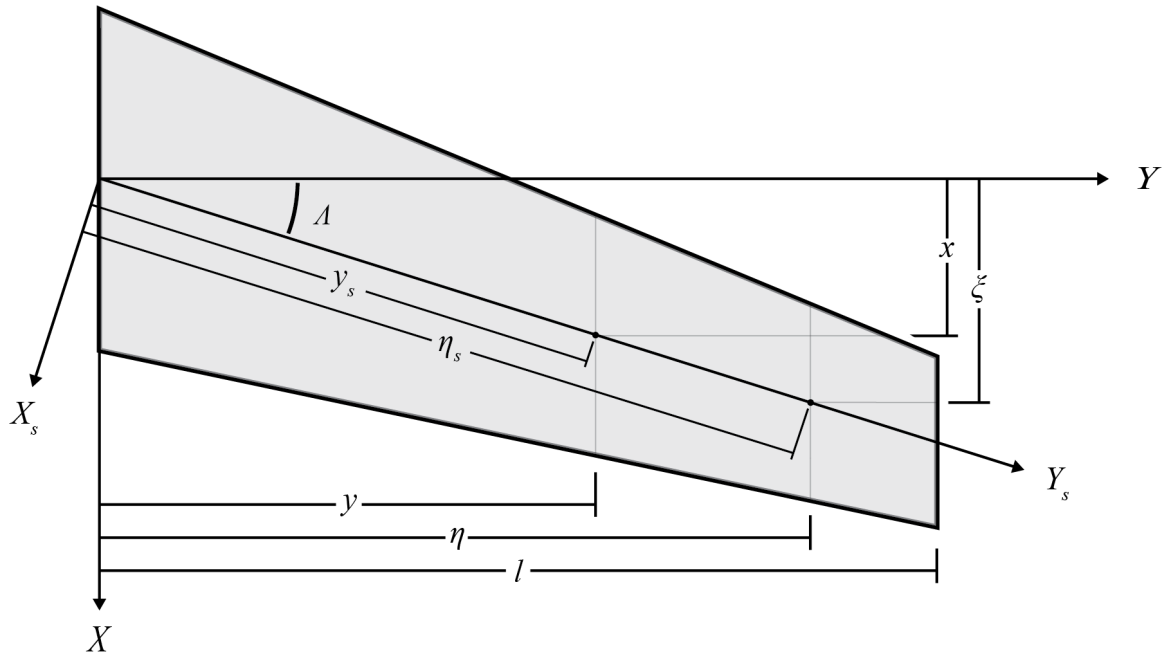

Figure 3.8 Axis System for Swept Wing [1]

Similar to the straight tapered wing, two cases must be considered. In the first case, the applied load is outboard of the measured displacement (e.g. $\xi \geq x$ or $\eta \geq y$). Figure 3.9 shows the internal moments at a section cut due to an applied force in the Z direction when the applied force is outboard of the section cut.

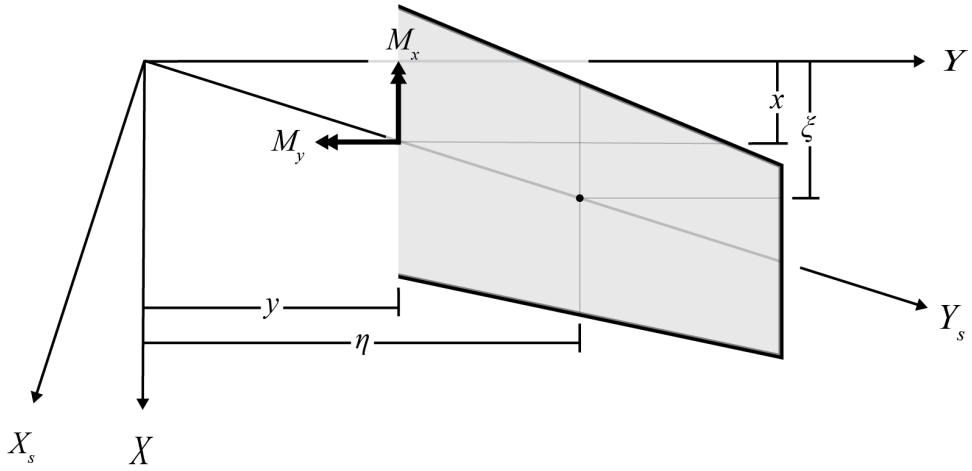

Figure 3.9 Internal Moments Due to Applied Force

For the unit load case, the internal moment about the X axis is

$$M_x = (1)(\eta - y) \tag{3.79}$$

and the internal moment about the Y axis is

$$M_y = (1)(\xi - x) \tag{3.80}$$

Figure 3.10 shows the internal moments at a section cut due to an applied moment in X and Z when the applied moment is outboard of the section cut.

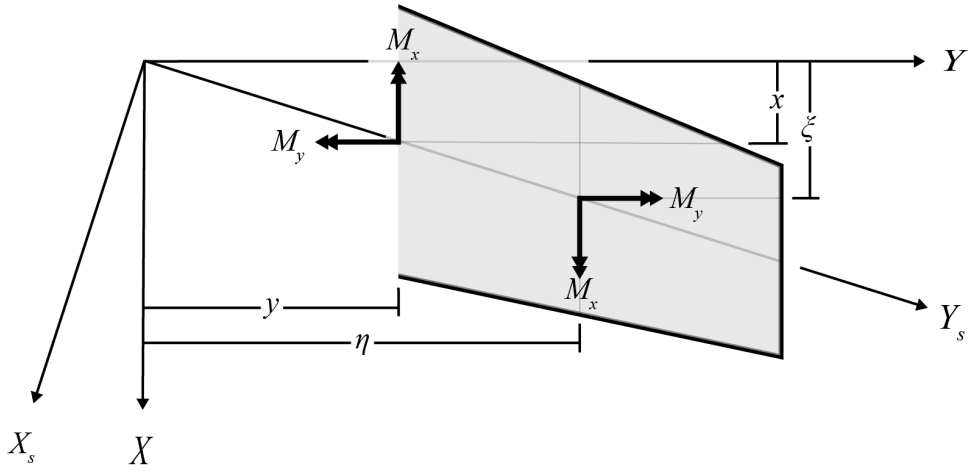

Figure 3.10 Internal Moments Due to an Applied Moment

In the second case, the applied load is inboard of the measured displacement (e.g. $x \geq \xi$ or $y \geq \eta$). For this case, similar to the simplified beam problem,

$$M_x = 0 \tag{3.81}$$

and

$$M_y = 0 \tag{3.82}$$

For each case, the internal moments can then be resolved into the swept coordinate frame and applied to the wing. Figure 3.11 shows the orientation of the swept axis with respect to the global Cartesian frame as well as the moments in each frame.

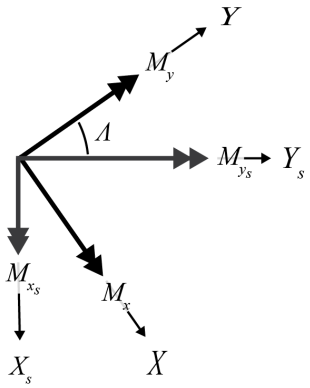

Figure 3.11 Applied Moments in the Swept Axis System

By applying the rotation, the internal moment about the X_s axis is

$$M_{x_s} = M_x cos\Lambda - M_y sin\Lambda \tag{3.83}$$

and the internal moment about the Y_s axis is

$$M_{y_s} = M_x sin\Lambda + M_y cos\Lambda \tag{3.84}$$

where M_{x_s} is analogous to the bending moment for a straight tapered beam and M_{y_s} is analogous to the torsional moment for a straight tapered beam. Then, the displacement $w(x, y, \xi, \eta)$ and slope $\theta(x, y, \xi, \eta)$ due to bending in the swept axis system are calculated using Eq. 3.61 and the twist due to torsion in the swept axis system is calculated using Eq. 3.62. The bending influence coefficients can then be directly calculated as $C^{zz}(x, y, \xi, \eta)$, which is equal to $w(x, y, \xi, \eta)$ for an applied force, and $C^{z\theta}(x, y, \xi, \eta)$, which is equal to $w(x, y, \xi, \eta)$ for an applied moment. Depending on the definition of torsional displacement, the rotational influence coefficients may require rotation back into the unswept coordinate frame. Figure 3.12 shows the relationship between rotations in the unswept and swept coordinate frames.

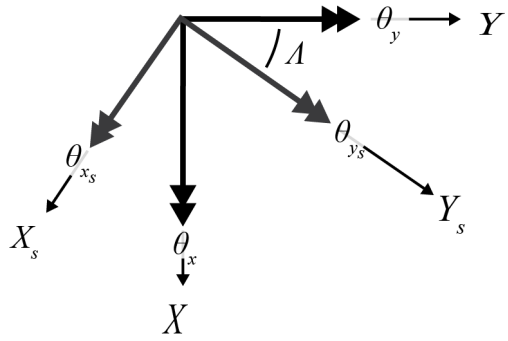

Figure 3.12 Torsional Influence Angles in the Swept Axis System

This yields the relationships

$$\theta_x = \theta_{x_s} cos\Lambda + \theta_{y_s} sin\Lambda \tag{3.85}$$

and

$$\theta_y = -\theta_{x_s} sin\Lambda + \theta_{y_s} cos\Lambda \tag{3.86}$$

Then, the rotational influence coefficients $C^{\theta z}(x, y, \xi, \eta)$ and $C^{\theta\theta}(x, y, \xi, \eta)$ can be determined.

3.4 Matrix Iteration Method

Matrix iteration is a method used to determine the frequencies and mode shapes of a dynamical system that is of the form

$$[M]\underline{\ddot{x}} + [K]\underline{x} = \underline{0} \tag{3.87}$$

Under the assumption of simple harmonic motion where $\underline{x} = \underline{x}_0 e^{i\omega t}$, Eq. (3.87) becomes

$$\left([K] - \omega^2[M]\right)\underline{x}_0 = \underline{0} \tag{3.88}$$

According to Flomenhoft [4], the problem of determining vibrational mode shapes and frequencies of a dynamic system is to reduce Eq. (3.88) to an eigenvalue problem of the form

$$[D]\{A\} = \lambda\{A\} \tag{3.89}$$

where $\{A\}$ is a column matrix of mode shapes and $[D]$ is known as the dynamic matrix, given by

$$[D] = [K]^{-1}[M] \tag{3.90}$$

where $[K]$ is the matrix of stiffness influence coefficients, and $[M]$ is the mass matrix. Substituting Eq. (3.55) into Eq. (3.90) allows for direct computation of the dynamic matrix once the flexibility influence coefficients are known

$$[D] = [C][M] \tag{3.91}$$

The dynamic matrix is useful in the matrix iteration process to determine the first fundamental frequency and mode shape of the dynamic system. When calculating the uncoupled modes, Bisplinghoff et. al. [1] show that the characteristic equation of the system is

$$\frac{1}{\omega_r^2}\phi^{(r)} = [D]\phi^{(r)} \tag{3.92}$$

where ω_r is the frequency of vibration of the rth mode and $\phi^{(r)}$ is its corresponding mode shape. The fundamental mode, $r = 1$, is determined by making an initial estimate of the mode shape $\phi_1^{(1)}$ such that one of the elements $\phi_{1n}^{(1)}$ is equal to 1. The subscript indicates the iteration number. The simplest approach is to take a trial mode shape, $\phi_1^{(1)}$, to be a vector of ones. Substituting the trial mode shape into the right hand side of Eq. (3.92) gives

$$[D]\phi_1^{(1)} = \{N_1\} \tag{3.93}$$

The resulting vector, the left hand side of Eq. (3.93), is then normalized with the nth element

$$\{N_1\} = N_{1n}\left\{\frac{N_1}{N_{1n}}\right\} = N_{1n}\phi_2^{(1)} \tag{3.94}$$

The process is then repeated using $\phi_2^{(1)}$ as the trial mode shape. After m iterations, the resulting vector will converge to the following

$$[D]\phi_m^{(1)} = N_{mn}\phi_m^{(1)} \tag{3.95}$$

where $\phi_m^{(1)}$ is the converged fundamental mode shape and $1/N_{mn}$ is equal to the fundamental frequency ω_1^2. To determine the higher order mode shapes, the orthogonality condition

$$\sum_i B_i^{(r)} A_i^{(r+1)} = 0 \tag{3.96}$$

between mode shapes must be enforced, where $A_i^{(r+1)}$ are unknown values of the relative displacement of the $(r+1)$th mode and $B_i^{(r)}$ is a constant. For the case of no dynamic coupling

$$B_i^{(r)} = m_i \phi_i^{(r)} \tag{3.97}$$

whereas for the case with dynamic coupling

$$B_i^{(r)} = \sum_j m_{ij} \phi_j^{(r)} \tag{3.98}$$

where $\phi^{(r)}$ is a vector of the converged values of the rth mode of a fixed system. The individual elements of the $\left\{A^{(r+1)}\right\}$ vector for the $(r+1)$th mode can be written as

$$\left.\begin{aligned} A_1^{(r+1)} = -\frac{B_2^{(r)}}{B_1^{(r)}} A_2^{(r+1)} - \frac{B_3^{(r)}}{B_1^{(r)}} A_3^{(r+1)} \ldots - \frac{B_n^{(r)}}{B_1^{(r)}} A_n^{(r+1)} \\ A_2^{(r+1)} = A_2^{(r+1)} \\ \vdots \\ A_n^{(r+1)} = A_n^{(r+1)} \end{aligned}\right\} \tag{3.99}$$

Then, for simplicity, the ratio of weighting factors is defined as

$$K_{1i}^{(r)} = -\frac{B_i^{(r)}}{B_1^{(r)}}$$

such that Eq. (3.99) can be written in matrix notation in terms of the coefficients $K_{1i}^{(r)}$.

$$\begin{bmatrix} A_1^{(r+1)} \\ A_2^{(r+1)} \\ \cdot \\ \cdot \\ A_n^{(r+1)} \end{bmatrix} = \begin{bmatrix} 0 & K_{12}^{(r)} & K_{13}^{(r)} & \cdots & K_{1n}^{(r)} \\ 0 & 1 & 0 & \cdots & 0 \\ \cdot & 0 & 1 & \cdots & \cdot \\ \cdot & \cdot & \cdot & \cdots & \cdot \\ 0 & 0 & 0 & \cdots & 1 \end{bmatrix} \begin{bmatrix} A_1^{(r+1)} \\ A_2^{(r+1)} \\ \cdot \\ \cdot \\ A_n^{(r+1)} \end{bmatrix} \tag{3.100}$$

or in more compact form,

$$\left\{A^{(r+1)}\right\} = \left[S^{(r)}\right]\left\{A^{(r+1)}\right\} \tag{3.101}$$

where the square matrix $\left[S^{(r)}\right]$ is known as the "sweeping" matrix. Substituting Eq. (3.101) into Eq. (3.89) yields:

$$\left[D^{(r)}\right]\left[S^{(r)}\right]\left\{A^{(r+1)}\right\} = \lambda\left\{A^{(r+1)}\right\} \tag{3.102}$$

Flomenhoft [4] notes that, since the first column of $\left[S^{(r)}\right]$ is composed of all zeros, the order of the matrix is effectively reduced by one. In the case of determining the second mode, A_1 is multiplied by zero and has no effect on the iteration process. For each subsequent mode that is solved, another column of the sweeping matrix will become all zeros and another row will be comprised of the coefficients K_{ij}, thus the name "sweeping matrix". Essentially, the first mode is removed to determine the second mode. Clough and Penzien [5] explain that iterating a trial mode shape that contains no component of the fundamental mode will converge to the second mode. Expressed mathematically,

$$\left[D^{(1)}\right]\left[S^{(1)}\right]\left\{A^{(2)}\right\} = \left[D^{(2)}\right]\left\{A^{(2)}\right\} \tag{3.103}$$

Therefore, the dynamic matrix for higher modes can be found using the following:

$$\left[D^{(r+1)}\right] = \left[D^{(r)}\right]\left[S^{(r)}\right] \tag{3.104}$$

With this new dynamic matrix, the higher modes are calculated using the iteration process discussed above. However, the computation of higher modes must be approached cautiously. The lower modes must be calculated with great precision as the accuracy of each higher mode reduces by an order of magnitude. Therefore, this sweeping process is generally used to compute no more than the first four or five modes [5]. The uncoupled mode shapes can now be used to compute the system equations of motion.

3.5 Three-Dimensional Equations of Motion

For a three-dimensional wing where multiple bending, torsion, or normal modes are considered, the equations of motion must be modified. This begins with reformulating the kinetic and potential energies of the system to account for a full span wing. This is done by calculating the energy per unit span and integrating along the length of the wing. Figure 3.13 shows the nomenclature used when calculating the energies of the wing. The semi-span length is l, the non-dimensional inboard flap break location is η_i (i.e. $0 \leq \eta_i \leq \eta_o$), and the non-dimensional outboard flap break location is η_o (i.e. $0 \leq \eta_o \leq 1$).

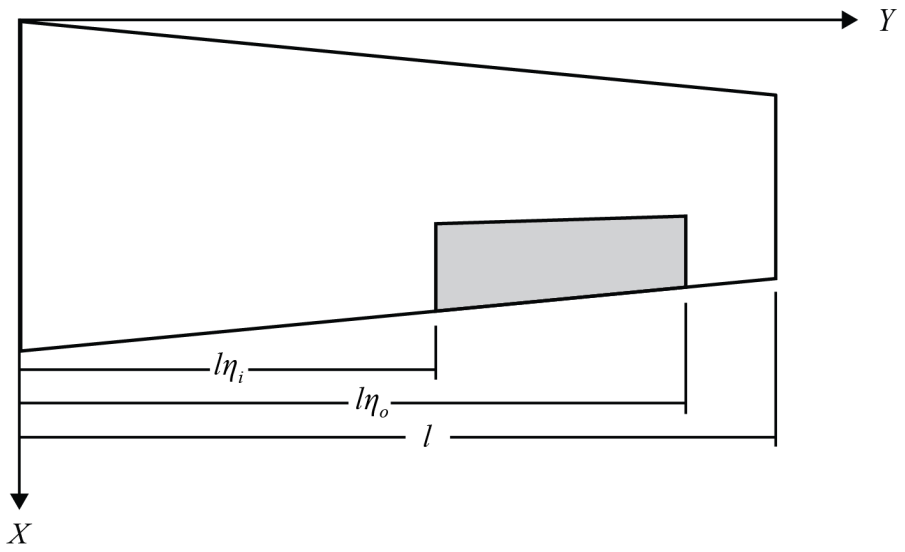

Figure 3.13 Wing and Control Surface Dimensions

The kinetic energy per unit span of a given spanwise location y at time t is:

$$\frac{dT(y,t)}{dy} = \sum_{i=1}^{N_h} \frac{1}{2} m(y) \dot{h}_i^2(y,t) + \sum_{j=1}^{N_\alpha} \frac{1}{2} I_\alpha(y) \dot{\alpha}_j^2(y,t) + \frac{1}{2} I_\beta(y) \dot{\beta}^2(y,t)$$
$$+ \sum_{i=1}^{N_h} \sum_{j=1}^{N_\alpha} S_\alpha(y) \dot{h}_i(y,t) \dot{\alpha}_j(y,t) + \sum_{i=1}^{N_h} S_\beta(y) \dot{h}_i(y,t) \dot{\beta}(y,t) + \sum_{j=1}^{N_\alpha} P_{\alpha\beta}(y) \dot{\alpha}_j(y,t) \dot{\beta}(y,t) \quad (3.105)$$

where $m(y)$ is the wing-flap section mass per unit length, $I_\alpha(y)$ is the wing-flap section mass moment of inertia about the elastic axis per unit length, $I_\beta(y)$ is the flap mass moment of inertia about the hinge line per unit length, $S_\alpha(y)$ is the wing-flap static imbalance about

the elastic axis per unit length, $S_\beta(y)$ is the flap static imbalance about the hingeline per unit length, and $P_{\alpha\beta}$ is the flap rotational imbalance per unit length.

The potential energy per unit span of a given section at location y at time t is a function of the strain energy stored in the system resulting from bending and torsion. This is given by

$$\frac{dV(y,t)}{dy} = \sum_{i=1}^{N_h} \frac{1}{2} EI(y) \left\{ \frac{\partial^2}{\partial y^2} h_i(y,t) \right\}^2 + \sum_{j=1}^{N_\alpha} \frac{1}{2} GJ(y) \left\{ \frac{\partial^2}{\partial y^2} \alpha_j(y,t) \right\}^2 + \frac{1}{2} k_\beta \beta^2(y,t) \quad (3.106)$$

where $EI(y)$ is the bending stiffness at location y, $GJ(y)$ is the torsional stiffness at location y, and k_β is structural stiffness of the flap. Integrating along the span gives the total kinetic energy of the wing at time t:

$$T(t) = \sum_{i=1}^{N_h} \frac{1}{2} M_i \dot{h}_i^2(t) + \sum_{j=1}^{N_\alpha} \frac{1}{2} I_{\alpha_j} \dot{\alpha}_j^2(t) + \frac{1}{2} I_\beta \dot{\beta}^2(t) + \sum_{i=1}^{N_h} \sum_{j=1}^{N_\alpha} S_{\alpha_{ij}} \dot{h}_i(t) \dot{\alpha}_j(t) + \sum_{i=1}^{N_h} S_{\beta_i} \dot{h}_i(t) \dot{\beta}(t) + \sum_{j=1}^{N_\alpha} P_{\alpha\beta_j} \dot{\alpha}_j(t) \dot{\beta}(t) \quad (3.107)$$

where the effective mass of the ith bending mode is

$$M_i = \int_0^l m(y) \phi_{h_i}^2(y) dy \quad (3.108)$$

the effective rotational inertia of the jth torsional mode is

$$I_{\alpha_j} = \int_0^l I_\alpha(y) \phi_{\alpha_j}^2(y) dy \quad (3.109)$$

the effective flap rotational inertia is

$$I_\beta = \int_{l\eta_i}^{l\eta_o} I_\beta(y)(1) dy \quad (3.110)$$

the effective static imbalance between the ith bending and jth torsional modes is

$$S_{\alpha_{ij}} = \int_0^l S_\alpha(y)\phi_{h_i}(y)\phi_{\alpha_j}(y)dy \tag{3.111}$$

the effective flap static imbalance for the ith bending mode is

$$S_{\beta_i} = \int_{l\eta_i}^{l\eta_o} S_\beta(y)\phi_{h_i}(y)(1)dy \tag{3.112}$$

and the effective flap rotational imbalance for the jth torsional mode is

$$P_{\alpha\beta_j} = \int_{l\eta_i}^{l\eta_o} P_{\alpha\beta}(y)\phi_{\alpha_j}(y)(1)dy \tag{3.113}$$

Next, integrating along the span gives the total potential energy of the wing at time t:

$$V(t) = \sum_{i=1}^{N_h} \frac{1}{2} k_{h_i}\, h_i^2(t) + \sum_{i=1}^{N_\alpha} \frac{1}{2} k_{\alpha_j}\, \alpha_j^2(t) + \frac{1}{2} k_\beta \beta^2(t) \tag{3.114}$$

where the effective stiffness of the ith bending mode is

$$k_{h_i} = \int_0^l EI(y) \left\{ \frac{\partial^2}{\partial y^2} \phi_{h_i}(y) \right\}^2 \tag{3.115}$$

the effective stiffness of the jth torsional mode is

$$k_{\alpha_j} = \int_0^l GJ(y) \left\{ \frac{\partial^2}{\partial y^2} \phi_{\alpha_j}(y) \right\}^2 \tag{3.116}$$

and the effective flap stiffness is

$$k_\beta = \int_{l\eta_i}^{l\eta_o} k_\beta(y)dy \tag{3.117}$$

Alternatively, if the natural frequencies are known, the effective stiffness for each mode can be calculated by applying a simple harmonic motion assumption to the unforced vibration case, assuming it is only free to move with a single degree-of-freedom (DOF); i.e., all other modes

are fixed. For example, the equation of motion for the first bending mode (h_1) becomes

$$\frac{d}{dt}\left(\frac{\partial T}{\partial \dot{h}_1}\right) + \frac{\partial V}{\partial h_1} = 0 = M_1\ddot{h} + k_{h_1}h \tag{3.118}$$

Applying the simple harmonic motion condition to Eq. (3.118) yields

$$\left(-M_1\omega_{h_1}^2 + k_{h_1}\right)h = 0 \tag{3.119}$$

which simplifies to

$$k_{h_1} = M_1\omega_{h_1}^2 \tag{3.120}$$

It follows that the effective stiffness for the ith bending mode is

$$k_{h_i} = M_i\omega_{h_i}^2 \tag{3.121}$$

the stiffness for the jth torsional mode is

$$k_{\alpha_j} = I_{\alpha_j}\omega_{\alpha_j}^2 \tag{3.122}$$

and the stiffness of the flap is

$$k_{\beta} = I_{\beta}\omega_{\beta}^2 \tag{3.123}$$

Finally, given Eq. (3.107) and Eq. (3.114) the equations of motion that govern the elastic wing are calculated using Eq. (3.3). The resulting equations for all bending DOFs are

$$M_1\ddot{h}_1 + S_{\alpha_{11}}\ddot{\alpha}_1 + \cdots + S_{\alpha_{1N_\alpha}}\ddot{\alpha}_{N_\alpha} + S_{\beta_1}\ddot{\beta} + k_{h_1}h_1 = Q_{h_1} \tag{3.124}$$

$$M_2\ddot{h}_2 + S_{\alpha_{21}}\ddot{\alpha}_1 + \cdots + S_{\alpha_{2N_\alpha}}\ddot{\alpha}_{N_\alpha} + S_{\beta_2}\ddot{\beta} + k_{h_2}h_2 = Q_{h_2} \tag{3.125}$$

$$\vdots$$

$$M_{N_h}\ddot{h}_{N_h} + S_{\alpha_{N_h1}}\ddot{\alpha}_1 + \cdots + S_{\alpha_{N_hN_\alpha}}\ddot{\alpha}_{N_\alpha} + S_{\beta_{N_h}}\ddot{\beta} + k_{h_{N_h}}h_{N_h} = Q_{h_{N_h}} \tag{3.126}$$

The resulting equations for all torsional DOFs are

$$S_{\alpha_{11}}\ddot{h}_1 + \cdots + S_{\alpha_{N_h 1}}\ddot{h}_{N_h} + I_{\alpha_1}\ddot{\alpha}_1 + P_{\alpha\beta_1}\ddot{\beta} + I_{\alpha_1}\omega_{\alpha_1}^2\,\alpha_1 = Q_{\alpha_1} \quad (3.127)$$

$$S_{\alpha_{12}}\ddot{h}_1 + \cdots + S_{\alpha_{N_h 2}}\ddot{h}_{N_h} + I_{\alpha_2}\ddot{\alpha}_2 + P_{\alpha\beta_2}\ddot{\beta} + I_{\alpha_2}\omega_{\alpha_2}^2\,\alpha_2 = Q_{\alpha_2} \quad (3.128)$$

$$\vdots$$

$$S_{\alpha_{1N_\alpha}}\ddot{h}_1 + \cdots + S_{\alpha_{N_h N_\alpha}}\ddot{h}_{N_h} + I_{\alpha_{N_\alpha}}\ddot{\alpha}_{N_\alpha} + P_{\alpha\beta_{N_\alpha}}\ddot{\beta} + I_{\alpha_{N_\alpha}}\omega_{\alpha_{N_\alpha}}^2\,\alpha_{N_\alpha} = Q_{\alpha_{N_\alpha}} \quad (3.129)$$

and the equation for the flap DOF is

$$S_{\beta_1}\ddot{h}_1 + \cdots + S_{\beta_{N_h}}\ddot{h}_{N_h} + P_{\alpha\beta_1}\ddot{\alpha}_1 + \cdots + P_{\alpha\beta_{N_\alpha}}\ddot{\alpha}_{N_\alpha} + I_\beta\ddot{\beta} + I_\beta\omega_\beta^2\,\beta = Q_\beta \quad (3.130)$$

Together, these form a system of $(N_h + N_\alpha + 1)$ equations of motion. These can be written more compactly in matrix form as

$$[M_s]\,\underline{\ddot{x}} + [K_s]\,\underline{x} = \underline{Q} \quad (3.131)$$

where the state vector is

$$\underline{x} = \left\{ h_1 \quad \cdots \quad h_{N_h} \quad \alpha_1 \quad \cdots \quad \alpha_{N_\alpha} \quad \beta \right\}^\top \quad (3.132)$$

Next, the structural mass matrix can be written as

$$[M_s] = \begin{bmatrix} M_1 & \cdots & 0 & S_{\alpha_{11}} & \cdots & S_{\alpha_{1N_\alpha}} & S_{\beta_1} \\ \vdots & \ddots & \vdots & \vdots & \ddots & \vdots & \vdots \\ 0 & \cdots & M_{N_h} & S_{\alpha_{N_h 1}} & \cdots & S_{\alpha_{N_h N_\alpha}} & S_{\beta_{N_h}} \\ S_{\alpha_{11}} & \cdots & S_{\alpha_{N_h 1}} & I_{\alpha_1} & \cdots & 0 & P_{\alpha_{\beta_1}} \\ \vdots & \ddots & \vdots & \vdots & \ddots & \vdots & \vdots \\ S_{\alpha_{1N_\alpha}} & \cdots & S_{\alpha_{N_h N_\alpha}} & 0 & \cdots & I_{\alpha_{N_\alpha}} & P_{\alpha\beta_{N_\alpha}} \\ S_{\beta_1} & \cdots & S_{\beta_{N_h}} & P_{\alpha\beta_1} & \cdots & P_{\alpha\beta_{N_\alpha}} & I_\beta \end{bmatrix} \tag{3.133}$$

This is condensed into a series of sub-matrices as follows

$$[M_s] = \begin{bmatrix} [M] & [S_\alpha] & [S_\beta] \\ [S_\alpha]^\top & [I_\alpha] & [P_{\alpha\beta}] \\ [S_\beta]^\top & [P_{\alpha\beta}]^\top & [I_\beta] \end{bmatrix} \tag{3.134}$$

where the matrix of effective masses is

$$[M] = \begin{bmatrix} M_1 & \cdots & 0 \\ \vdots & \ddots & \vdots \\ 0 & \cdots & M_{N_h} \end{bmatrix} \tag{3.135}$$

the matrix of effective static imbalances is

$$[S_\alpha] = \begin{bmatrix} S_{\alpha_{11}} & \cdots & S_{\alpha_{1N_\alpha}} \\ \vdots & \ddots & \vdots \\ S_{\alpha_{N_h 1}} & \cdots & S_{\alpha_{N_h N_\alpha}} \end{bmatrix} \tag{3.136}$$

the matrix of effective flap imbalances is

$$[S_\beta] = \begin{bmatrix} S_{\beta_1} \\ \vdots \\ S_{\beta_{N_h}} \end{bmatrix} \tag{3.137}$$

the matrix of effective mass moments of inertia is

$$[I_\alpha] = \begin{bmatrix} I_{\alpha_1} & \cdots & 0 \\ \vdots & \ddots & \vdots \\ 0 & \cdots & I_{\alpha_{N_\alpha}} \end{bmatrix} \tag{3.138}$$

the matrix of effective rotational imbalances is

$$[P_{\alpha\beta}] = \begin{bmatrix} P_{\alpha\beta_1} \\ \vdots \\ P_{\alpha\beta_{N_\alpha}} \end{bmatrix} \tag{3.139}$$

and the flap moment of inertia about the hingeline is

$$[I_\beta] = I_\beta \tag{3.140}$$

Similarly, the structural stiffness matrix is

$$[K_s] = \begin{bmatrix} k_{h_1} & \cdots & 0 & 0 & \cdots & 0 & 0 \\ \vdots & \ddots & \vdots & \vdots & \ddots & \vdots & \vdots \\ 0 & \cdots & k_{h_{N_h}} & 0 & \cdots & 0 & 0 \\ 0 & \cdots & 0 & k_{\alpha_1} & \cdots & 0 & 0 \\ \vdots & \ddots & \vdots & \vdots & \ddots & \vdots & \vdots \\ 0 & \cdots & 0 & 0 & \cdots & k_{\alpha_{N_\alpha}} & 0 \\ 0 & \cdots & 0 & 0 & \cdots & 0 & k_\beta \end{bmatrix} \tag{3.141}$$

which is condensed into a series of sub-matrices

$$[K_s] = \begin{bmatrix} [K_h] & [0]_{N_h \times N_\alpha} & [0]_{N_h \times 1} \\ [0]_{N_\alpha \times N_h} & [K_\alpha] & [0]_{N_\alpha \times 1} \\ [0]_{1 \times N_h} & [0]_{1 \times N_\alpha} & [K_\beta] \end{bmatrix} \tag{3.142}$$

where the matrix of effective bending stiffness is

$$[K_h] = \begin{bmatrix} k_{h_1} & \cdots & 0 \\ \vdots & \ddots & \vdots \\ 0 & \cdots & k_{h_{N_h}} \end{bmatrix} \tag{3.143}$$

the matrix of effective torsional stiffness is

$$[K_\alpha] = \begin{bmatrix} k_{\alpha_1} & \cdots & 0 \\ \vdots & \ddots & \vdots \\ 0 & \cdots & k_{\alpha_{N_\alpha}} \end{bmatrix} \tag{3.144}$$

and the effective flap stiffness is

$$[K_\beta] = k_\beta \tag{3.145}$$

Finally, the vector of generalized forces is

$$\underline{Q} = \begin{bmatrix} Q_{h_1} \\ \vdots \\ Q_{h_{N_h}} \\ Q_{\alpha_1} \\ \vdots \\ Q_{\alpha_{N_\alpha}} \\ Q_\beta \end{bmatrix} \tag{3.146}$$

For a given DOF, the generalized force is a combination of damping and aerodynamic forces or moments. It has been shown that the structural damping is a function of the amplitude of the system and its frequency. Furthermore, the damping force can be described by a force whose magnitude is proportional to the elastic restoring force, but in phase with the velocity [3]. For each bending DOF, the structural damping due to bending rate and lift is considered:

$$Q_{h_i} = -c_{h_i}\dot{h}_i - L_{e_i} \tag{3.147}$$

where c_{h_i} is the effective damping of the ith bending mode and L_{e_i} is the elastic lift of the ith bending mode. For each torsional DOF, the structural damping due to torsion rate and the bending moment about the elastic axis is considered:

$$Q_{\alpha_j} = -c_{\alpha_j}\dot{\alpha}_j + M_{e_j} \tag{3.148}$$

where c_{α_j} is the effective damping of the jth torsional mode and M_{e_j} is the torsional moment about the elastic axis of the jth torsional mode. For the flap, the structural damping due to the flap rate and the hinge moment is considered:

$$Q_\beta = -c_\beta\dot{\beta} + T_e \tag{3.149}$$

Substituting the vector of the generalized forces into Eq. (3.131) gives the final set of differential equations that govern the structural dynamics:

$$[M_s]\,\underline{\ddot{x}} + [C_s]\,\underline{\dot{x}} + [K_s]\,\underline{x} = \underline{Q} \tag{3.150}$$

where the structural damping matrix is

$$[C_s] = \begin{bmatrix} c_{h_1} & \cdots & 0 & 0 & \cdots & 0 & 0 \\ \vdots & \ddots & \vdots & \vdots & \ddots & \vdots & \vdots \\ 0 & \cdots & c_{h_{N_h}} & 0 & \cdots & 0 & 0 \\ 0 & \cdots & 0 & c_{\alpha_1} & \cdots & 0 & 0 \\ \vdots & \ddots & \vdots & \vdots & \ddots & \vdots & \vdots \\ 0 & \cdots & 0 & 0 & \cdots & c_{\alpha_{N_\alpha}} & 0 \\ 0 & \cdots & 0 & 0 & \cdots & 0 & c_\beta \end{bmatrix} \tag{3.151}$$

This is condensed into a series of sub-matrices

$$[C_s] = \begin{bmatrix} [C_h] & [0]_{N_h \times N_\alpha} & [0]_{N_h \times 1} \\ [0]_{C_\alpha \times N_h} & [C_\alpha] & [0]_{N_\alpha \times 1} \\ [0]_{1 \times N_h} & [0]_{1 \times N_\alpha} & [C_\beta] \end{bmatrix} \tag{3.152}$$

where the matrix of effective bending structural damping is

$$[C_h] = \begin{bmatrix} c_{h_1} & \cdots & 0 \\ \vdots & \ddots & \vdots \\ 0 & \cdots & c_{h_{N_h}} \end{bmatrix} \tag{3.153}$$

the matrix of effective torsional structural damping is

$$[C_\alpha] = \begin{bmatrix} c_{\alpha_1} & \cdots & 0 \\ \vdots & \ddots & \vdots \\ 0 & \cdots & c_{\alpha_{N_h}} \end{bmatrix} \tag{3.154}$$

and the matrix of effective flap damping is

$$[C_\beta] = c_\beta \tag{3.155}$$

As previously stated, the damping force is proportional to the elastic restoring force and some damping coefficient g. Thus, the damping coefficients for each bending mode in Eq. (3.151) are calculated by

$$c_{h_i} = g\, M_i \omega_{h_i} \tag{3.156}$$

the damping coefficients for each torsional mode are calculated by

$$c_{\alpha_j} = g\, I_i \omega_{\alpha_j} \tag{3.157}$$

and the damping coefficient for the flap mode is calculated by

$$c_\beta = g\, I_\beta \omega_\beta \tag{3.158}$$

Next, the aerodynamic forces and moments are calculated. The total lift, torsional moment, and hinge moment are written in terms of the contribution from each mode. The lift at station y exciting the ith bending mode is

$$L_{e_i}(y) = L_{\dot{h}_i}(y) + \sum_{j=1}^{N_\alpha} L_{\alpha_j}(y) + \sum_{j=1}^{N_\alpha} L_{\dot{\alpha}_j}(y) + L_\beta(y) + L_{\dot{\beta}}(y) + L_\delta(y) \tag{3.159}$$

where $L_{\dot{h}_i}(y)$ is the lift due to the rate of the ith bending mode, $L_{\alpha_j}(y)$ is the lift due to the

jth torsion mode, $L_{\dot{\alpha}_j}(y)$ is the lift due to the rate of the jth torsional mode, $L_\beta(y)$ is the lift due to elastic flap deflection, $L_{\dot{\beta}}(y)$ is the lift due to the rate of elastic flap deflection, and $L_\delta(y)$ is the lift due to control surface deflection. The torsional moment about the elastic axis at station y exciting the jth torsional mode is

$$M_{e_j}(y) = \sum_{i=1}^{N_h} M_{\dot{h}_i}(y) + M_{\alpha_j}(y) + M_{\dot{\alpha}_j}(y) + M_\beta(y) + M_{\dot{\beta}}(y) + M_\delta(y) \tag{3.160}$$

where $M_{\dot{h}_i}(y)$ is the torsional moment due to the rate of the ith bending mode, $M_{\alpha_j}(y)$ is the torsional moment due to the jth torsional mode, $M_{\dot{\alpha}_j}(y)$ is the torsional moment due to the rate of the jth bending mode, $M_\beta(y)$ is the torsional moment due to elastic flap deflection, $M_{\dot{\beta}}(y)$ is the torsional moment due to the rate of elastic flap deflection, and $M_\delta(y)$ is the torsional moment due to control surface deflection. The hinge moment at station y is

$$T_e(y) = \sum_{i=1}^{N_h} T_{\dot{h}_i}(y) + \sum_{j=1}^{N_\alpha} T_{\alpha_j}(y) + \sum_{j=1}^{N_\alpha} T_{\dot{\alpha}_j}(y) + T_\beta(y) + T_{\dot{\beta}}(y) + T_\delta(y) \tag{3.161}$$

where $T_{\dot{h}_i}(y)$ is the hinge moment due to the rate of the ith bending mode, $T_{\alpha_j}(y)$ is the hinge moment due to the jth torsional mode, $T_{\dot{\alpha}_j}(y)$ is the hinge moment due to the rate of the jth torsional mode, $T_\beta(y)$ is the hinge moment due to elastic flap deflection, $T_{\dot{\beta}}(y)$ is the hinge moment due to the rate of elastic flap deflection, and $T_\delta(y)$ is the hinge moment due to control surface deflection.

The net aerodynamic influence for each mode is found by applying modal weighting and integrating along the span. For a wing semi-span, the effective lift that excites the ith bending mode is

$$L_{e_i} = \int_0^l L_e(y)\phi_{h_i}(y)dy \tag{3.162}$$

Substituting Eq. (3.159) into Eq. (3.162) gives the effective lift for the ith bending mode in terms of aerodynamic influence. Due to the orthogonality of modes, the only bending contribution to the lift into the ith bending mode is that of $\dot{h}_i$. Thus, the total effective lift

for the ith bending mode is

$$L_{e_i} = A_{h_i\dot{h}_i} + \sum_{j=1}^{N_\alpha} A_{h_i\alpha_j} + \sum_{j=1}^{N_\alpha} A_{h_i\dot{\alpha}_j} + A_{h_i\beta} + A_{h_i\dot{\beta}} + A_{h_i\delta} \tag{3.163}$$

where each quantity A is the aerodynamic influence of one mode onto another. For example, the aerodynamic influence of the ith bending mode onto the ith bending mode is given by

$$A_{h_i\dot{h}_i} = \int_0^l L_{\dot{h}_i}(y)\phi_{h_i}(y)dy \tag{3.164}$$

or

$$A_{\dot{h}_i} = \sum_{k=1}^{n} L_{\dot{h}_i}(y_k)\phi_{h_i}(y_k) \tag{3.165}$$

where n is the total number of spanwise stations. Similarly, the effective torsional moment for the jth torsional mode is

$$M_{e_j} = \int_0^l M_e(y)\phi_{\alpha_j}(y)dy \tag{3.166}$$

and the effective hinge moment is

$$T_e = \int_{l\eta_i}^{l\eta_o} T_e(y)(1)dy \tag{3.167}$$

Both the torsional moment and hinge moment can also be expanded in terms of the aerodynamic influence of each mode. With all of the generalized forces known, they can be

assembled into the aerodynamic forcing vector as follows

$$\underline{F}_a = \begin{bmatrix} L_{e_i} \\ \vdots \\ L_{e_{N_h}} \\ M_{e_j} \\ \vdots \\ M_{e_{N_\alpha}} \\ T_e \end{bmatrix} \tag{3.168}$$

Substituting into Eq. (3.150) yields the the full set of aeroelastic equations for a three dimensional wing, fixed at its root.

$$[M_s]\,\ddot{\underline{x}} + [C_s]\,\dot{\underline{x}} + [K_s]\,\underline{x} = \underline{F}_a \tag{3.169}$$

3.6 Rigid-Body Dynamics

The rigid-body aircraft equations of motion are developed such that the elastic wing dynamics can be appended to the model. Figure 3.15 shows the standard aircraft body axis frame in which the combined rigid-elastic equations of motion are developed.

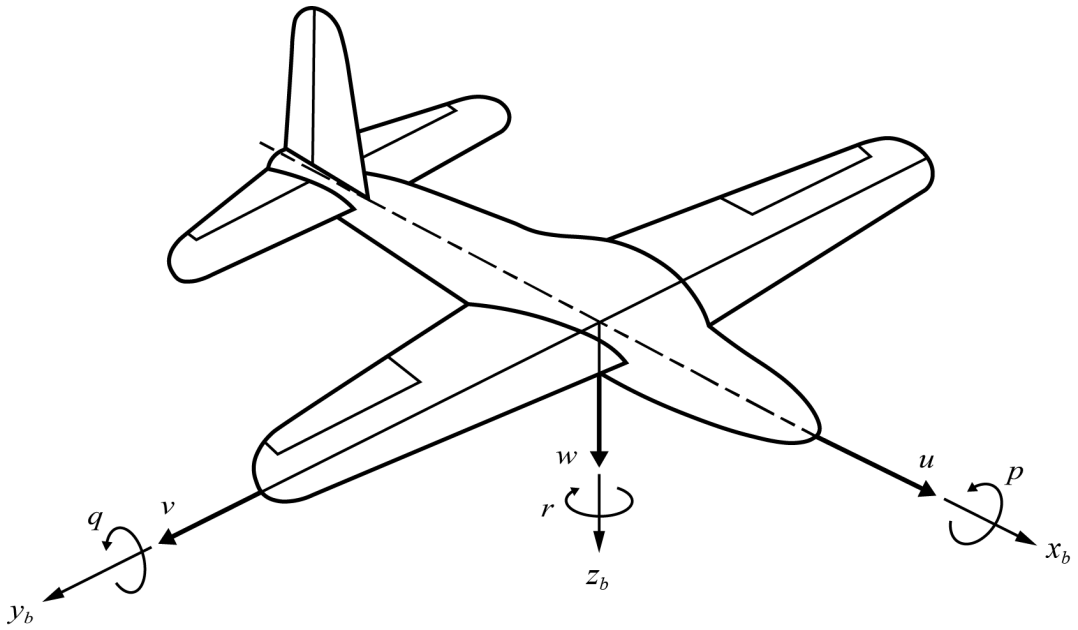

Figure 3.14 Aircraft Body Axis System Notations

For simplicity, the rigid body and flexible dynamics are assumed to not be inertially coupled; they are only coupled through the aerodynamic forcing. The complete set of equations that governs six degree-of-freedom aircraft dynamics is

$$m(\dot{u} + qw - rv) = -mg\,sin\theta + F_x \tag{3.170}$$

$$m(\dot{v} + ur - pw) = mg\,cos\theta\,sin\phi + F_y \tag{3.171}$$

$$m(\dot{w} + pv - qu) = mg\,cos\theta\,cos\phi + F_z \tag{3.172}$$

$$\dot{p}I_{xx} - \dot{r}I_{xz} - pqI_{xz} + rq(I_{zz} - I_{zz}) = M_x \tag{3.173}$$

$$\dot{q}I_{yy} + pq(I_{xx} - I_{zz}) + (p^2 - r^2)I_{xz} = M_y \tag{3.174}$$

$$\dot{r}I_{zz} - \dot{p}I_{xz} + pq(I_{yy} - I_{xx}) + qrI_{xz} = M_z \tag{3.175}$$

In the interest of simplicity, the analysis is reduced to longitudinal motion only. Thus, the rigid-body equations of motion become

$$\dot{u} = -qw - gsin\theta + \frac{X}{m} \tag{3.176}$$

$$\dot{w} = qu + gcos\theta + \frac{Z}{m} \tag{3.177}$$

$$\dot{q} = \frac{M}{I_{yy}} \tag{3.178}$$

$$\dot{\theta} = q \tag{3.179}$$

$$\dot{h} = usin\theta - wcos\theta \tag{3.180}$$

where u is velocity in the x-body direction, w is the velocity in the z-body direction, q is the pitch rate, θ is the pitch angle of the aircraft, and h is the altitude. Furthermore, X, Z, and M are the aircraft body axis forces and moments resulting from rigid body aerodynamics (i.e. angle of attack, engine thrust, drag, etc.), flexible aerodynamics, and thrust. The equations of motion are linearized about the trim condition which gives

$$\Delta\dot{u} = -w^*\Delta q - gsin\theta^*\Delta\theta + \frac{\Delta X}{m} \tag{3.181}$$

$$\Delta\dot{w} = u^*\Delta q + gcos\theta^*\Delta\theta + \frac{\Delta Z}{m} \tag{3.182}$$

$$\Delta\dot{q} = \frac{\Delta M}{I_{yy}} \tag{3.183}$$

$$\Delta\dot{\theta} = \Delta q \tag{3.184}$$

$$\Delta\dot{h} = sin\theta^*\Delta u - cos\theta^*\Delta w + V_T^*\Delta\theta \tag{3.185}$$

where terms with an asterisk, such as θ^*, represent the trim value and terms with Δ represent perturbations from trim conditions. The forcing terms such as ΔX are calculated using the unsteady vortex-lattice method and resolved into the body frame for analysis. Using the unsteady vortex-lattice solution, the aerodynamic forces and moments are calculated in the

wind axis system. The forces and moments must be transformed into the body axis system. Figure 3.15 illustrates the relationship between the aircraft body, wind, and stability axes.

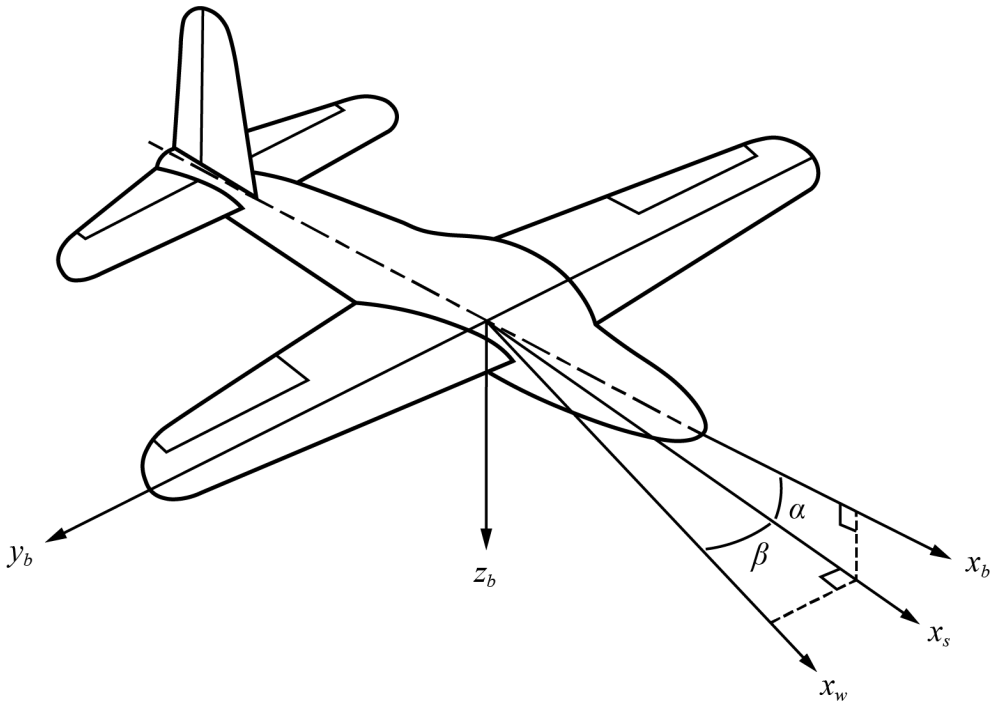

Figure 3.15 Aircraft Stability and Wind Axis Systems

When considering the aircraft equations of motion, the net force on the vehicle can be decomposed into rigid and elastic increments. For example, the force in the x direction is

$$F_x = F_{x_r} + F_{x_e} + F_{x_c} \tag{3.186}$$

where F_{x_r} are the rigid increments of the force in the x_b direction, including the force due to angle of attack, sideslip, roll rate, pitch rate, and yaw rate. F_{x_e} is the elastic increment of the force in the x_b direction, including the force due to wing torsion, bending rate, and torsion rate. Finally, F_{x_c} are the forces in the x_b direction due to control inputs. The same process is applied to the remaining aerodynamic forces and moments acting on the system. Another important aspect in calculating the total vehicle airloads is the position of the wing with respect to the aircraft's center of gravity, as shown in Figure 3.16.

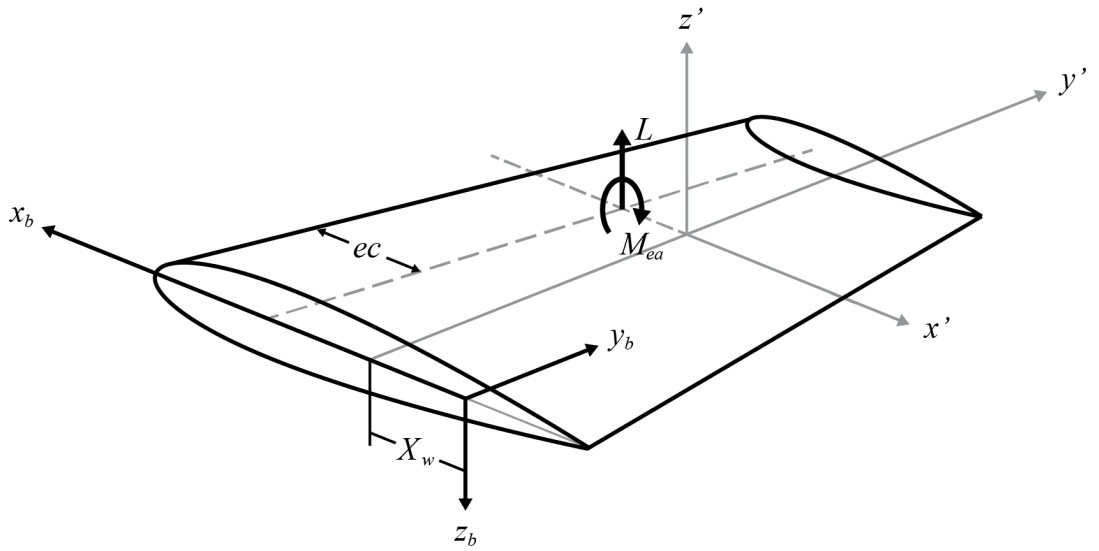

Figure 3.16 Wing in Aircraft Body Frame

When considering the elastic equations of motion, the forces must also be decomposed into rigid, elastic, and control increments:

$$L = L_r + L_e + L_c \tag{3.187}$$

For longitudinal only motion, the total rigid lift is

$$L_r = L_0 + L_{\alpha_v} + L_q \tag{3.188}$$

where L_0 is the zero angle of attack lift due to wing incidence or camber, L_{α_v} is lift due to vehicle angle of attack, and L_q is the lift due to pitch rate. The total elastic lift is

$$L_e = \sum_{i=1}^{N_h} L_{\dot{h}_i} + \sum_{j=1}^{N_\alpha} (L_{\alpha_i} + L_{\dot{\alpha}_i}) + L_\beta + L_{\dot{\beta}} \tag{3.189}$$

where L_{h_i} is the lift due to the ith bending mode, L_{α_j} is the lift due to deformation of the jth bending mode, $L_{\dot{\alpha}_j}$ is the lift due to rate of deformation of the jth torsional mode, L_β is lift due to elastic flap deformation, and $L_{\dot{\beta}}$ is the lift due to the rate of elastic flap deformation.

Similarly, the rigid drag is

$$D_r = D_0 + D_{\alpha_v} + D_q \tag{3.190}$$

and the elastic drag is

$$D_e = \sum_{i=1}^{N_h} D_{\dot{h}_i} + \sum_{j=1}^{N_\alpha} (D_{\alpha_i} + D_{\dot{\alpha}_i}) + D_\beta + D_{\dot{\beta}} \tag{3.191}$$

Finally, the rigid torsional moment about the elastic axis is

$$M_r = M_0 + M_{\alpha_v} + M_q \tag{3.192}$$

and the elastic torsional moment about the elastic axis is

$$M_e = \sum_{i=1}^{N_h} M_{\dot{h}_i} + \sum_{j=1}^{N_\alpha} (M_{\alpha_i} + M_{\dot{\alpha}_i}) + M_\beta + M_{\dot{\beta}} \tag{3.193}$$

At this point, an important distinction must be made between M and M_{CG}. M is the moment about the elastic axis that will result in wing torsion, and M_{CG} is the moment about the CG of the aircraft that will result in aircraft pitching. Special care should be taken as to not use one in place of the other. Once the total lift and torsional moment about the elastic axis are calculated for a given timestep, they can be converted to modal coordinates and used to calculated the generalized displacements using Eq. (3.169).

Some additional steps must be taken to use the lift, drag, and torsional moment in the rigid-body aircraft equations of motion. First, the loads must be transformed from the wind axis system into the aircraft body axis system. For longitudinal only motion, the wind axis and stability axis are aligned. Then, the relationship between a force in the stability axes and a force in the body axes is

$$F_{x_b} = F_{x_s} cos\alpha - F_{z_s} sin\alpha \tag{3.194}$$

and

$$F_{z_b} = F_{z_s} cos\alpha + F_{x_s} sin\alpha \tag{3.195}$$

where

$$F_{z_s} = -L \tag{3.196}$$

and

$$F_{x_s} = -D \tag{3.197}$$

The net moment about the the CG is

$$M_{CG} = M + L(X_w + (0.5 - e)c_r) \tag{3.198}$$

where X_w is the distance from the aircraft CG to the mid chord of the wing root, c_r is the root chord length, and e is the nondimensional location of the elastic axis, measured from the leading edge. The implementation of the perturbation lift and moment for use in Eqs. (3.181) through (3.185) is discussed in the following chapter.

3.7 Combined Rigid-Elastic Dynamics

Combining the elastic wing dynamics with the rigid-body aircraft dynamics gives the complete dynamic model used in this analysis. For simulation use, the system is represented by

$$\left\{ \begin{array}{c} \dot{\underline{x}}_r \\ \hdashline \dot{\underline{x}}_e \end{array} \right\} = \left[\begin{array}{c:c} A_{rr} & A_{re} \\ \hdashline A_{er} & A_{ee} \end{array} \right] \left\{ \begin{array}{c} \underline{x}_r \\ \hdashline \underline{x}_e \end{array} \right\} + \left[\begin{array}{c:c} B_{rr} & B_{re} \\ \hdashline B_{er} & B_{ee} \end{array} \right] \left\{ \begin{array}{c} \underline{u}_r \\ \hdashline \underline{u}_e \end{array} \right\} \tag{3.199}$$

where A_{rr} is a matrix of rigid-body elements that affect rigid body motion, A_{re} is a matrix of elastic elements that affect rigid body motion, A_{er} is a matrix of rigid body elements that affect flexible motion, and A_{ee} is a matrix of elastic elements that affect flexible motion. Further, B_{rr} is a matrix of rigid-body inputs that affect rigid-body motion, i.e. the pitching moment due to elevator deflection, B_{re} is a matrix of elastic inputs that affect rigid-body motion, i.e. the change in lift due to wing torsion, B_{er} is a matrix of rigid-body inputs that

affect elastic motion, i.e. the change in wing bending due to elevator deflection, and B_{ee} is a matrix of elastic inputs that affect elastic motion, i.e. the wing torsion due to aileron deflection.

Based on the formulation of the structural dynamics equations of motion discussed in Section 3.5 the elastic state vector is

$$\underline{x}_e = \left\{ h_1 \quad \cdots \quad h_{N_h} \quad \alpha_1 \quad \cdots \quad \alpha_{N_\alpha} \quad \beta \right\}^\top \tag{3.200}$$

and the rigid-body state vector is

$$\underline{x}_r = \left\{ u \quad w \quad q \quad \theta \quad h \right\}^\top \tag{3.201}$$

For the case of longitudinal only rigid-body motion with an elastic wing, the control inputs are

$$\underline{u} = \left\{ \delta_a \quad \delta_e \right\}^\top$$

where δ_a is aileron deflection and δ_e is elevator deflection.

3.8 Nonlinear Torsional Stiffness

The option to consider nonlinear torsional stiffness is considered. To model the implementation of nonlinear torsional stiffness in [24], an nth-order polynomial is used. The stiffness is described by

$$k_\alpha(\alpha) = \sum_{i=0}^{n} k_{\alpha_i} \alpha^i \tag{3.202}$$

where k_{α_i} are polynomial coefficients

3.9 Freeplay Modeling and Actuator Dynamics

This section discusses the modeling of actuator dynamics and actuator freeplay, and their integration into the two-dimensional and three-dimensional systems. Figure 3.17 shows the flap angle definitions in the presence of a commanded flap deflection and actuator freeplay.

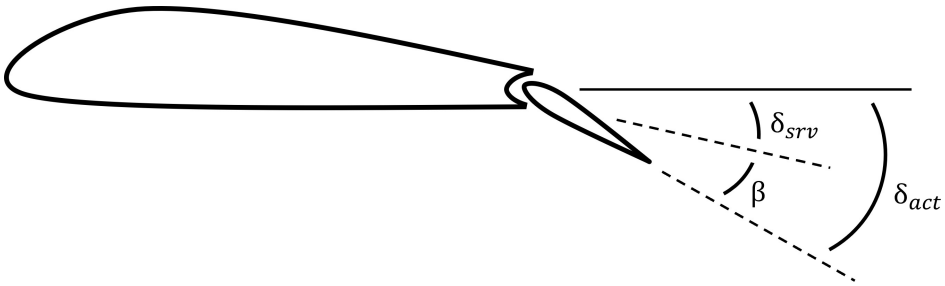

Figure 3.17 Control Surface Deflection Definitions

As indicated, δ_{act} denotes the total or "actual" deflection of the flap with respect to the airfoil chord line, δ_{srv} is the servo position with respect to the chord line, and β is the freeplay deflection angle measured with respect to the servo position. Mathematically, the actual flap position is given by

$$\delta_{act} = \delta_{srv} + \beta \tag{3.203}$$

which simulates the motion of a rigid flap with a flexible attachment.

3.9.1 Actuator Dynamics

To incorporate additional levels of realism into the simulation, actuator dynamics are included in the form of a first-order system or second-order oscillator. For a first-order actuator, the relationship between the commanded actuator position and the real-time servo position is given by the first-order differential equation

$$\dot{\delta}_{srv} + a_{srv}\delta_{srv} = a_{srv}\delta_{cmd} \tag{3.204}$$

where δ_{cmd} is the commanded actuator position, δ_{srv} is the position of the servo given some commanded deflection, and a_{srv} is the servo bandwidth in rad/s. In the case of a very fast actuator, $a_{srv} \gg 1$; then $\delta_{srv} \to \delta_{act}$ and the effects of actuator dynamics are minimal. For a second-order actuator, the relationship between the commanded actuator position and the real-time servo position is given by the second-order differential equation

$$I_\delta \ddot{\delta}_{srv} + c_\delta \dot{\delta}_{srv} + k_\delta \delta_{srv} = k_\delta \delta_{cmd} \tag{3.205}$$

where I_δ is the flap moment of inertia about the hinge line, c_δ is the flap damping coefficient, and k_δ is the flap hinge stiffness. Figure 3.18 shows a comparison of the responses of a fast actuator, first-order actuator, and second-order actuator.

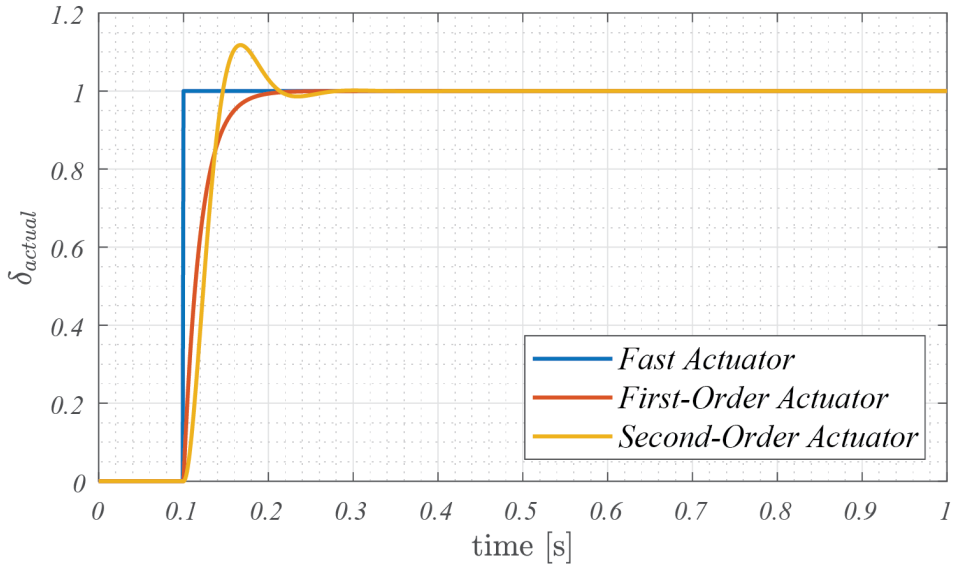

Figure 3.18 Actuator Dynamic Response

Note that this figure illustrates the differences in the response to different types of actuator dynamics and is not representative of the exact dynamics being applied in this work.

3.9.2 Actuator Freeplay

Actuator free-play is a bilinear stiffness in the flap actuator, such that the elastic restoring moment is zero within certain free-play limits. This phenomenon can be mathematically described by

$$M_\beta = \begin{cases} k_\beta(\beta + \beta_{f_r}) & \beta \leq -\beta_{f_r} \\ 0 & -\beta_{f_r} \leq \beta \leq \beta_{f_r} \\ k_\beta(\beta - \beta_{f_r}) & \beta \geq \beta_{f_r} \end{cases}$$

where M_β is the flap elastic restoring moment, β is the freeplay angle (i.e. the flap deflection with respect to servo position), β_{f_r} is the freeplay limit, and k_β is the structural stiffness

of the flap fitting. Figure 3.19 shows the elastic restoring moment with respect to flap deflection.

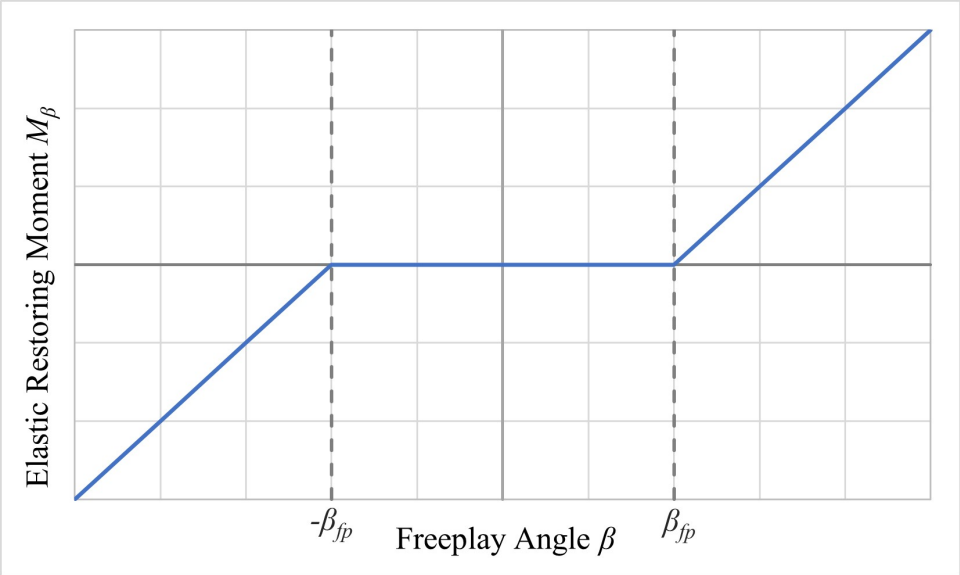

Figure 3.19 Actuator Restoring Moment in the Presence of Freeplay

4 Aerodynamic Modeling

This chapter discusses the aerodynamic modeling efforts of this research. The topics covered include the development of an unsteady vortex-lattice model that calculates time-varying aerodynamic forces and moments on a deforming structural model. This chapter also discusses the implementation of gust loads and atmospheric turbulence.

4.1 Unsteady Vortex-Lattice Modeling

This work utilizes an unsteady vortex-lattice method with ring vortex elements. Wake shed and wake roll-up procedures are included to improve the fidelity of the aerodynamic model. The steps to model aerodynamic panels and the basic principles of the unsteady vortex-lattice solver are described in the following section.

4.1.1 Lifting Surface Definition

The aerodynamic model assumes a lifting surface that is symmetric about the aircraft centerline. Therefore, only the starboard wing is defined and all points are mirrored to generate the aerodynamic panels for the full span model. Figure 4.1 shows the four corner points used to define the lifting surface geometry.

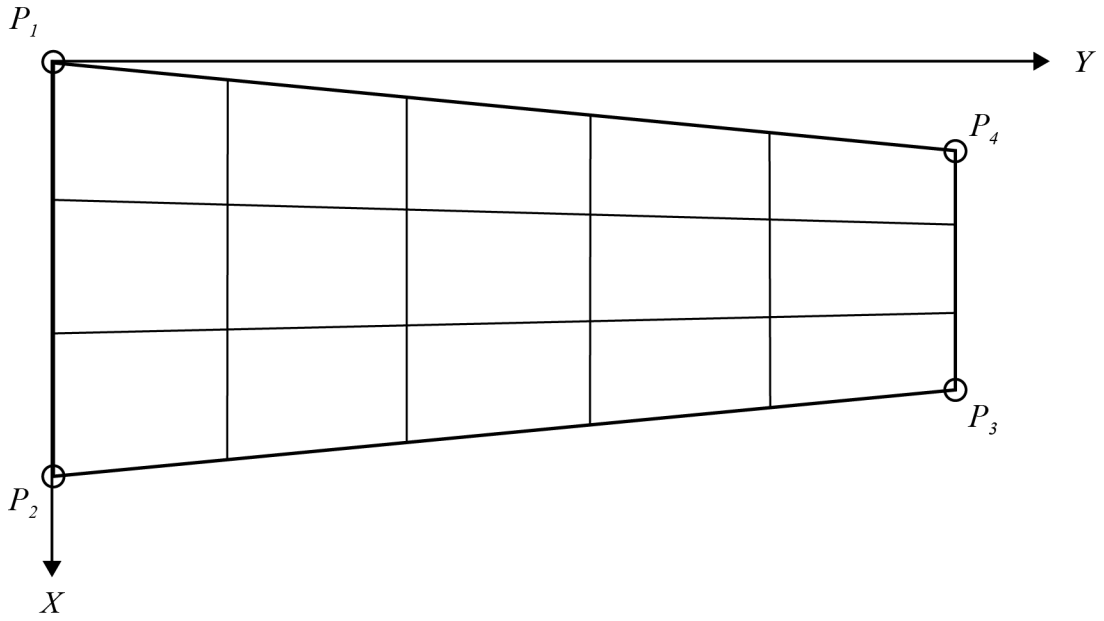

Figure 4.1 Lifting Surface Corner Point Definitions

The corner points are labeled beginning with the inboard leading edge (P_1), and moving counter-clockwise to the outboard leading edge (P_4). Figure 4.2 shows how each of those points are defined. The geometry of the panel can be completely defined by the x, y and z coordinates of the leading edge corner points (P_1 and P_4), the root length (X_{12}), and the tip length (X_{43}). This assumes the root and tip extend only in the x direction, i.e. the aerodynamic panel does not account for twist.

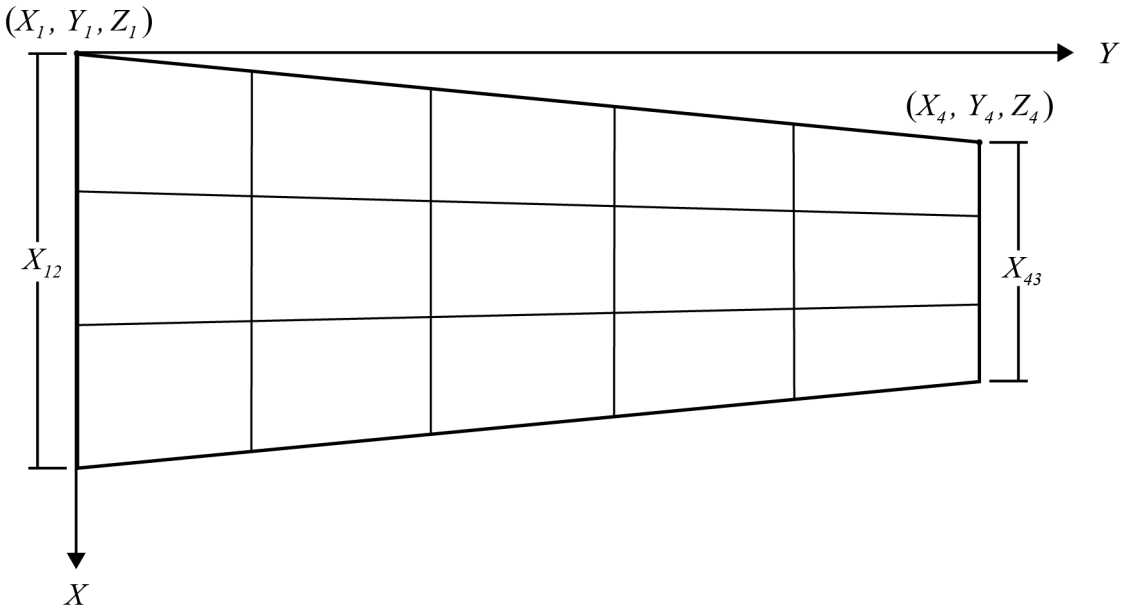

Figure 4.2 Lifting Surface Coordinate Definitions

Next, the panel is discretized into N_c chordwise boxes and N_s spanwise boxes. This brings the total number of boxes in the starboard wing to $N_b = N_s N_c$ and the total number of boxes in the full-span model to $N_{b_{fs}} = 2N_b$. Then, vertices of each box can be defined based on the panel corners and the number of discretizations in the chordwise and spanwise directions. Figure 4.3 shows the box vertex definitions.

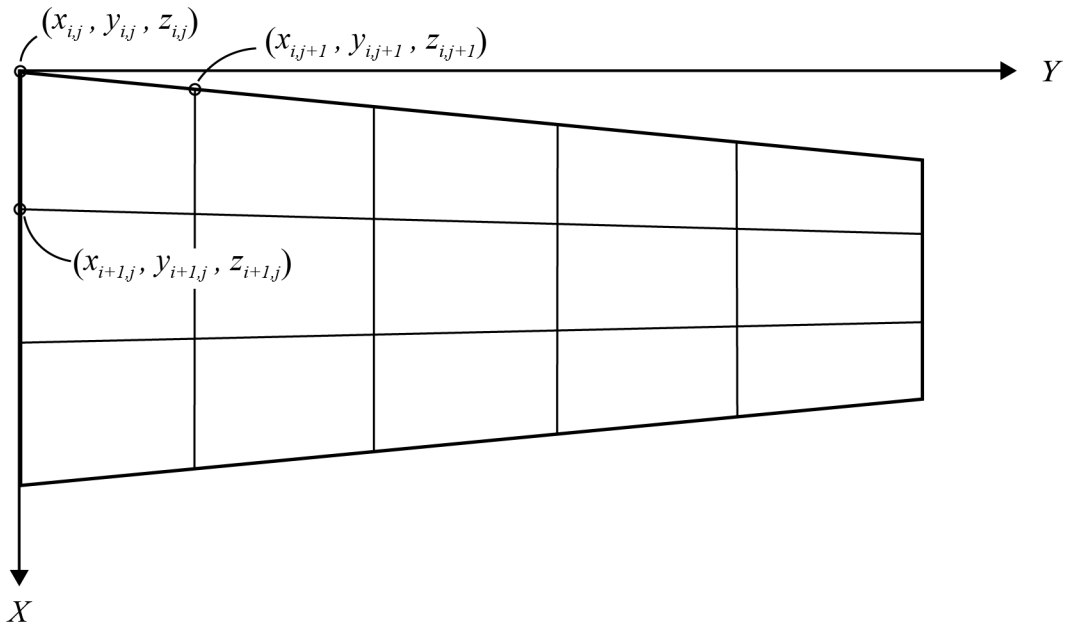

Figure 4.3 Aerodynamic Box Vertex Definitions

To do this, the $x_{i,j}$, $y_{i,j}$, and $z_{i,j}$ coordinates for each vertex are calculated for $1 \leq i \leq N_c + 1$ and $1 \leq j \leq N_s + 1$. Each box contains a control point at the three-quarter chord of the box midspan. Figure 4.4 shows the discretized aerodynamic panel with the aerodynamic boxes and their control points.

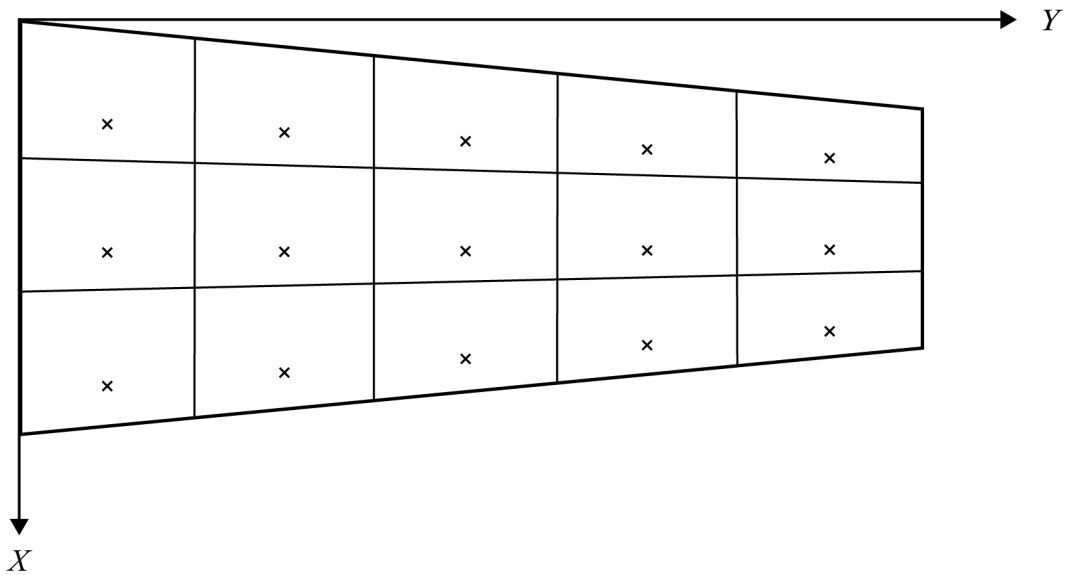

Figure 4.4 Aerodynamic Boxes with Control Points

A ring vortex of strength $\Gamma_{i,j}$ is placed on each box such that the bound vortex segment is aligned with the box quarter-chord. Ring vortex elements are used rather than horseshoe vortices, as the are essential to calculating unsteady aerodynamic forces. The unsteady aerodynamic forces are a result of time-dependent wake vortex strengths, which require the use of rung vortices over horseshoe vortices. Figure 4.5 shows the layout of the ring vortex elements with respect to the aerodynamic boxes

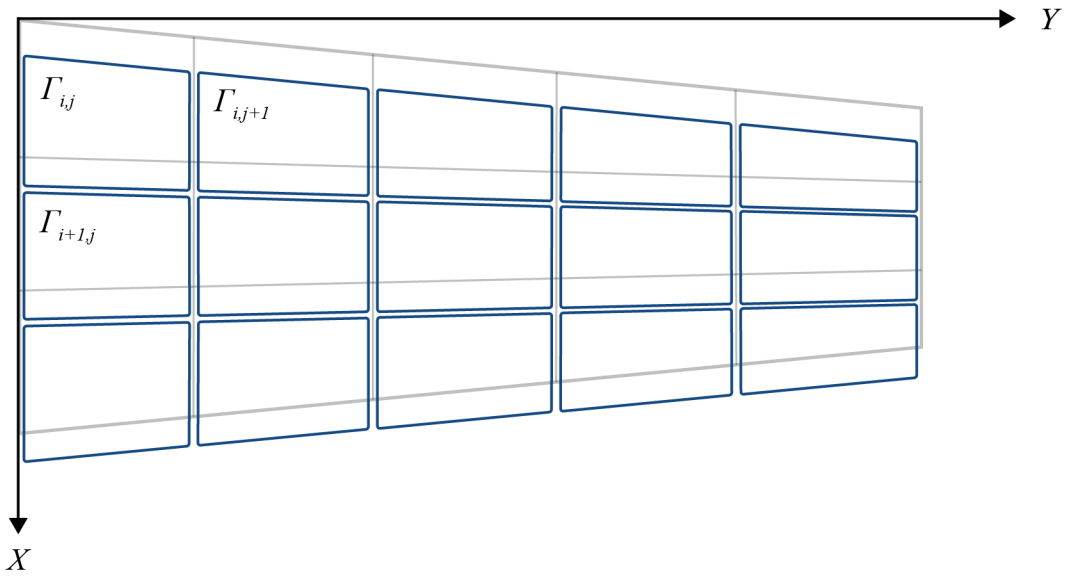

Figure 4.5 Ring Vortex Placement

where $\Gamma_{i,j}$ are the unknown strengths of each ring vortex for $1 \leq i \leq N_c$ and $1 \leq y \leq N_s$. Figure 4.6 (left) shows a ring vortex aligned with a single aerodynamic box. Figure 4.6 (right) shows the labeling convention used when calculating the downwash for each vortex segment.

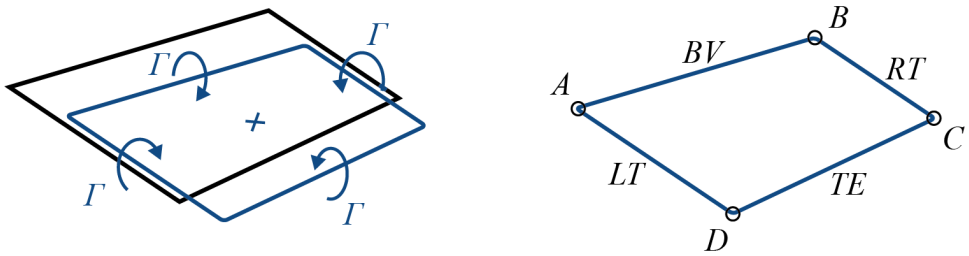

Figure 4.6 Ring Vortex Element and Labeling Convention

Segment AB is referred to as the bound vortex segment (BV), segments AD and BC are the left trailing (LT) and right trailing (RT) vortex segments, respectively, and segment DC is the trailing edge vortex segment (TE). This also shows the control point at the box 3/4 chord point of the box midspan. This is the point at which the flow tangency condition must be satisfied.

4.1.2 Basic Principles

The lifting surface is discretized into a series of aerodynamic boxes, upon which vortex elements of unknown strength are placed. The Biot-Savart law is applied to each vortex segment on every panel to determine its downwash on each control point. This downwash from the jth vortex on the ith control point $w_{i,j}$ is given by

$$w_{i,j} = \oint \frac{\Gamma_j}{4\pi} \frac{d\bar{s} \times \bar{r}_i}{r_i^3} \tag{4.1}$$

where Γ_j is the strength of the jth vortex, $d\bar{s}$ is a differential segment that points along the vortex, and $\bar{r}_i$ is the distance of a segment of the jth vortex ring to the ith control point. Simplifying Eq. (4.1) yields

$$w_{i,j} = \frac{1}{4\pi} \oint \frac{sin\theta_i}{r_i^2} \, ds \, \Gamma_j = A_{i,j} \, \Gamma_j \tag{4.2}$$

where θ_i is the angle the $\bar{r}$ vector makes with the vortex segment and $A_{i,j}$ is the aerodynamic influence coefficient of the jth vortex on the ith panel, given by

$$A_{i,j} = \frac{1}{4\pi} \oint \frac{sin\theta_i}{r_i^2} \, ds \tag{4.3}$$

Figure 4.7 shows the effects of a segment of the jth vortex on the ith control point and illustrates key parameters. It is important to note the sign of $w_{i,j}$, as it depends on the vortex segment being considered. In the configuration shown in Figure 4.7 the bound vortex and left trailing vortex will produce $w_{i,j}$ in the $-z$ direction (into the page). The trailing

edge vortex and right trailing vortex will produce $w_{i,j}$ in the $+z$ direction (out of the page). While this is true for the configuration shown below, it is dependent on the relative position of panel i with respect to panel j and will change.

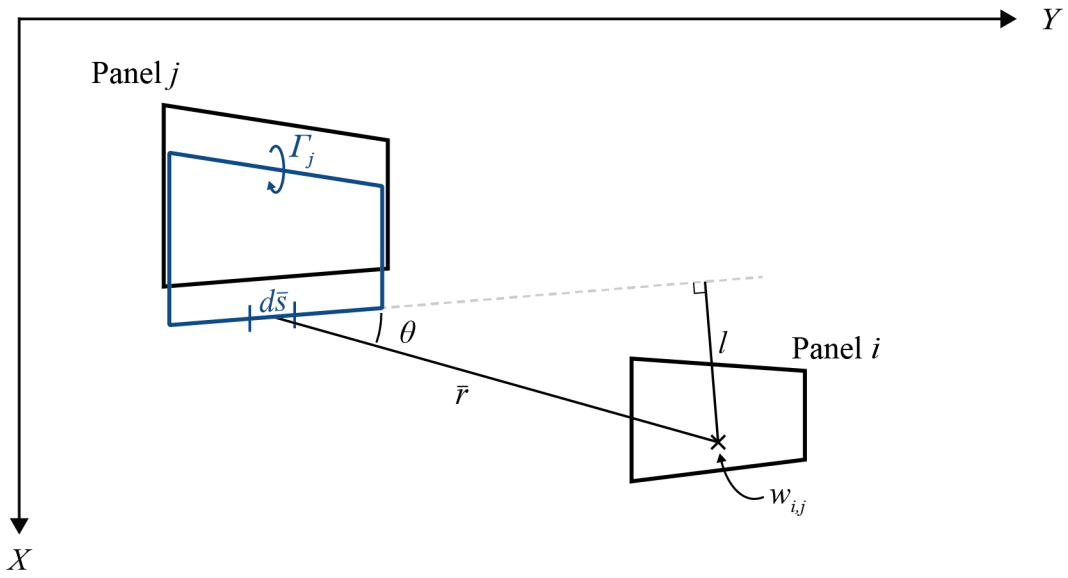

Figure 4.7 Aerodynamic Influence of jth Vortex on the ith Box

To simplify the calculations, a new length l is defined. The length l is the perpendicular distance from the vortex segment to the control point. For a single segment of the ring vortex, the following relationships apply

$$r = \frac{l}{sin\,\theta} \tag{4.4}$$

$$s = -\frac{l}{tan\,\theta} \tag{4.5}$$

Therefore,

$$ds = \frac{l}{sin^2\,\theta}\,d\theta \tag{4.6}$$

Substituting Eq. (4.4) through Eq. (4.6) into Eq. (4.3) gives

$$(A_{i,j})_x = \frac{1}{4\pi\,l}\int_{\theta_i}^{\theta_f} sin\,\theta\,d\,\theta \tag{4.7}$$

where $(A_{i,j})_x$ is the influence of a single segment of the vortex ring, θ_i is the angle formed by $\bar{s}$ and $\bar{r}$ at the starting point of the vortex segment, and θ_f is the angle formed by $\bar{s}$ and $\bar{r}$ at the ending point of the vortex segment. The angle θ is calculated using the properties of a dot product. The vector $\bar{s}$ is defined such that it points in the direction of the vortex segment (positive being in the CCW direction). Then, the angle θ is calculated using

$$\theta = cos^{-1}\left(\frac{\bar{r}\cdot\bar{s}}{r\,s}\right) \tag{4.8}$$

By evaluating Eq. (4.7) on each segment of the vortex ring, the net aerodynamic influence can be calculated. The aerodynamic influence of the bound vortex segment is

$$A_{BV} = \frac{1}{4\pi\,l}(cos\theta_b - cos\theta_a) \tag{4.9}$$

where θ_a and θ_b are the angles formed by $\bar{s}$ and $\bar{r}$ when $\bar{r}$ originates from point A and ends at point B on the ring vortex, as defined in Figure 4.6. It follows that the aerodynamic influence of the right trailing vortex is

$$A_{RT} = \frac{1}{4\pi\,l}(cos\theta_c - cos\theta_b) \tag{4.10}$$

the aerodynamic influence of the trailing edge vortex is

$$A_{TE} = \frac{1}{4\pi\,l}(cos\theta_d - cos\theta_c) \tag{4.11}$$

and the aerodynamic influence of the left trailing vortex is

$$A_{LT} = \frac{1}{4\pi\,l}(cos\theta_a - cos\theta_d) \tag{4.12}$$

Then, the net aerodynamic influence of the jth vortex on the ith panel is

$$A_{i,j} = (A_{BV} + A_{RT} + A_{TE} + A_{LT}) \tag{4.13}$$

The total downwash on the ith aerodynamic box due to all vortices is

$$w_i = \sum_{j=1}^{N} A_{i,j}\,\Gamma_j \tag{4.14}$$

where w_i is the scalar value of the total downwash on the ith panel due to all vortices, $A_{i,j}$ is a $1 \times N_b$ vector containing the aerodynamic influence coefficient for each vortex on the ith panel, and Γ_j is an $N_b \times 1$ vector of vortex strengths. For the entire wing (i.e. $1 \leq i \leq N_b$), Eq. (4.14) becomes

$$w = A\,\Gamma \tag{4.15}$$

where $w \in \mathbb{R}^{N_b \times 1}$ is vector of box downwashes at time t, $A \in \mathbb{R}^{N_b \times N_b}$ is a matrix of aerodynamic influence coefficients at time t, and $\Gamma \in \mathbb{R}^{N_b \times 1}$ is a vector of vorticities at time t. For a rigid wing, the aerodynamic influence matrix A will be constant. In the case of the elastic wing, A will change as the distance between vortex segments and control points changes at each time step. The vorticity of each vortex ring is found by utilizing

$$\Gamma = A^{-1} w \tag{4.16}$$

and applying the flow tangency condition at all control points

$$V_n = 0 \tag{4.17}$$

such that the sum of the velocities normal to the panel must be zero. This includes the normal component of freestream velocity, the downwash from each vortex element, and the normal component of any perturbations such as atmospheric turbulence. For a simple rigid

wing, this becomes

$$w = V_\infty sin\alpha \tag{4.18}$$

where α is the wing angle of attack. For boxes designated as control surface boxes, the flow tangency condition becomes

$$w = V_\infty sin(\alpha + \delta) \tag{4.19}$$

where δ is the control surface deflection. Figure 4.8 shows the normal velocity at a series of panels when considering angle of attack and control surface deflection.

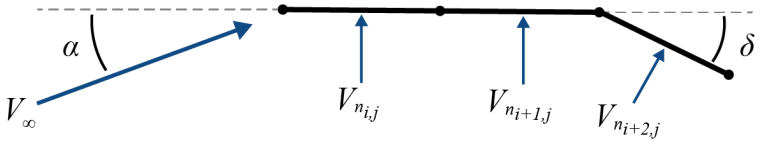

Figure 4.8 Panel Normal Velocity

If a gust or turbulence is also considered, the normal component of the respective perturbation is added to the right hand side of Eq. (4.19). Now that the downwash on each panel is established, the strength of each vortex ring is determined using Eq. (4.16). Finally, the lift on each box (L_{b_i}) is calculating using the Kutta-Jukowski Theorem

$$L_{b_i} = \rho V_\infty \Gamma_i \Delta y \tag{4.20}$$

where Γ_i is the net vorticity on the quarter-chord of the ith panel and Δy is the panel width. When using vortex ring elements as opposed to horseshoe vortices, some modifications to Eq. (4.20) are required. Figure 4.9 shows the effect of two ring vortices with coincident trailing edge and bound vortex segments on a panel with a width of $2s$.

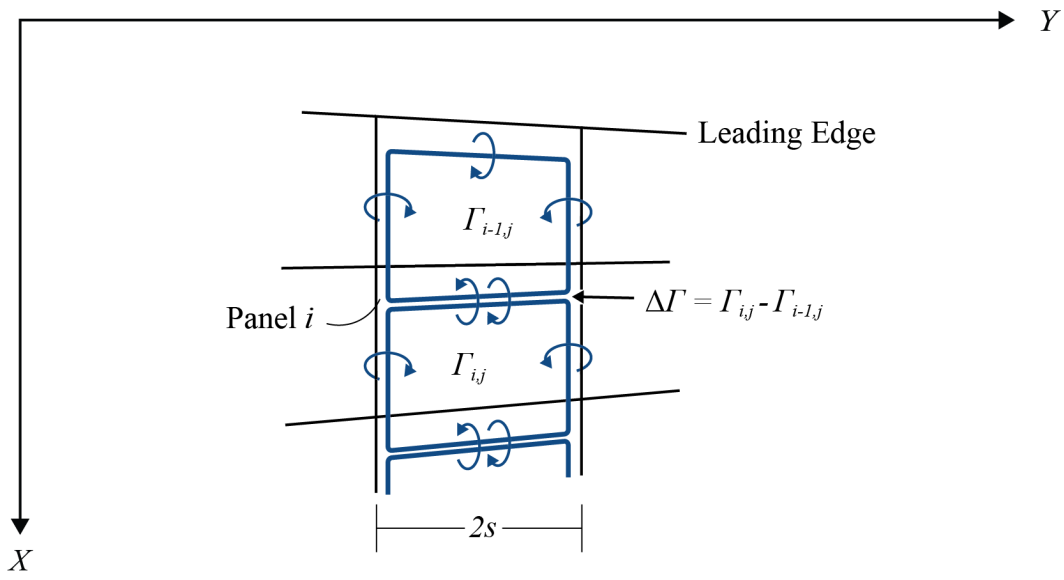

Figure 4.9 Net Vorticity on Aerodynamic Box

This occurs for all panels that do not lie on the leading edge. In this case, the net vorticity on the quarter-chord of the ith box is

$$\Delta\Gamma_i = \Gamma_{i,j} - \Gamma_{i-1,j} \tag{4.21}$$

If panel i is on the leading edge, there are no overlapping vortex elements and thus the vorticity is

$$\Delta\Gamma_i = \Gamma_{i,j} \tag{4.22}$$

Then, the lift on the ith panel is

$$L_{b_i} = \rho V_\infty \Delta\Gamma_i (2s) \tag{4.23}$$

Similarly, the induced drag on each box is calculated using

$$D_{i_b} = \rho w_i \Delta\Gamma_i (2s) \tag{4.24}$$

While the drag is generally not used in simple simulations, it becomes useful when simulating

an elastic aircraft. The final step in the loads calculation is determining the direction of the force vector. For a rigid aerodynamic panel, the calculation is very simple, as all box normal vectors point in the same direction. Furthermore, the box areas can be used to calculate other quantities of interest, such as pressure coefficients. The box normal vectors $\hat{n}$ and areas S are depicted in Figure 4.10.

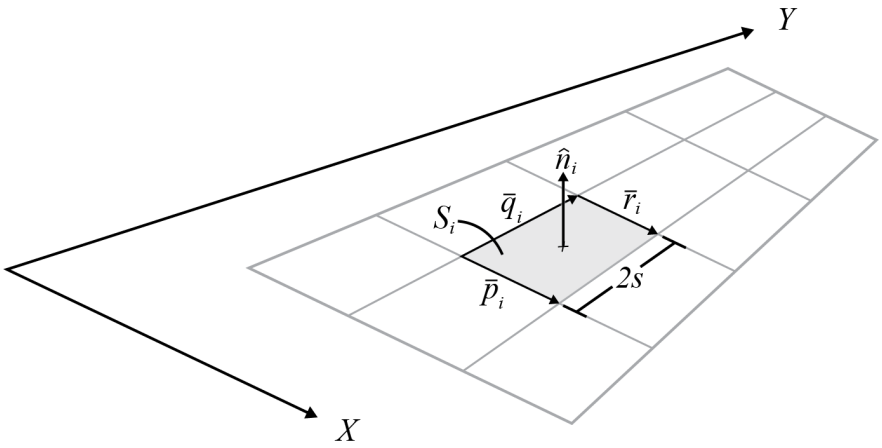

Figure 4.10 Aerodynamic Box Normal Vector and Area

With the vertices of each box known, vectors $\bar{p}_i$, $\bar{q}_i$, and $\bar{r}_i$ can be defined. Then, the normal vector of the ith box is

$$\hat{n}_i = \frac{\bar{p}_i \times \bar{q}_i}{|\bar{p}_i \times \bar{q}_i|} \tag{4.25}$$

and the area of the ith box is

$$S_i = \frac{1}{2}(p + r)(2s) \tag{4.26}$$

4.1.3 Considerations for an Elastic Wing

If the wing is elastic, additional bending and twist must be considered, which alter the aerodynamic calculations. The elastic motion changes the position of the aerodynamic boxes such that they are no longer coplanar. Figure 4.11 shows an aerodynamic panel that has been deformed due to wing bending and torsion.

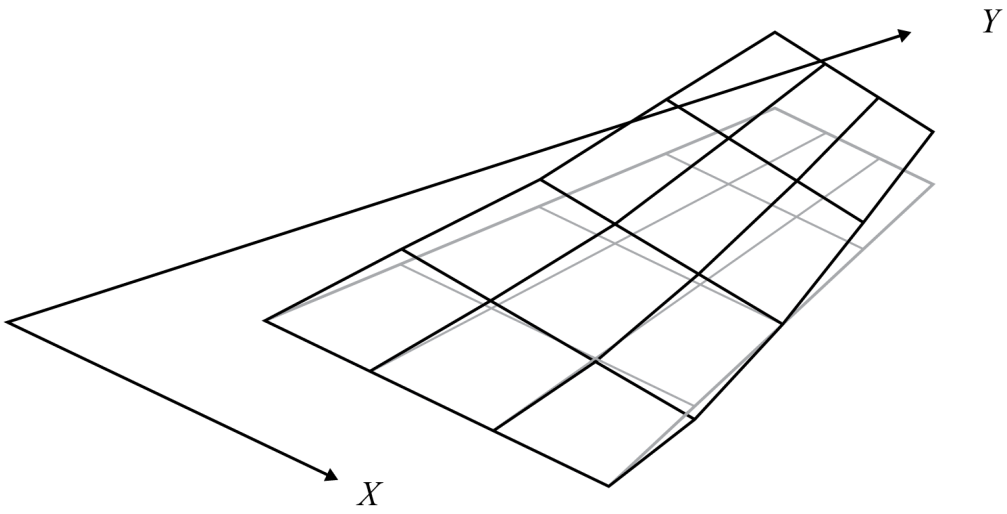

Figure 4.11 Aerodynamic Panel Subject to Bending and Torsion

When the wing is deformed, the vortex segments change position with respect to one another. Due to this effect, the aerodynamic influence coefficients must be recalculated at each timestep. Another side-effect of the elastic deformation is that the downwash induced by the vortex elements is no longer strictly normal to a given aerodynamic box. Figure 4.12 shows the aerodynamic influence of panel j onto panel i for a deformed wing.

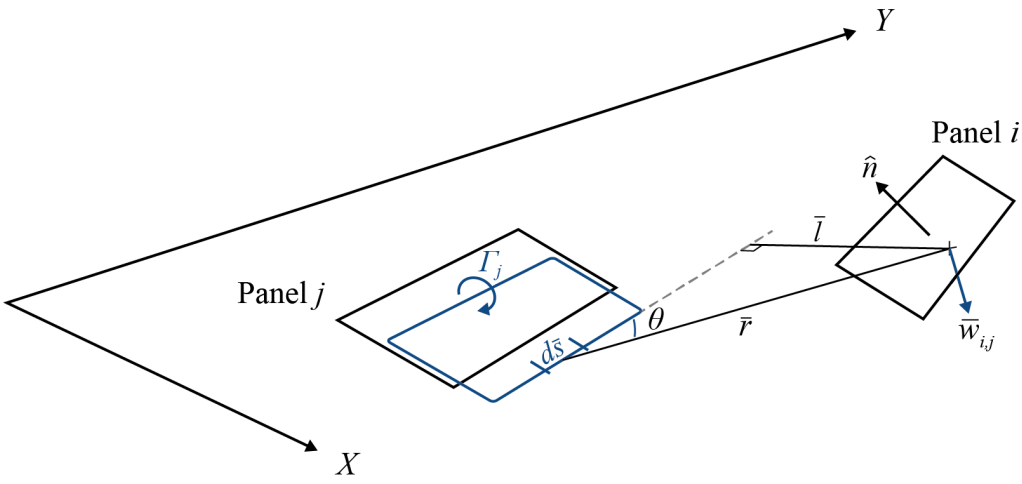

Figure 4.12 Aerodynamic Influence of the jth Vortex on the ith Box of a Deformed Wing

As the panels no longer share the same orientation, special care must be taken when calculating the normalwash on each panel.

Once the deformed shape of the panel is known, the net aerodynamic force from each mode can be determined. Due to the linear nature of the vortex-lattice solution, the incremental force from each mode can be determined in the integration step. At each timestep, the generalized displacements and rates are calculated for each retained mode and converted back into physical coordinates. Using this, the normalwash contribution from each mode can be calculated. Then, the vorticity using Eq. (4.16) and the force is calculated using Eq. (4.23).

4.1.4 Control Surface Definition

A single control surface is defined by designating a portion of the aerodynamic boxes as control surface elements that can be rotated about their forward edge, which defines the hinge line. Figure 4.13 shows the control surface (shaded) and its hingeline, which lies on the leading edge of the specified boxes.

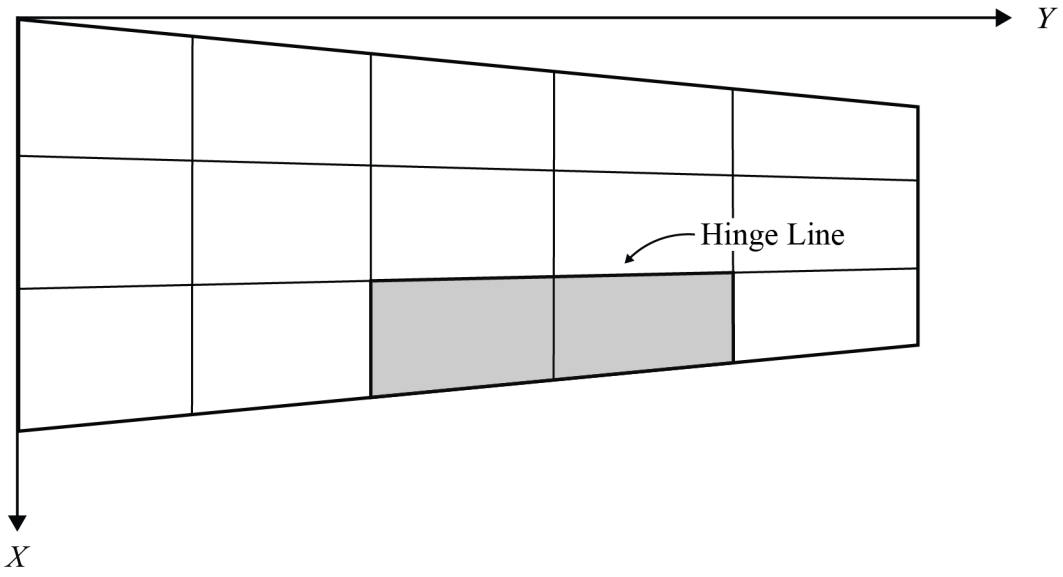

Figure 4.13 Aerodynamic Panel Control Surface Definition

The control surface boxes are rotated about the hingeline by some angle prescribed by the control system. The change in aerodynamic force and moment is calculated during the vortex-lattice procedure.

4.2 Gust and Turbulence Loads

This section discusses the modeling and implementation of gust loads and turbulence loads to act as exogenous disturbances to the system.

4.2.1 Gust Modeling

A 1-cos (referred to as a "one minus cosine") gust is modeled in accordance with 14 CFR §25.341. The gust velocity w_g is given by

$$w_g = \frac{U_{ds}}{2}\left[1 - cos\left(\frac{\pi s_p}{H}\right)\right] \tag{4.27}$$

where U_{ds} is the design gust velocity, s_p is the penetration distance into the gust, and H is the gust gradient (the distance for the gust to reach its peak velocity). The design gust velocity is calculated using

$$U_{ds} = U_{ref} F_g \left(\frac{H}{350}\right)^{1/6} \tag{4.28}$$

where U_{ref} is the reference gust velocity and F_g is the flight profile alleviation factor. A detailed description of the gust calculation process can be found in 14 CFR §25.341 [34]. For the purposes of this work, the gradient length and gust amplitude can be scaled to achieve a desired frequency response. Figure 4.14 shows the sinusoidal gust velocity profile (w_g) with an aircraft at penetration distance s_p into the gust at penetration time t_p.

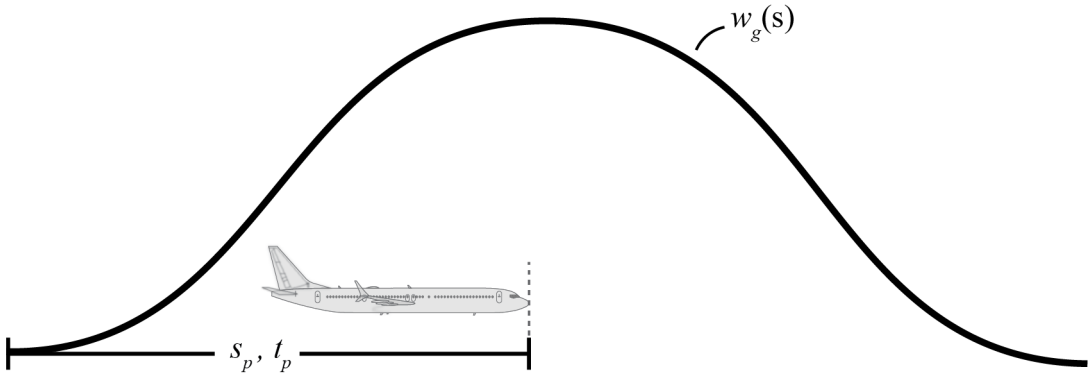

Figure 4.14 Gust Penetration Distance and Time

In this analysis, the gust profile is generated prior to the simulation and propagated over the model with each timestep. Figure 4.15 shows the propagation of the gust profile over a single aerodynamic box with each timestep.

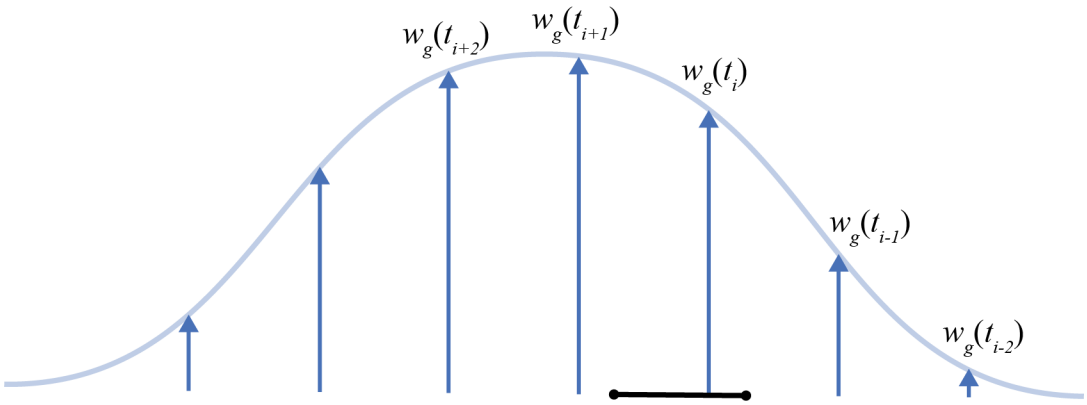

Figure 4.15 Gust Propagation Over an Aerodynamic Box

At time t the box is subjected to the vertical gust velocity $w_g(t_i)$. At the previous timestep, the box was subjected to the velocity $w_g(t_{i-1})$ and at the next timestep the box will be subjected to $w_g(t_{i+1})$. The velocities are determined by interpolating the position of the control point onto the spatial position of the gust.

4.2.2 Turbulence Modeling

The von Kármán power spectral density function is used to model turbulence loads in accordance with 14 CFR §25.341. The power spectral density of the turbulence as a function of frequency is given by

$$\Phi(\Omega) = \frac{L}{\pi} \frac{1 + \frac{8}{3}(1.339\Omega L)^2}{[1 + (1.339\Omega L)^2]^{11/6}} \tag{4.29}$$

where L is the turbulence length scale and Ω is the reduced frequency. Per 14 CFR §25.341, $L = 2500ft$. The application of turbulence to the aerodynamic boxes is the same process as described in Figure 4.15.

4.2.3 Wake Shed Procedure

With the use of ring vortices, the wake is developed by shedding the trailing edge vortex at each timestep and allowing it to propagate downstream. Figure 4.17 illustrates the wake

shedding process.

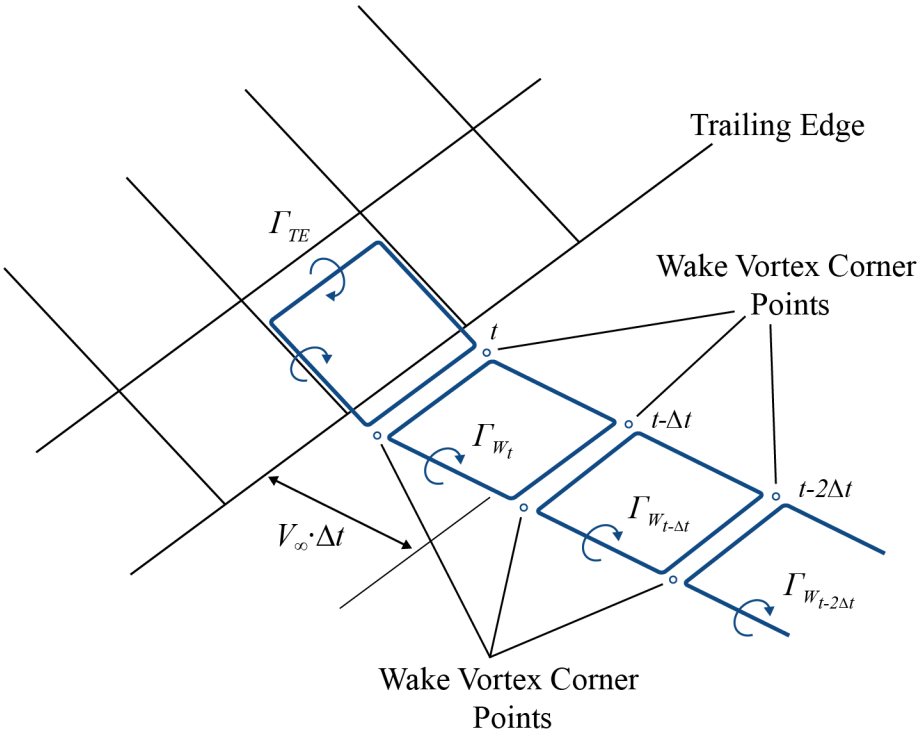

Figure 4.16 Ring Vortex Wake Propagation [2]

At the end of each timestep, a new set of ring vortex corner points is generated at distance $d = V_\infty \, \Delta t$ downstream of the aft-most wake vortex. This creates a new set of corner points that define a new wake vortex element. At each timestep, each wake element propagates in the direction of flow as a new wake vortex ring is shed from the trailing edge. The strength of the most recently shed vortex (Γ_{W_t}) is equal to the strength of the trailing edge vortex from the previous timestep:

$$\Gamma_{W_t} = \Gamma_{TE_{t-\Delta t}} \tag{4.30}$$

Once the vortex is shed, its strength remains constant as it propagates downstream and moves with the local flow velocity. This is the unsteady form of the Kutta condition [2].

4.2.4 Wake Roll-Up Procedure

As previously discussed, the ring vortices in the wake are free vortex elements such that their individual vortex strengths do not change once they are shed from the trailing edge.

However, the vorticity of each vortex induces a local flow velocity felt by every other ring vortex. The result is a rolling up of the wake as it propagates downstream, forming trailing vortices and causing the wake vortex sheet to descend with downstream distance. Figure 4.17 depicts the wake roll-up.

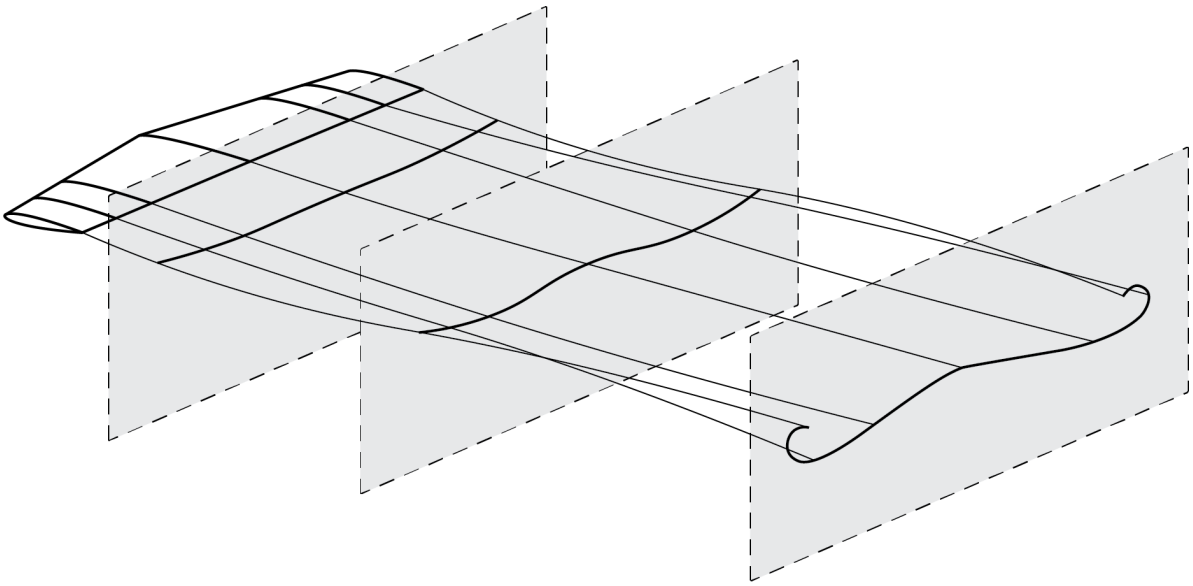

Figure 4.17 Wake Roll-up [2]

4.3 Application to Structure

Once the aerodynamic forces on each box are calculated for a given timestep, they are applied to the structure. The resulting shear force, bending moment, and torsional moment about the elastic axis deform the structure for the next timestep. The lift, torsional moment, and hinge moment at each mass element are calculated and applied in the form of modal forcing.

For use in the structural dynamics equations of motion, the aerodynamics can be separated into the contribution from each mode as previously discussed. The lift at time t due to each mode can be calculated by determining the normalwash on each panel for a given mode; for example,

$$L_{\dot{h}_i}(t) = \rho V_\infty (A(t)^{-1} w_{\dot{h}_i}(t))(2s) \tag{4.31}$$

where $L_{\dot{h}_i}$ is the lift contribution from the ith bending rate and $w_{\dot{h}_i}$ is a vector of nor-

malwashes at each panel due to the ith bending rate. It is important to note that, while the matrix of aerodynamic influence coefficients A is typically time-invariant, for an elastic structure it becomes time dependent. The total lift on the wing is

$$L = L_0 + L_v + \sum_{i=1}^{N_h} L_{\dot{h}_i} + \sum_{j=1}^{N_\alpha} L_{\alpha_j} + \sum_{j=1}^{N_\alpha} L_{\dot{\alpha}_j} + L_\beta + L_{\dot{\beta}} + L_\delta \tag{4.32}$$

For the steady-state condition, the dynamic contributions go to zero. The steady-state lift then becomes

$$L_{ss} = L_0 + L_v + \sum_{j=1}^{N_\alpha} L_{\alpha_{ss_j}} + L_{\beta_{ss}} + L_{\delta_{ss}} \tag{4.33}$$

and the perturbation lift is

$$\Delta L_i = \Delta L_{\dot{h}_i} + \sum_{j=1}^{N_\alpha} \Delta L_{\alpha_j} + \sum_{j=1}^{N_\alpha} \Delta L_{\dot{\alpha}_j} + \Delta L_\beta + \Delta L_{\dot{\beta}} + \Delta L_\delta \tag{4.34}$$

The perturbation moment about the elastic axis (ΔM_e) and perturbation hinge moment (ΔT_e) are calculated using a similar process such that

$$\Delta M_{e_j} = \sum_{i=1}^{N_h} \Delta M_{e_{h_i}} + \Delta M_{e_{\alpha_j}} + \Delta M_{e_{\dot{\alpha}_j}} + \Delta M_{e_\beta} + \Delta M_{e_{\dot{\beta}}} + \Delta M_{e_\delta} \tag{4.35}$$

and

$$\Delta T_e = \sum_{i=1}^{N_h} \Delta T_{e_{\dot{h}_i}} + \sum_{j=1}^{N_\alpha} \Delta T_{e_{\alpha_j}} + \sum_{j=1}^{N_\alpha} \Delta T_{e_{\dot{\alpha}_j}} + \Delta T_{e_\beta} + \Delta T_{e_{\dot{\beta}}} + \Delta T_{e_\delta} \tag{4.36}$$

While the aerodynamic forces are a function of the elastic motion, the aerodynamic stiffness and damping matrices are not as evident as in the two-dimensional case. This is because the outputs of the unsteady vortex-lattice solution are time dependent forces and not force coefficients. That is,

$$L(t_i) = L_{\dot{h}}(t_i) + L_\alpha(t_i) + L_{\dot{\alpha}}(t_i) + L_\beta(t_i) + L_{\dot{\beta}}(t_i) + L_{\dot{\beta}}(t_i) \tag{4.37}$$

and not

$$L(t_i) = C_{L_{\dot{h}}}\dot{h}(t_i) + C_{L_\alpha}\alpha(t_i) + C_{L_{\dot{\alpha}}}\dot{\alpha}(t_i) + C_{L_\beta}\beta(t_i) + C_{L_{\dot{\beta}}}\dot{\beta}(t_i) \tag{4.38}$$

which cannot be easily put into the form

$$\underline{F}_a(t) = [M_a]\underline{\ddot{x}}(t) + [C_a]\underline{\dot{x}}(t) + [K_a]\underline{x}(t) + [F_\delta]\delta(t) \tag{4.39}$$

Therefore, it is simply represented as the linear function

$$\underline{F}_a(t) = \underline{f}(\underline{x}(t), \underline{\dot{x}}(t), \delta(t)) \tag{4.40}$$

which then yields the linear system

$$\begin{Bmatrix} \underline{\dot{x}}(t) \\ \underline{\ddot{x}}(t) \end{Bmatrix} = \begin{bmatrix} [0] & [I] \\ -[M_s]^{-1}[K_s] & -[M_s]^{-1}[C_s] \end{bmatrix} \begin{Bmatrix} \underline{x}(t) \\ \underline{\dot{x}}(t) \end{Bmatrix} + \begin{bmatrix} [0] \\ [M_s]^{-1}\underline{F}_a(t) \end{bmatrix} \tag{4.41}$$

4.4 Complete Aeroelastic Equations of Motion

Various methods can be used to simulate the aeroelastic system. For a wing only, the system is inherently linear, so the equations of motion can be simulated through direct calculation of Eq. (4.41). For a full airplane, it is necessary to decompose the system into its elastic steady-state and perturbation states. This will take the form

$$\underline{x} = \underline{x}_{ss} + \underline{\Delta x} \tag{4.42}$$

where $\underline{x}_{ss}$ are the equilibrium displacements and rates (which tend to zero), and $\underline{\Delta x}$ are the perturbations from the steady-state. The equations of motion become

$$[M_s]\left(\underline{\ddot{x}}_{ss} + \underline{\Delta\ddot{x}}\right) + [C_s]\left(\underline{\dot{x}}_{ss} + \underline{\Delta\dot{x}}\right) + [K_s]\left(\underline{x}_{ss} + \underline{\Delta x}\right) = \left(\underline{F}_{ss} + \underline{\Delta F}\right) \tag{4.43}$$

which simplifies to

$$[M_s]\,\underline{\Delta\ddot{x}} + [C_s]\,\underline{\Delta\dot{x}} + [K_s]\,\underline{\Delta x} = \underline{\Delta F} \tag{4.44}$$

which describes the perturbation of the cantilevered wing about the elastic equilibrium position.

5 Model Validation

This section discusses the model validation for the uncoupled mode prediction and flutter speed determination algorithm used in this research. This includes the structural model, the mass model, and the aerodynamic model used to perform aeroelastic analyses.

5.1 Model

The model used to validate the mode prediction is given by Bisplinghoff, Ashley, and Halfman in [1]. The jet transport wing is used to study various mode shape determination methods and flutter prediction techniques. This geometry is also used as a case study for the Nastran aeroelastic flutter solution method. A Matlab code was written to perform the modal analysis, structural dynamics calculations, unsteady-vortex lattice aerodynamics, and aeroelastic calculations. The results are compared to Nastran, which acts as the source of truth model.

Figure 5.1 shows the jet transport wing mass distribution and aerodynamic layout as described in [14]. The structure is represented by the elastic axis at 35% chord and a series of dumbbell masses at five spanwise locations.

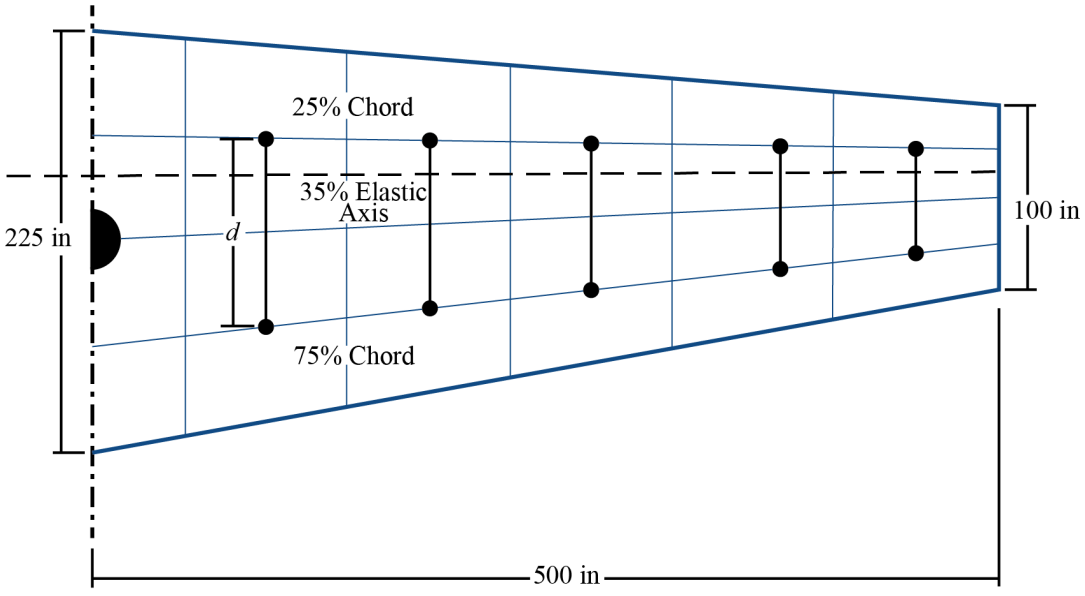

Figure 5.1 Jet Transport Wing Layout [1]

For this configuration, the structural data are listed in Table 5.1.

Table 5.1 Jet Transport Structural Data

Station (in)	M (lb_f)	I_α $(lb_f \cdot in^2)$	S_α $(lb_f \cdot in)$	m (lb_f)	d (in)
0	17,400	∞	-	17,400	-
90	6,030	8.72×10^6	-42,273	3,019.5	74.7
186	10,200	93.16×10^6	-140,083	5,100	189.15
268	4,200	3.72×10^6	8,400	2,100	59.39
368	3,400	2.77×10^6	6,800	1,700	56.95
458	680	0.40×10^6	2,720	340	47.84

In [1], the bending and torsional stiffness of the wing are graphically provided. This is recreated as Figure 5.2 and placed here for convenience. Recall, for slender beams, the shear stiffness GK is ignored.

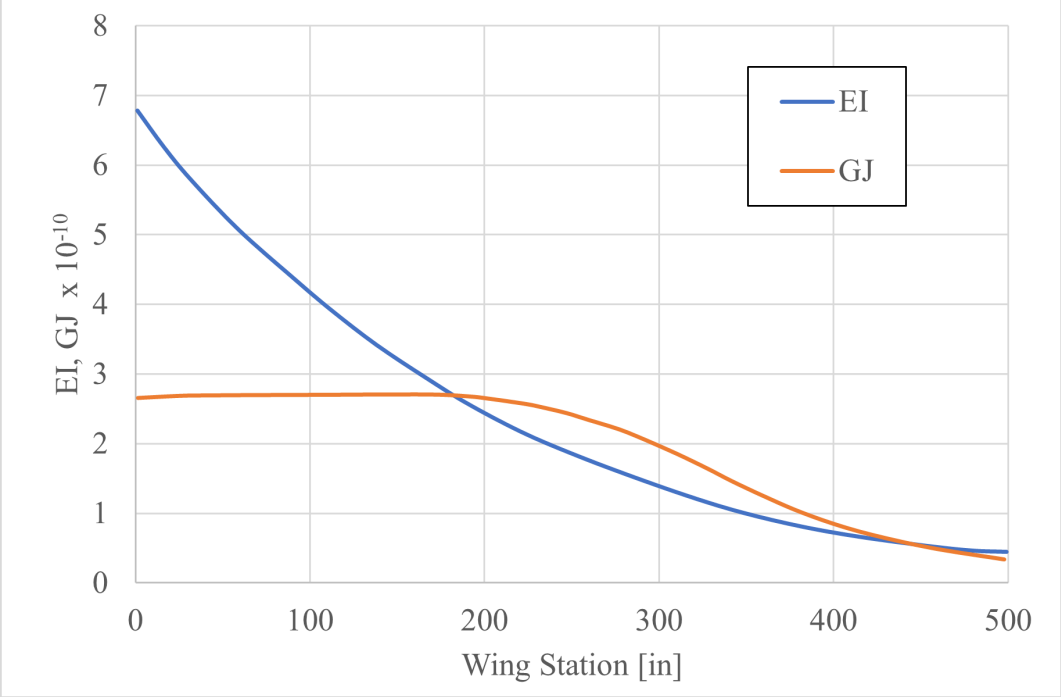

Figure 5.2 BAH Bending and Torsional Stiffness Curves [1]

The system of dumbbell masses is simplified such that it is amenable to the structural dynamics calculation method used in this research. The lumped masses are concentrated about the elastic axis such that each spanwise station has equivalent mass, mass moment of inertia, and static imbalance. The section properties along the elastic axis remain unchanged.

Figure 5.3 presents the simplified jet transport wing used to validate the structural dynamics and aeroelastic solution capabilities of the Matlab code used in this research.

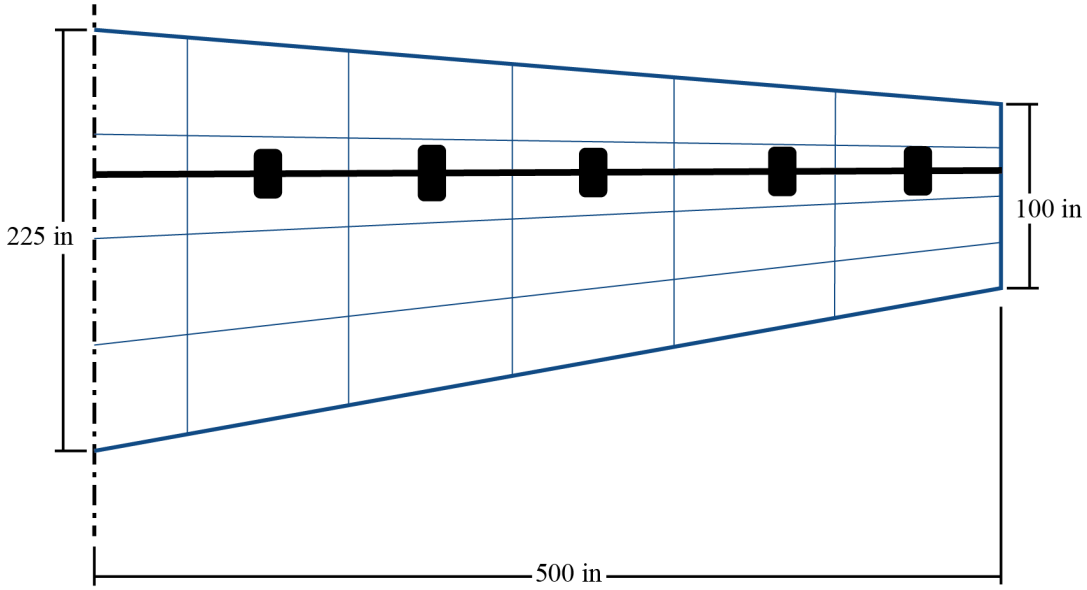

Figure 5.3 Simplified Jet Transport Wing Layout

Once the structure and aerodynamic panels are defined, the modal solution and flutter solution can be validated against the Nastran results.

5.1.1 Uncoupled Mode Approximation

The uncoupled modes are calculated using the method described in Section 3.4. The first five modes are summarized and compared against Nastran in Table 5.2. Only the first five modes are compared as these are the modes retained in the Nastran flutter solution.

Table 5.2 Comparison of Natural Frequencies

Mode No. -	Label -	Nastran Freq. (Hz)	Matlab Freq. (Hz)	Error -
1	First Bending	2.04	2.11	3.43%
2	First Torsion	3.55	3.56	0.28%
3	Second Bending	7.28	7.44	2.19%
4	Third Bending	11.70	13.14	13.39%
5	Second Torsion	14.88	14.80	0.47%

The results show strong agreement in the lower frequency modes with the error increasing

with the third bending mode, as expected for a system with only five discretizations. Figure 5.4 shows a comparison of the first bending mode shape as calculated by Matlab and Nastran.

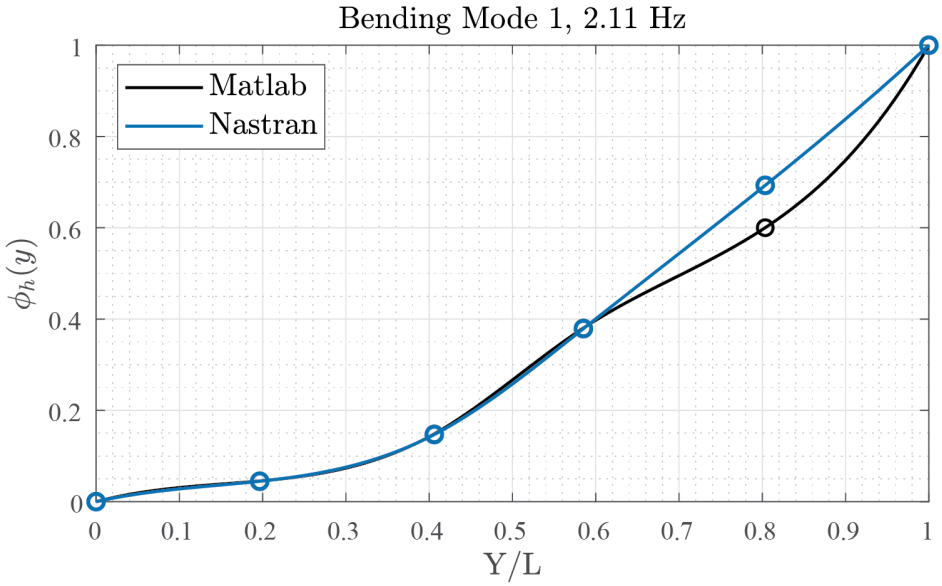

Figure 5.4 Comparison of First Bending Mode Shape

Figure 5.5 shows a comparison of the second bending mode shape as calculated by Matlab and Nastran.

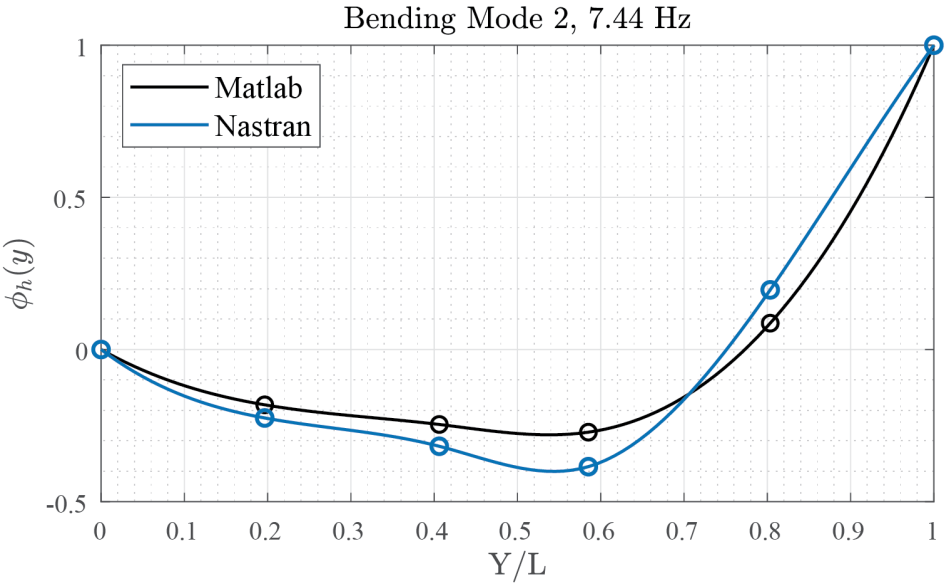

Figure 5.5 Comparison of Second Bending Mode Shape

Figure 5.6 shows a comparison of the third bending mode shape as calculated by Matlab

and Nastran.

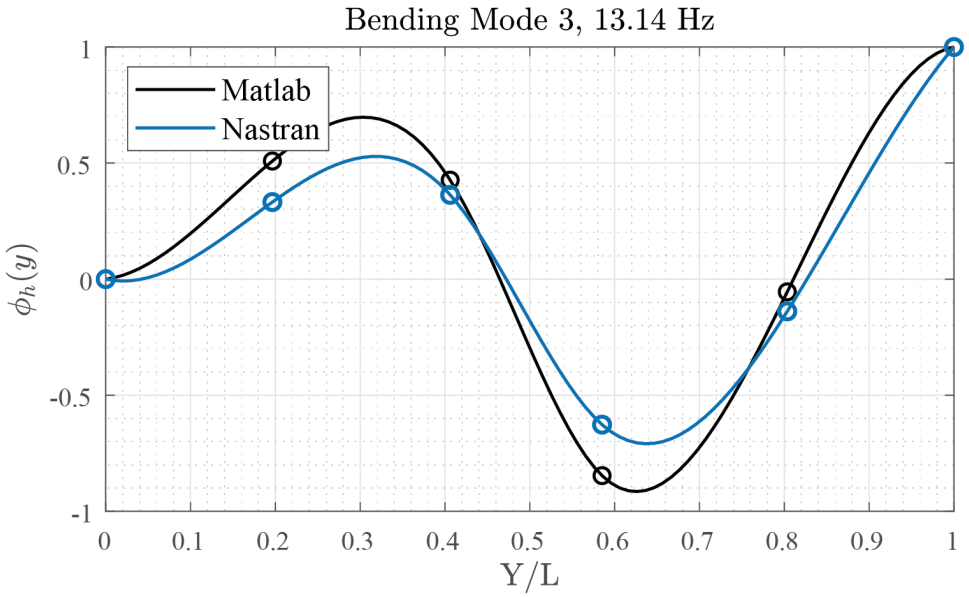

Figure 5.6 Comparison of Third Bending Mode Shape

Figure 5.7 shows a comparison of the first torsion mode shape as calculated by Matlab and Nastran.

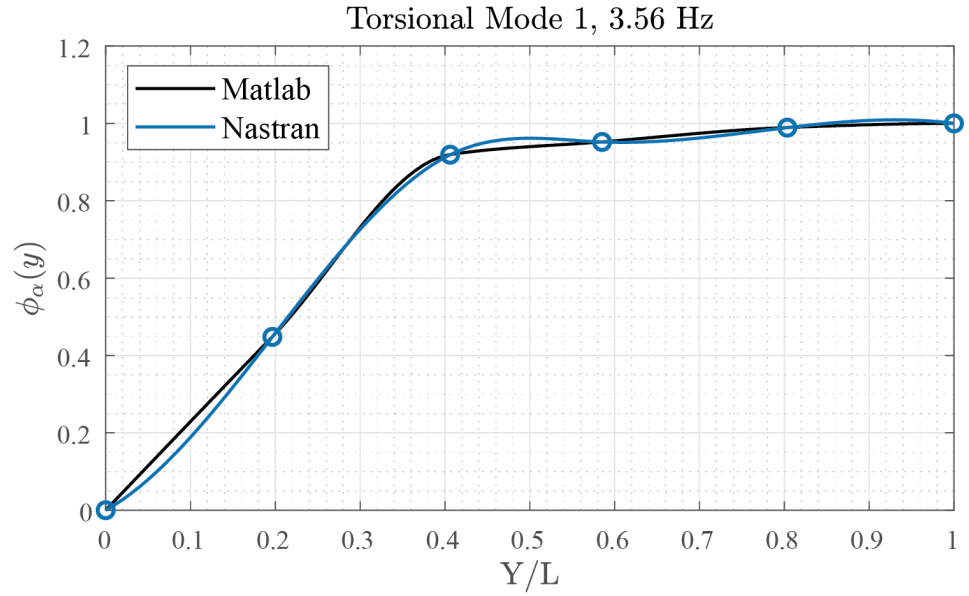

Figure 5.7 Comparison of First Torsion Mode Shape

Figure 5.8 shows a comparison of the first torsion mode shape as calculated by Matlab and Nastran.

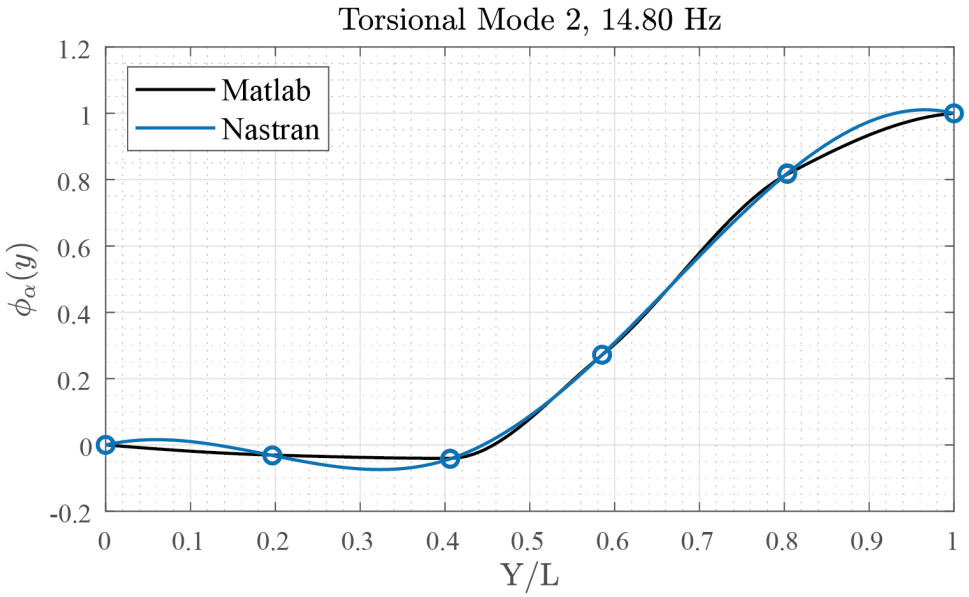

Figure 5.8 Comparison of Second Torsion Mode Shape

Overall, the first two bending and torsion mode shapes show strong agreement with the Nastran solution while the error in the higher frequency modes, namely the third bending mode, introduces higher error as there are only five discretizations in the model. In addition, there are small differences in the mode shapes due to differences in the flexibility influence coefficients used in the calculations and numerical differences in the modal extraction techniques.

5.1.2 Flutter

Next, the open-loop flutter characteristics of the systems are simulated by perturbing them with a gust and evaluating the responses. The generalized response of each model is tracked while the damping and prevailing frequency are estimated. Figure 5.9 shows the V-F and V-g plots of the Nastran pk flutter solution for the full range of airspeed in the Nastran input card. These plots show the frequency F and damping g of each mode as a function of airspeed. The system becomes unstable at the airspeed which a mode crosses into positive damping.

Figure 5.10 shows a zoomed view of the V-F and V-g plot of the Nastran pk flutter solution, making the flutter speed more evident. When examining the V-F plot, each line

corresponds to a mode in Table 5.2 when reading the figure from bottom to top. This means the bottom line (blue) corresponds to the lowest frequency mode, i.e. first bending. The line second from the bottom (orange) corresponds to the second mode, i.e. first torsion. This pattern continues for all modes in Table 5.2. When examining the V-g plot, each line corresponds to the mode of the same color in the V-F plot. For example, the orange line shows the damping of the first torsional mode with respect to airspeed. The Nastran V-g plot shows that the first torsional mode becomes unstable at approximately $1080 ft/s$.

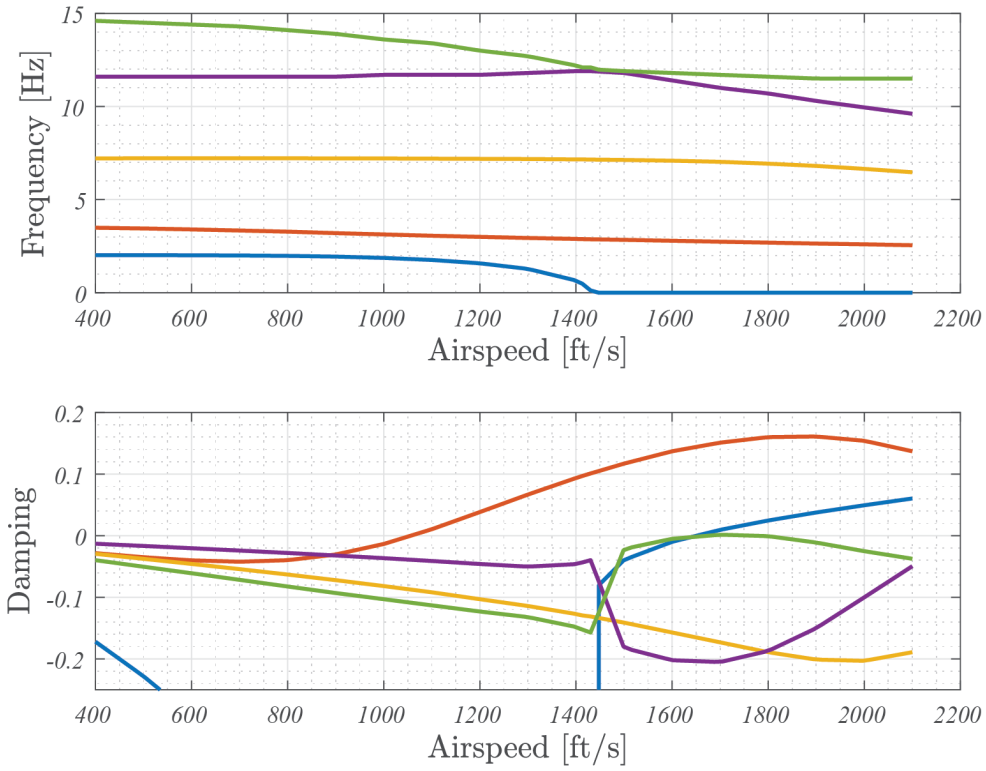

Figure 5.9 Nastran V-F and V-g Plot

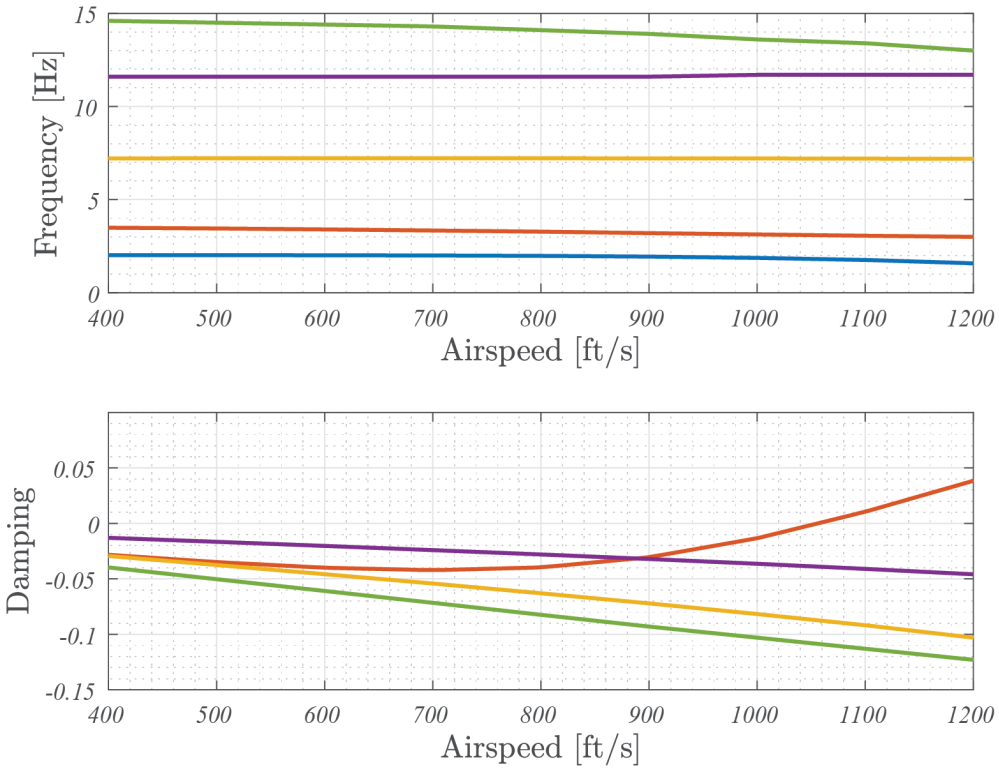

Figure 5.10 Nastran F-F and V-g Plot Zoomed

Figure 5.11 shows the estimated V-F and V-g curves from the Matlab unsteady vortex-lattice solution. The V-g plot shows that the first torsional mode becomes unstable at approximately 1120 ft/s.

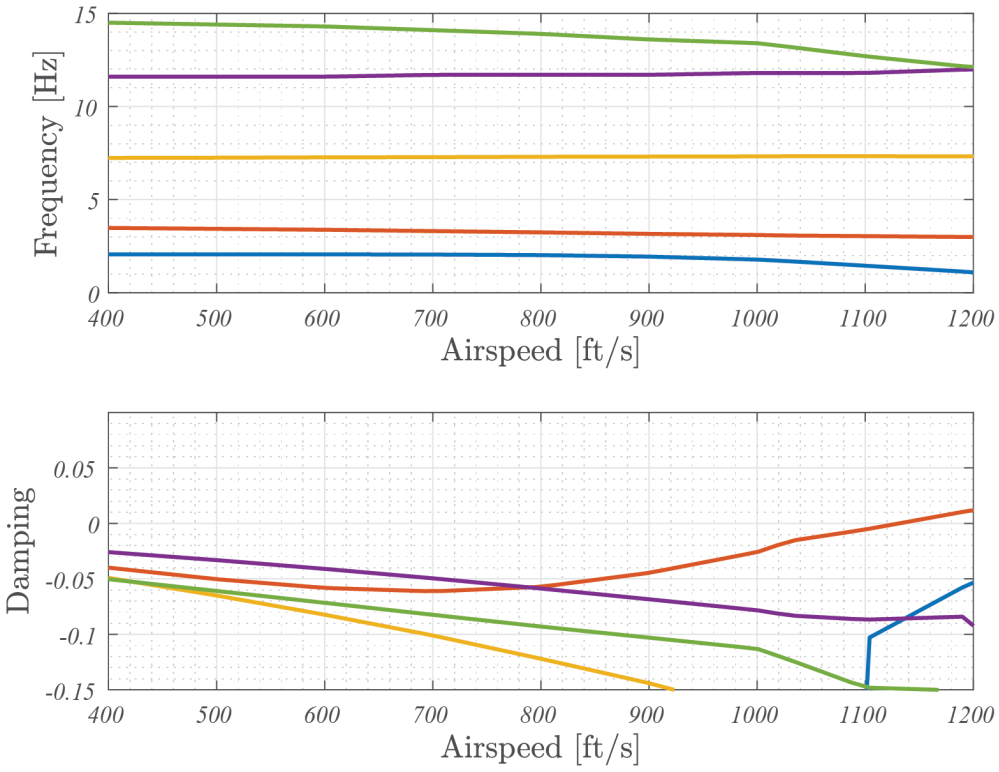

Figure 5.11 Matlab V-F and V-g Plot

These results indicate strong agreement between the Nastran solution and the Matlab solution in both flutter speed prediction and the flutter mode. The flutter speed is predicted with a 3.7% error compared to the Nastran solution and the correct flutter mode (first torsion) is also predicted.

6 Control Systems

Various forms of direct and indirect model reference adaptive control are evaluated on their performance and robustness on the two-dimensional system before applying them to the flexible aircraft. The open-loop reference model is of the form

$$\dot{\bar{x}}_m = A_m \bar{x}_m + B_m \bar{u}_m(t) \qquad \bar{x}_m(0) = x_0$$
$$\bar{y}_m = C_m \bar{x}_m$$

where $\bar{x}_m \in \mathbb{R}^n$ is the reference model state vector, $\bar{u}_m \in \mathbb{R}^q$ is the reference model control input vector, $\bar{y}_m \in \mathbb{R}^p$ is the reference model output vector, $A_m \in \mathbb{R}^{n \times n}$ is the reference model state matrix, $B_m \in \mathbb{R}^{n \times q}$ is the reference model input matrix, and $C_m \in \mathbb{R}^{p \times n}$ is the reference model output matrix. The reference model is a linearized dynamics model at a flutter free point in the flight envelope. Within the reference model framework, two scenarios are considered. In the first scenario, all of the states are available for feedback (i.e. full-state feedback). In the second scenario, only a subset of the states are available for feedback (i.e. partial-state feedback) and output feedback or a state estimator is required.

For the full-state feedback case, a linear quadratic regulator is implemented to form the closed-loop reference model dynamics. In this case, the control law is

$$\bar{u}_m(t) = -K_{LQR}\, \bar{x}_m(t) \tag{6.1}$$

where $\bar{u}_m(t) \in \mathbb{R}^q$ is the control input, $K_{LQR} \in \mathbb{R}^{q \times n}$ is a vector of LQR gains, and $\bar{x}_m(t) \in \mathbb{R}^n$ is the reference model state vector. The closed-loop reference model dynamic matrix is

$$A_{m_{cl}} = (A_m - B_m K_{LQR}) \tag{6.2}$$

where $A_{m_{cl}} \in \mathbb{R}^{n \times n}$ is the closed-loop state matrix. For the partial-state feedback case, a linear quadratic regulator with output feedback is implemented to form a closed-loop

reference model. In this case, the control law is

$$\bar{u}_m(t) = -K_{LQR}\,\bar{y}_m(t) \tag{6.3}$$

where $K_{LQR} \in \mathbb{R}^{p\times n}$ is a vector of LQR gains and $\bar{y}_m \in \mathbb{R}^p$ is the reference model output vector. In this case, the closed-loop reference model dynamics matrix is

$$A_{m_{cl}} = (A_m - B_m K_{LQR} C_m) \tag{6.4}$$

In both cases, the LQR gain is determined by solving the Matrix Ricatti Equation for an infinite horizon LQR controller as discussed later in this chapter. This allows the system to track a reference model that drives the angle of attack to a desired set point and provides the ability to control the frequency of both the pitch and plunge acceleration. The control input for the closed loop LQR system is determined by minimizing the cost function

$$J = \tfrac{1}{2}[C\bar{x}(T)]^\top W[C\bar{x}(T)] + \tfrac{1}{2}\int_0^T [\bar{x}^\top(t)Q\bar{x}(t) + \bar{u}^\top R\bar{u}(t)]dt \tag{6.5}$$

where $Q \in \mathbb{R}^{n\times n}$ is a positive semi-definite state tuning matrix and $R \in \mathbb{R}^{q\times q}$ is a positive definite control input tuning matrix.

6.1 Full-State Feedback Direct Model Reference Adaptive Control

Direct model reference adaptive control laws take the following general form [23], with numerous variations in the literature:

$$\bar{u}(t) = -K_y(t)\bar{y}(t) - K_u(t)\bar{u}_m(t) \tag{6.6}$$

where $K_y(t) \in \mathbb{R}^{n\times p}$ and $K_u(t) \in \mathbb{R}^{n\times q}$ are adaptive gains. This form of adaptive controller has been applied to nonlinear, time-varying systems, but classical theoretical results, such as Lyapunov-based stability proofs, are well established for linear, time-invariant (LTI) systems

of the form:

$$\dot{\bar{x}}(t) = A\bar{x}(t) + B\Lambda\bar{u}(t)$$
$$\bar{y}(t) = C\bar{x}(t)$$

where it is assumed that A is the unknown state matrix, B is the known input matrix, and $\Lambda \in \mathbb{R}^{m\times m}$ represents a positive definite matrix of unknown control effectiveness. The development that follows from Nguyen [23] assumes that the $\bar{y} = \bar{x}$, such that there is a direct sensor measurement of each state (i.e., full state feedback), but the results generalize to the partial state feedback case. Under certain conditions, when applied to LTI systems, there exist model matching conditions such that

$$K_y^* = (B\Lambda)^{-1}(A - A_{m_{CL}}) \tag{6.7}$$

$$K_u^* = (B\Lambda)^{-1} B_m \tag{6.8}$$

where K_y^* and K_u^* represent ideal constant values of $K_y(t)$ and $K_u(t)$ that would cause the system to exactly track the reference, or in other words match the closed-loop dynamics to the reference model, assuming A and B are known. In practice, A and B are not completely known, but the stability proof merely requires the existence of solutions to the matching conditions, not the actual ideal gains themselves. If the number of system inputs and states are not the same, $(B\Lambda)^{-1}$ in the matching conditions would take the form of a pseudoinverse. For the full state feedback case, $\bar{y}_m = \bar{x}_m$ and $\bar{y} = \bar{x}$, errors can be defined as

$$\bar{e}(t) = \bar{x}_m(t) - \bar{x}(t) \tag{6.9}$$

$$\Delta K_y(t) = K_y(t) - K_y^* \tag{6.10}$$

$$\Delta K_u(t) = K_u(t) - K_u^* \tag{6.11}$$

where $\bar{e}(t)$ is the tracking error and $\Delta K_y(t)$ and $\Delta K_u(t)$ represent the difference between the adaptive gains and their ideal values. Then, the error dynamics are defined by

$$\dot{\bar{e}}(t) = \dot{\bar{x}}_m(t) - \dot{\bar{x}}(t) = A_{m_{cL}}\bar{e}(t) + B\Lambda\Delta K_y(t)\bar{y}(t) + B\Lambda\Delta K_u(t)\bar{u}_m(t) \tag{6.12}$$

A stability proof then follows using the Lyapunov function

$$V = \bar{e}^\top(t)P\bar{e}(t) + tr\left(\Lambda\Delta K_y(t)\Gamma_y^{-1}\Delta K_y^\top(t)\right) + tr\left(\Lambda\Delta K_u(t)\Gamma_u^{-1}\Delta K_u^\top(t)\right) \tag{6.13}$$

where Γ_y and Γ_u are positive definite matrices. The derivative of the Lyapunov function simplifies to

$$\begin{aligned}\dot{V} = -\bar{e}^\top(t)Q\bar{e}(t) + 2tr\left(\Lambda\Delta K_y(t)\left[\Gamma_y^{-1}\Delta\dot{K}_y^\top(t) + \bar{y}(t)\bar{e}^\top(t)PB\right]\right) \\ + 2tr\left(\Lambda\Delta K_u(t)\left[\Gamma_u^{-1}\Delta\dot{K}_u^\top(t) + \bar{u}_m(t)\bar{e}^\top(t)PB\right]\right)\end{aligned} \tag{6.14}$$

from which the update laws can be derived. The update laws for the adaptive gains are then chosen as

$$\dot{K}_y(t) = -B^\top P\bar{e}(t)\bar{x}^\top(t)\Gamma_y \qquad K_y(0) = K_{y,0} \tag{6.15}$$

$$\dot{K}_u(t) = -B^\top P\bar{e}(t)\bar{u}_m^\top(t)\Gamma_u \qquad K_u(0) = K_{u,0} \tag{6.16}$$

where $\Gamma_y \in \mathbb{R}^{n\times n}$ and $\Gamma_u \in \mathbb{R}^{q\times q}$ represent positive definites tuning matrices that control the adaptation rates for each adaptive gain and $P \in \mathbb{R}^{n\times n}$ results from the solution to the Lyapunov equation

$$PA_{m_{CL}} + A_{m_{CL}}^\top P = -Q \tag{6.17}$$

where $Q \in \mathbb{R}^{n\times n}$ is any positive definite matrix. With this choice of update laws for the adaptive gains, it follows that

$$\dot{V} = -\bar{e}^\top Q\bar{e} \leq 0 \tag{6.18}$$

This result proves that the tracking error and adaptive gains will be stable (bounded). From Barbalat's Lemma, it can further be concluded that the tracking error will converge to zero.

6.2 Uncertainties or Unmodeled Dynamics

In the case a matched uncertainty exists in the system, the dynamics are given by

$$\dot{\bar{x}}(t) = A\bar{x}(t) + B\left[\bar{u}(t) + \Theta^{\top}(t)\Phi(x)\right] \tag{6.19}$$

where $\Theta(t) \in \mathbb{R}^r$ is a vector of unknown constants and $\Phi(x) \in \mathbb{R}^r$ is a vector of known, bounded basis functions [23]. In this case, the control law becomes

$$\bar{u}(t) = -K_y(t)\bar{y}(t) - K_u(t)\bar{u}_m(t) - \hat{\Theta}^{\top}(t)\Phi(x) \tag{6.20}$$

we can define the estimation error as $\Delta\Theta(t) = \hat{\Theta}(t) - \Theta^*(t)$. The new closed-loop tracking error is

$$\dot{\bar{e}}(t) = \dot{\bar{x}}_m(t) - \dot{\bar{x}}(t) = A_{m_{cL}}\bar{e}(t) + B\Lambda\Delta K_y(t)\bar{y}(t) + B\Lambda\Delta K_u(t)\bar{u}_m(t) + B\Delta\Theta^{\top}\Phi(x) \tag{6.21}$$

A stability proof then follows using the Lyapunov function

$$\begin{aligned} V = \bar{e}^{\top}(t)P\bar{e}(t) + tr\left(\Lambda\Delta K_y(t)\Gamma_y^{-1}\Delta K_y^{\top}(t)\right) \\ + tr\left(\Lambda\Delta K_u(t)\Gamma_u^{-1}\Delta K_u^{\top}(t)\right) + tr\left(\Lambda\Delta\Theta^{\top}\Gamma_{\Theta}^{-1}\Delta\Theta\right) \end{aligned} \tag{6.22}$$

where $\Gamma_\theta \in \mathbb{R}^{r\times r}$ is a positive definite tuning matrix. The derivative of the Lyapunov function simplifies to

$$\begin{aligned}\dot{V} = -\bar{e}^\top Q\bar{e} + 2tr\left(\Lambda\Delta K_y(t)\left[\Gamma_y^{-1}\Delta\dot{K}_y^\top(t) + \bar{y}(t)\bar{e}^\top(t)PB\right]\right) \\ + 2tr\left(\Lambda\Delta K_u(t)\left[\Gamma_u^{-1}\Delta\dot{K}_u^\top(t) + \bar{u}_m(t)\bar{e}^\top(t)PB\right]\right) \\ + 2tr\left(\Lambda\Delta\Theta(t)\left[\Gamma_\Theta^{-1}\Delta\dot{\Theta}(t) + \Phi(x)\bar{e}^\top(t)PB\right]\right) \quad (6.23)\end{aligned}$$

where the update for the uncertain dynamics can be derived as

$$\dot{\hat{\Theta}}(t) = -\Gamma_\Theta\Phi(x)e^\top(t)P\,B \qquad\qquad \hat{\Theta}(0) = \hat{\Theta}_0 \quad (6.24)$$

6.3 Actuator Dynamics

Another consideration to improve the controller performance is including actuator dynamics in the reference model. This allows the reference model to have knowledge of the system limitations and therefore will not command excessive control deflections. Using the system described by Eq. (3.39) as an example, with first-order actuator dynamics, the reference model state matrix A_m becomes

$$A_m = \begin{bmatrix} [0]_{3\times3} & [I]_{3\times3} & [0]_{3\times1} \\ -[M_{sa}]^{-1}[K_{sa}] & -[M_{sa}]^{-1}[C_{sa}] & [M_{sa}]^{-1}[F_\delta] \\ [0]_{1\times3} & [0]_{1\times3} & -a_{srv} \end{bmatrix} \quad (6.25)$$

and the reference model input matrix B_m becomes

$$B_m = \begin{bmatrix} [0]_{3\times1} \\ [0]_{3\times1} \\ a_{srv} \end{bmatrix} \quad (6.26)$$

where a_{srv} is the actuator bandwidth. The state vector becomes

$$\bar{x} = \begin{Bmatrix} \bar{x}_e \\ \dot{\bar{x}}_e \\ \delta_{srv} \end{Bmatrix} \tag{6.27}$$

where $\bar{x}_e$ are the elastic states, $\dot{\bar{x}}_e$ are the elastic rates, and δ_{srv} is the servo position. The control input is

$$\bar{u}_m = \delta_{cmd} \tag{6.28}$$

where δ_{cmd} is the commanded flap deflection. When considering second-order actuator dynamics, the equations of motion of the actuator are given by Eq. (3.205). In this case, the reference model state matrix A_m becomes

$$A_m = \begin{bmatrix} [0]_{3\times3} & [I]_{3\times3} & [0]_{3\times1} & [0]_{3\times1} \\ -[M_{sa}]^{-1}[K_{sa}] & -[M_{sa}]^{-1}[C_{sa}] & [M_{sa}]^{-1}[F_\delta] & [M_{sa}]^{-1}[F_{\dot{\delta}}] \\ [0]_{1\times3} & [0]_{1\times3} & [0]_{1\times1} & 1 \\ [0]_{1\times3} & [0]_{1\times3} & -\frac{k_\delta}{I_\delta} & -\frac{c_\delta}{I_\delta} \end{bmatrix} \tag{6.29}$$

where $[F_{\dot{\delta}}]$ is a vector of forces due to the rate of control surface rotation. This addition is unique to the system with second-order actuator dynamics. The reference model input matrix becomes

$$B_m = \begin{bmatrix} [0]_{3\times1} \\ [0]_{3\times1} \\ [0]_{1\times1} \\ \frac{k_\delta}{I_\delta} \end{bmatrix} \tag{6.30}$$

the state vector is

$$\bar{x} = \begin{Bmatrix} \bar{x}_e \\ \dot{\bar{x}}_e \\ \delta_{srv} \\ \dot{\delta}_{srv} \end{Bmatrix} \tag{6.31}$$

and the control input is

$$\bar{u}_m = \delta_{cmd} \tag{6.32}$$

7 Simulations

This chapter presents open-loop and closed-loop simulation results for a two-dimensional typical section, a three-dimensional cantilevered elastic wing, and a longitudinal-only rigid aircraft with an elastic wing.

7.1 Two-Dimensional System

This section presents simulation results for the pitch-plunge-flap typical section. Table 7.1 provides the structural data used in all linear simulations.

Table 7.1 Airfoil Structural Data

Parameter	Value	Parameter	Value
a	-0.6	k_h	2844.8 N/m
b	0.135 m	k_α	2.82 N/rad
x_α	$[0.0873 - (b + ab)]/b$	k_β	$20.0 N/rad$
m	12.387 kg	c_h	$27.43 N/(m \cdot s)$
I_α	$0.065 kg \cdot m^2$	c_α	$0.036 N \cdot s$
I_β	$0.01 kg \cdot m^2$	c_β	$0.100 N \cdot s$

For the simulations with nonlinear torsional stiffness, the stiffness polynomial is defined by Eq. (3.202) and the coefficients are

Table 7.2 Torsional Stiffness Polynomial Coefficients

Coefficient	Value
k_{α_0}	2.82
k_{α_1}	-62.32
k_{α_2}	3709.70
k_{α_3}	-24196.56
k_{α_4}	48757.69

Table 7.3 provides the aerodynamic coefficients required for quasi-steady aerodynamics.

Table 7.3 Airfoil Aerodynamic Data

Coefficient	Value	Coefficient	Value
C_{l_α}	6.28 /rad	C_{m_β}	-0.635
C_{l_β}	3.358 /rad	C_{h_α}	-0.0481
C_{m_α}	$(0.5+a)C_{l_\alpha}$	C_{l_β}	-0.01552

The remainder of this section compares the performance of a poorly tuned LQR controller to that of an MRAC. The three cases considered are: a linear k_α; a nonlinear k_α; and a system with linear k_α and freeplay, with limits of $\pm 1^\circ$. The LQR controller is tuned on the system with linear k_α operating at an airspeed of $6\,m/s$ to provide additional damping. The MRAC uses the LQR gain as its initial gain prior to any adaptation. The tuning matrices $[Q]$ and $[R]$ are diagonal and defined as follows

$$[Q] = \begin{bmatrix} Q_1 & \cdots & 0 \\ \vdots & \ddots & \vdots \\ 0 & \cdots & Q_n \end{bmatrix} \qquad [R] = \begin{bmatrix} R_1 & \cdots & 0 \\ \vdots & \ddots & \vdots \\ 0 & \cdots & R_q \end{bmatrix}$$

The LQR is tuned with the $[Q]$ and $[R]$ matrices given in Tables 7.4 and 7.5.

Table 7.4 Two-Dimensional $[Q]$ Tuning Values

Tuning Parameter	Value
Q_1	7.500
Q_2	3.000
Q_3	0.050
Q_4	1.000
Q_5	0.005
Q_6	0.050

Table 7.5 Two-Dimensional $[R]$ Tuning Values

Tuning Parameter	Value
R_1	20

Furthermore, the baseline adaptation rates and initial gains are

$$[\Gamma_y]_0 = \begin{bmatrix} \Gamma_1 & \cdots & 0 \\ \vdots & \ddots & \vdots \\ 0 & \cdots & \Gamma_n \end{bmatrix} \qquad [K_{x_0}] = \begin{bmatrix} K_{x_1} & \cdots & K_{x_N} \end{bmatrix}$$

The MRAC is tuned with the adaptation rates given in Table 7.6

Table 7.6 Two-Dimensional $[\Gamma_y]_0$ Tuning Values

Adaptation Rate	Value
Γ_1	5.00
Γ_2	1.00
Γ_3	0.10
Γ_4	2.00
Γ_5	0.35
Γ_6	0.10

and the initial gains given in Table 7.7

Table 7.7 Two-Dimensional $[K_{x_0}]$ Gains

Initial Gain	Value
K_{x_1}	-1.728
K_{x_2}	0.053
K_{x_3}	0.021
K_{x_4}	-0.960
K_{x_5}	-0.084
K_{x_6}	0.003

First, a flutter study of the open-loop system is conducted to determine the unstable airspeed. Figure 7.1 shows the V-g and V-F curves for the system with linear k_α and no actuator freeplay.

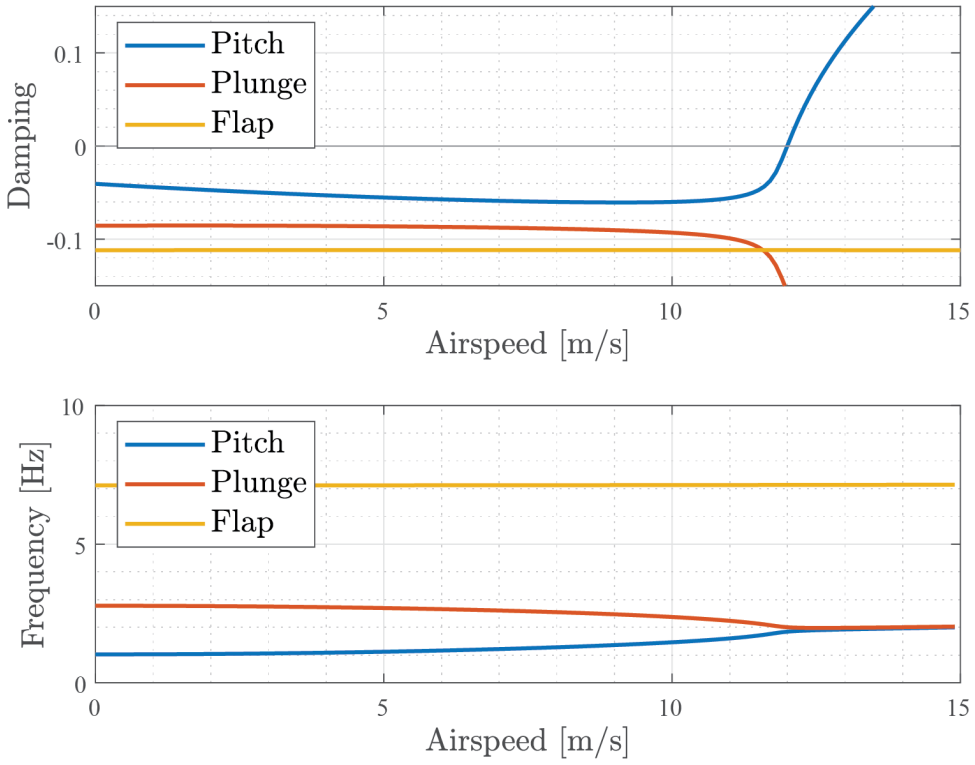

Figure 7.1 Airfoil V-g and V-f Curves

By examination of Figure 7.1, the flutter speed is approximately $12m/s$ at which the pitch mode becomes unstable. All further simulations in this analysis are performed at an airspeed speed of $12m/s$ or $39.4\,ft/s$ to study the effectiveness of a controller on stabilizing the system and providing a desirable response.

Next, the open-loop and closed-loop responses of the system with linear k_α, nonlinear k_α, and linear k_α with actuator freeplay are simulated at the flutter point mentioned above. Figure 7.2 shows the open-loop response of the system with linear k_α.

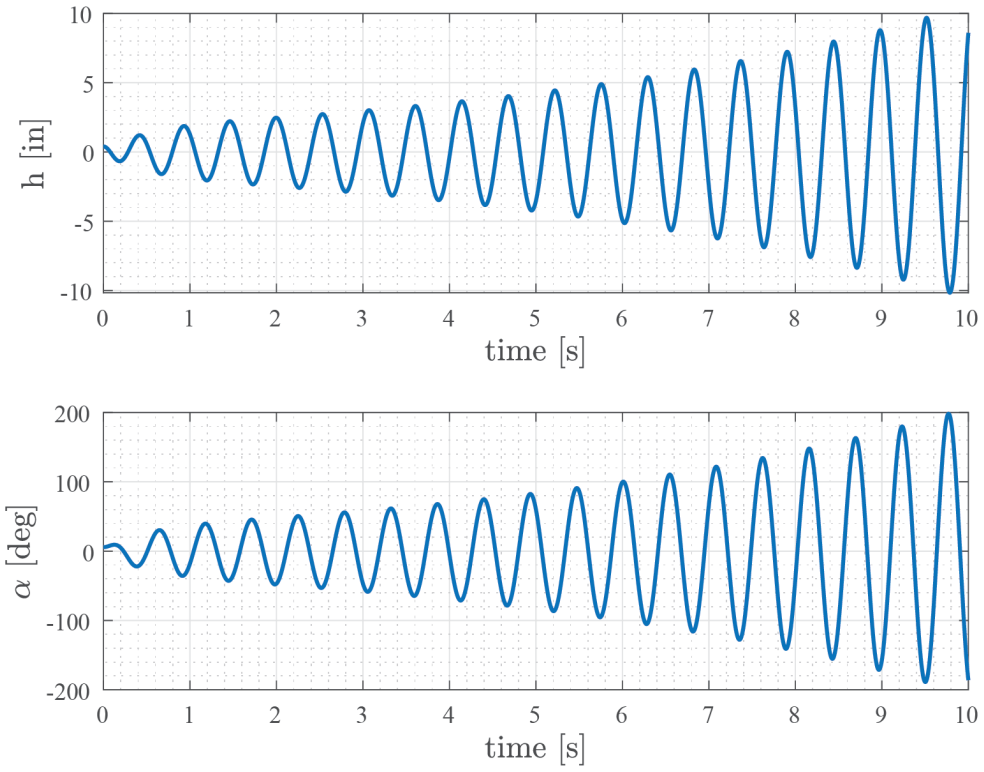

Figure 7.2 Open-Loop Response with Linear k_α at U=39.4 ft/s

The open-loop eigenvalues of the system with a linear k_α are provided in Table 7.8. The frequencies of the pitch and plunge modes approach one another as the system goes unstable, as shown by the positive real part of the pitch eigenvalue.

Table 7.8 Open-Loop Eigenvalues of Airfoil with Linear k_α at $U = 39.4\, ft/s$

Mode	Pole	ζ	ω [rad/s]	ω [Hz]
Flap	-5.01 ± 44.5i	1.12×10^{-1}	44.8	7.13
Plunge	-1.97 ± 12.4i	1.57×10^{-1}	12.6	2.01
Pitch	4.48×10^{-3} ± 11.6i	-3.87×10^{-4} $\times10^{-3}$	11.6	1.84

Next, the closed-loop response with an LQR and MRAC is studied. Figure 7.3 shows the response with each controller active. This shows that both controllers are able to stabilize the system. However, the MRAC is more effective at damping the transience and causes the system to settle faster. Recall, for the typical section, a positive plunge is downward and

a positive pitch is airfoil nose up. Due to the fact that the center of gravity far aft of the elastic axis (approximately $0.7b$) for this simulation study, as the airfoil accelerates upward, it also pitches nose up. This is shown in the first 0.25 seconds of the time history shown in Figure 7.3.

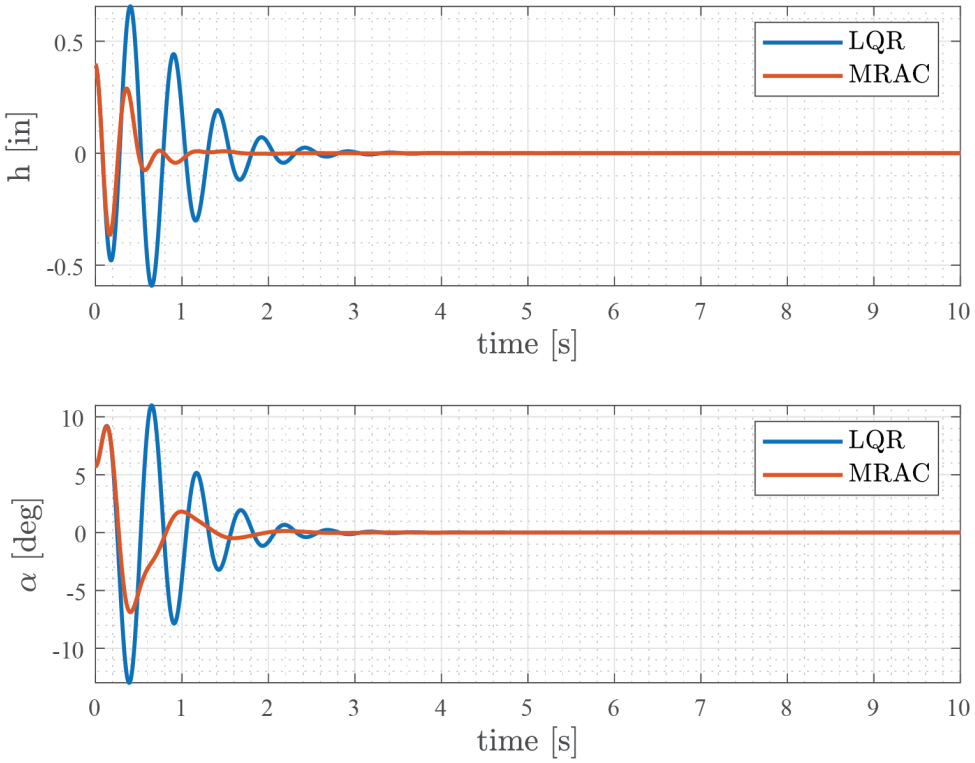

Figure 7.3 Closed-Loop Response with Linear k_α at $U = 39.4\, ft/s$

In addition to the pitch and plunge responses, the control deflection and elastic flap deflection are analyzed. Figure 7.4 shows the actual control surface deflection and the elastic flap deflection. The MRAC provides a more aggressive input than the LQR, which mitigates the response of the system and in turn leads to less overall elastic flap deflection. As the airfoil accelerates upward, the control system commands the flap to deflect trailing edge up (negative δ_{act}) to provide a downward force to counteract the motion.

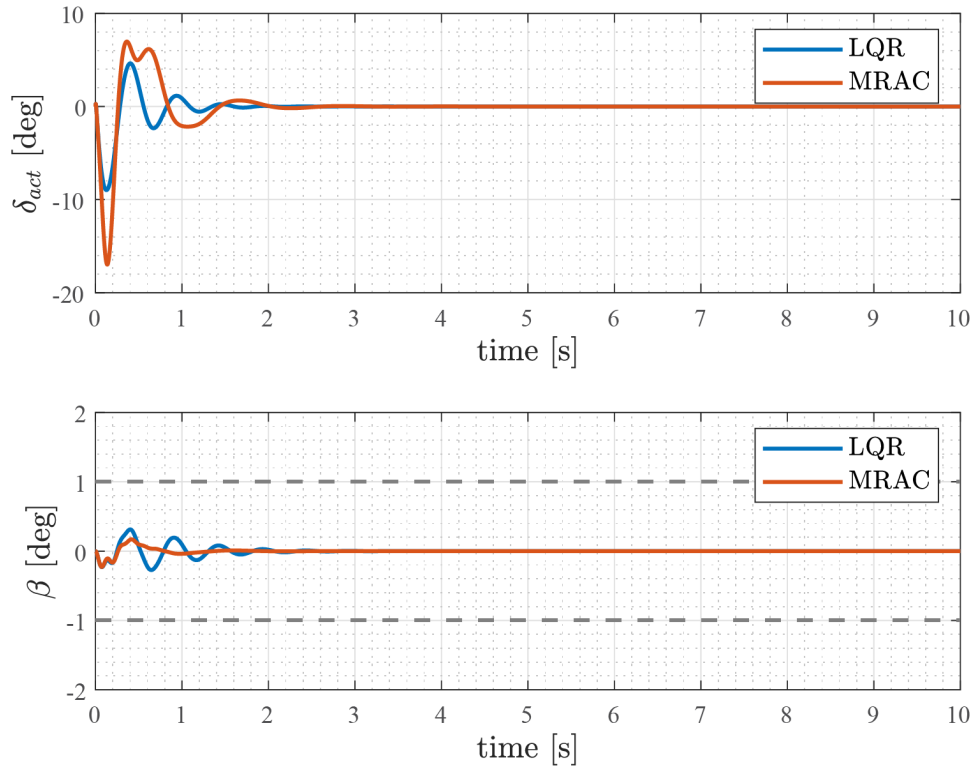

Figure 7.4 Control Input and Flap Deflection with Linear k_α at $U = 39.4\, ft/s$

Figure 7.5 shows the control surface rate for each controller. The MRAC gives an initial spike in the positive direction as it commands a very small positive deflection. Then, the flap reaches its minimum deflection reate at $-180\, deg/s$ and reversing direction to reach a maximum rate of approximately $180\, deg/s$. This shows that the MRAC requires a much faster control surface rate than the LQR.

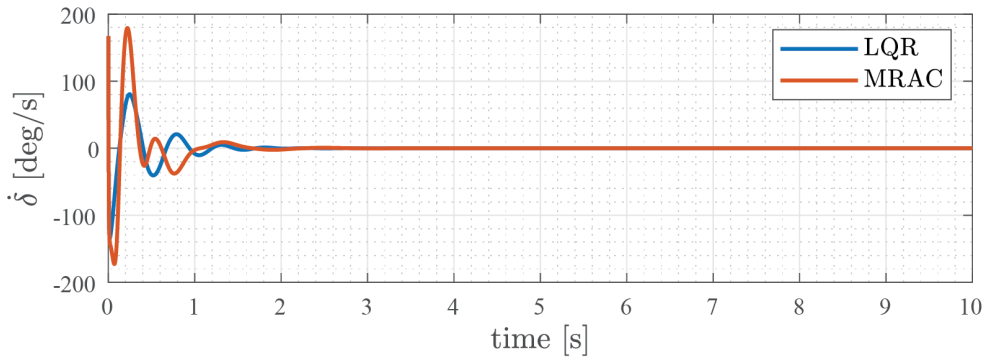

Figure 7.5 Control Surface Rate Linear k_α at $U = 39.4\, ft/s$

Table 7.9 lists the 5% settling times for the pitch and plunge DOFs for the LQR and the MRAC, respectively. This reinforces the assertion that the MRAC is much more effective at attenuating transience; the plunging settling time is reduced by 58% and the pitching settling time is reduced by 51%.

Table 7.9 Settling Time (5% Steady-State) with Linear k_α

	h	α
LQR	2.48 s	2.66 s
MRAC	1.03 s	1.31 s

Figure 7.6 shows the open-loop response of the system with nonlinear k_α. The response is oscillatory but bounded, indicative of limit-cycle oscillation (LCO).

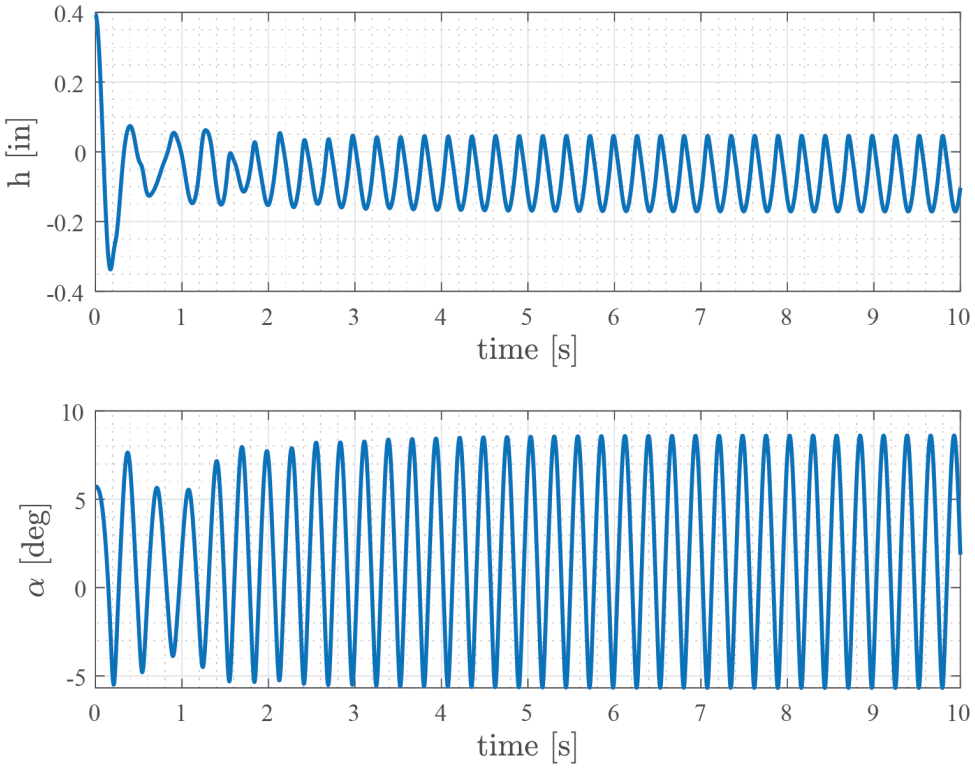

Figure 7.6 Open-Loop Response with Nonlinear k_α at $U = 39.4\, ft/s$

Figure 7.7 shows the closed-loop response of the system to an LQR and MRAC. The poorly tuned LQR is unable to stabilize the system and increases the amplitude of LCO. In

the case of the MRAC, the initial oscillation persists for approximately 2.5 seconds before the MRAC is able to stabilize the system due to adaptation.

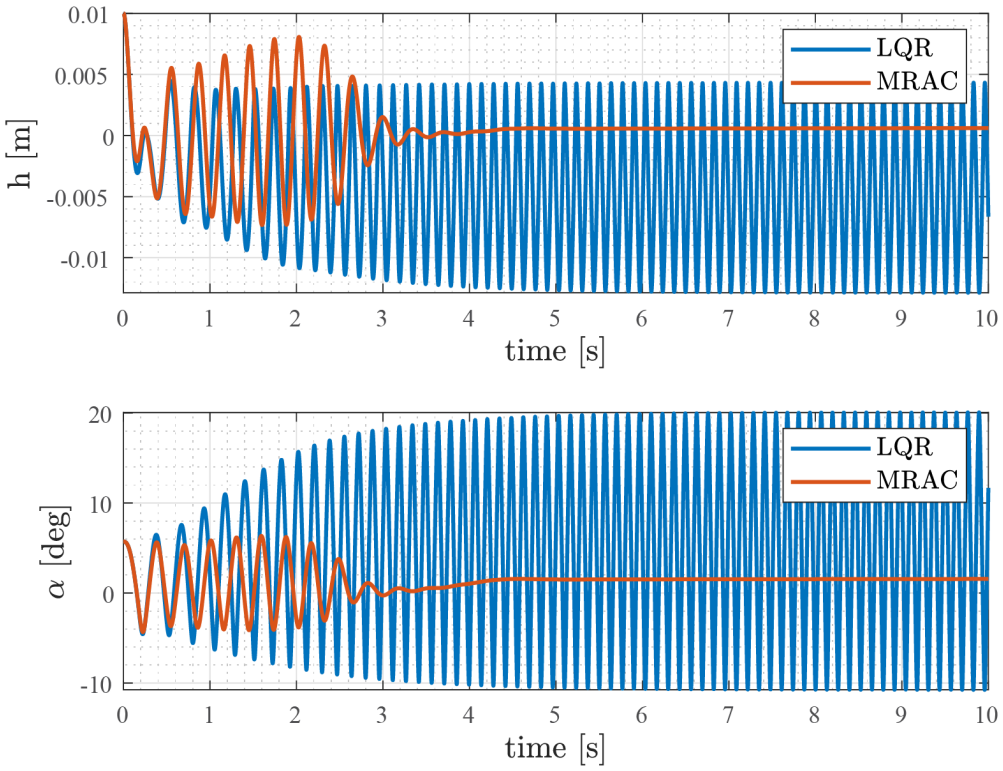

Figure 7.7 Closed-Loop Response with Nonlinear k_α at $U = 39.4\, ft/s$

Figure 7.8 shows the control input and flap deflection angle for the LQR and MRAC. The MRAC requires approximately $\pm 10°$ of control input while adapting before it settles. The LQR saturates and is unable to stabilize the system.

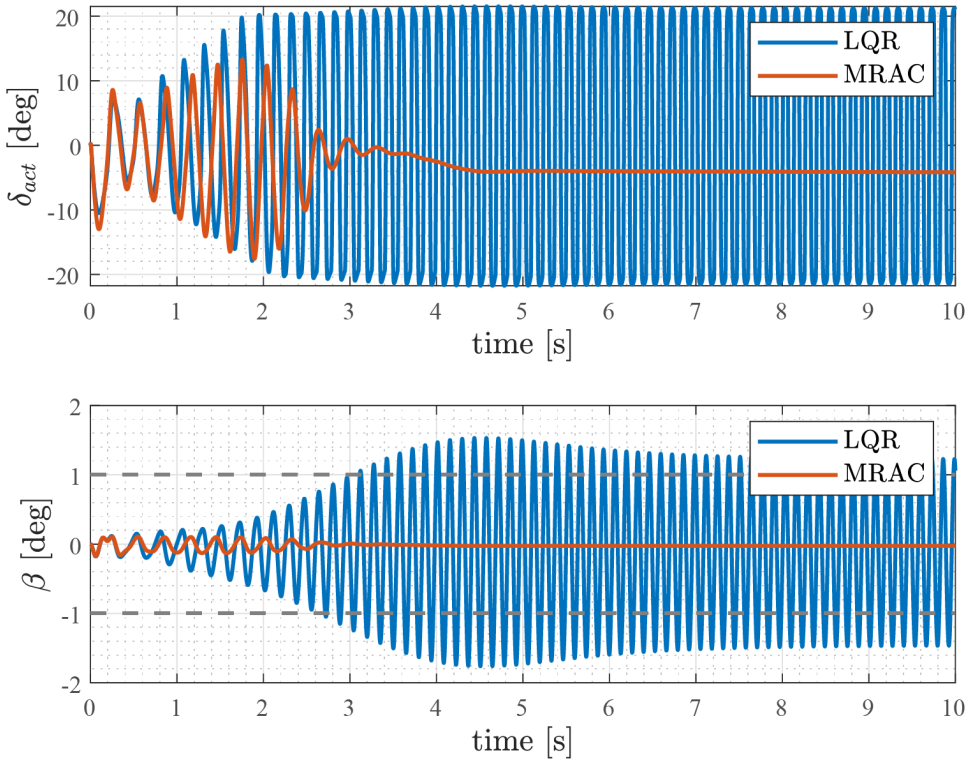

Figure 7.8 Control Input and Flap Deflection with Nonlinear k_α at $U = 39.4\, ft/s$

Figure 7.9 shows the control surface rate for the MRAC. The LQR is excluded as it does not stabilize the system. This shows, at its peak, the controller is commanding approximately $\pm 300\, deg/s$. For a control surface with limits of $\pm 20°$ this is equivalent to 3.75 Hz.

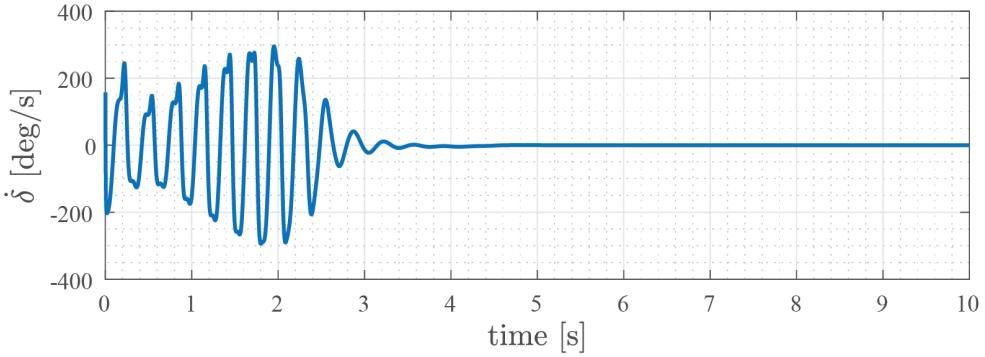

Figure 7.9 Control Surface Rate Nonlinear k_α at $U = 39.4\, ft/s$

Table 7.10 gives the 5% settling times for the LQR and MRAC respectively. The MRAC

settles both pitch and plunge in approximately three seconds, while the LQR does not stabilize the system and therefore settling time cannot be determined.

Table 7.10 Settling Time (5% Steady-State) with Nonlinear k_α

	h	α
LQR	-	-
MRAC	3.60 s	2.67 s

Next, the system response with a linear k_α and actuator freeplay is analyzed. For this case, the simulations are run with freeplay limits of $\pm 1°$ at an airspeed of $39.4\, ft/s$. Figure 7.10 shows the open-loop response with freeplay simulated over a time span of 10 seconds.

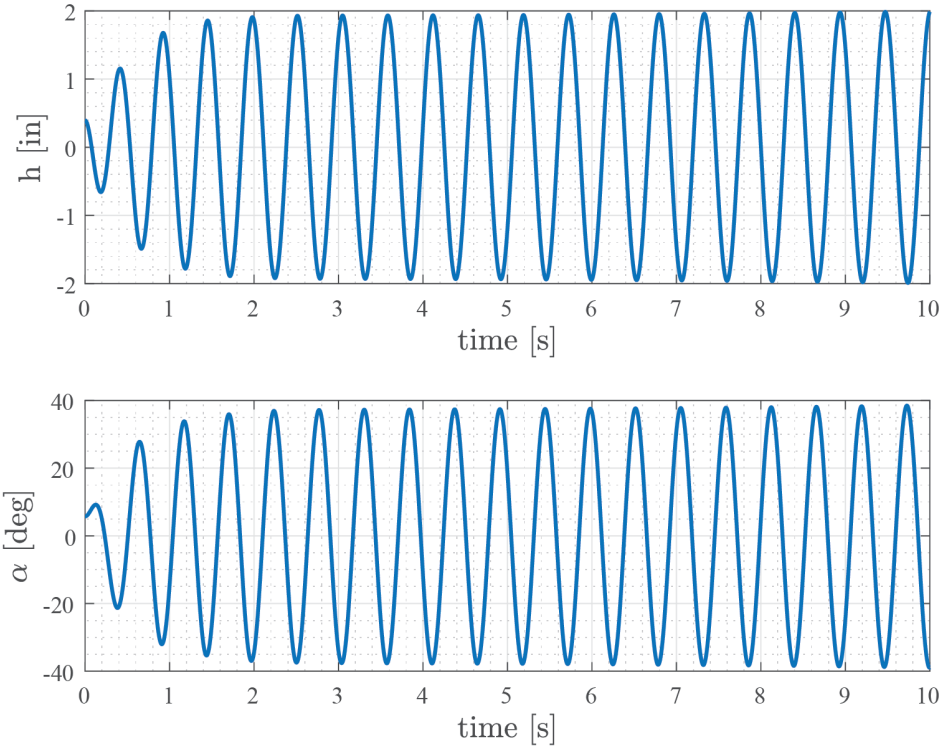

Figure 7.10 Open-Loop Response with Freeplay at $U = 39.4\, ft/s$

Figure 7.11 shows the flap angle and freeplay limits for the open-loop response at $39.4\, ft/s$.

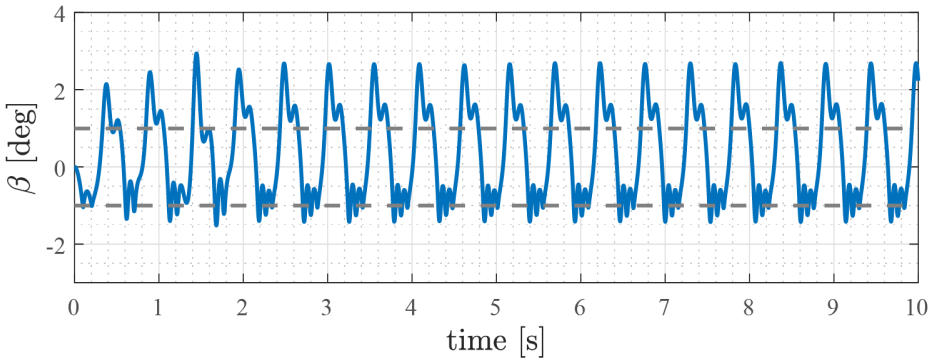

Figure 7.11 Open-Loop Flap Angle with Freeplay at $U = 39.4\,ft/s$

Figure 7.12 shows the closed-loop response of the system with actuator freeplay to an LQR and MRAC. Both controllers are able to stabilize the system; the plunge converges to near zero while the pitch does not settle to the set point due to the additional moment caused by the freeplay.

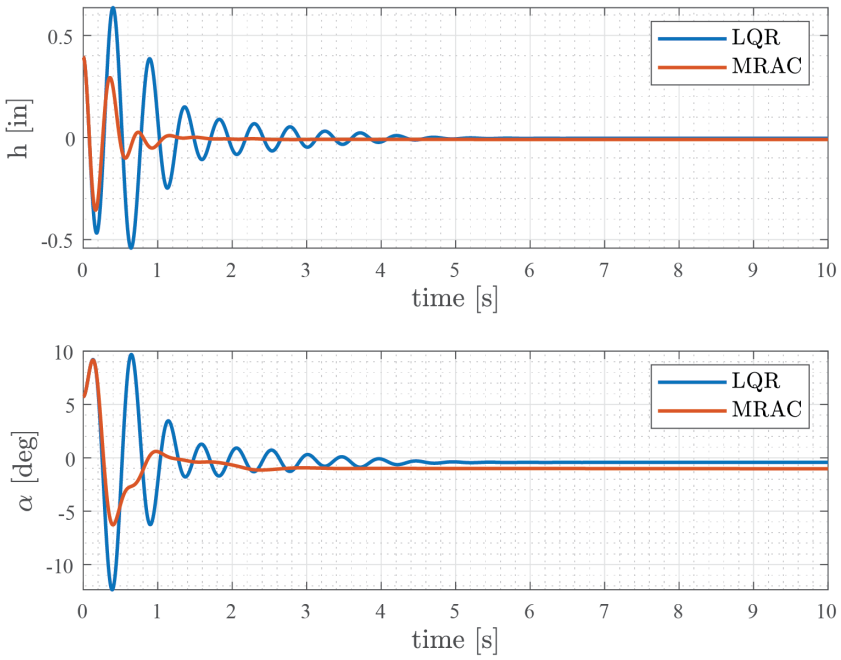

Figure 7.12 Closed-Loop Response with Freeplay at $U = 39.4\,ft/s$

Figure 7.13 shows the actual control surface displacement and flap angle for the LQR and MRAC. Both control inputs exhibit similar behavior, with the MRAC being more aggressive

than the LQR. When analyzing the flap angle, both controllers initially cause the flap to rebound off of the freeplay limits before settling at the limit of $+1°$. Recall, a positive flap deflection is trailing edge downward. Thus, the system settles at an equilibrium point where the airfoil has a small nose down pitch angle causing the flap to sit on the freeplay limit.

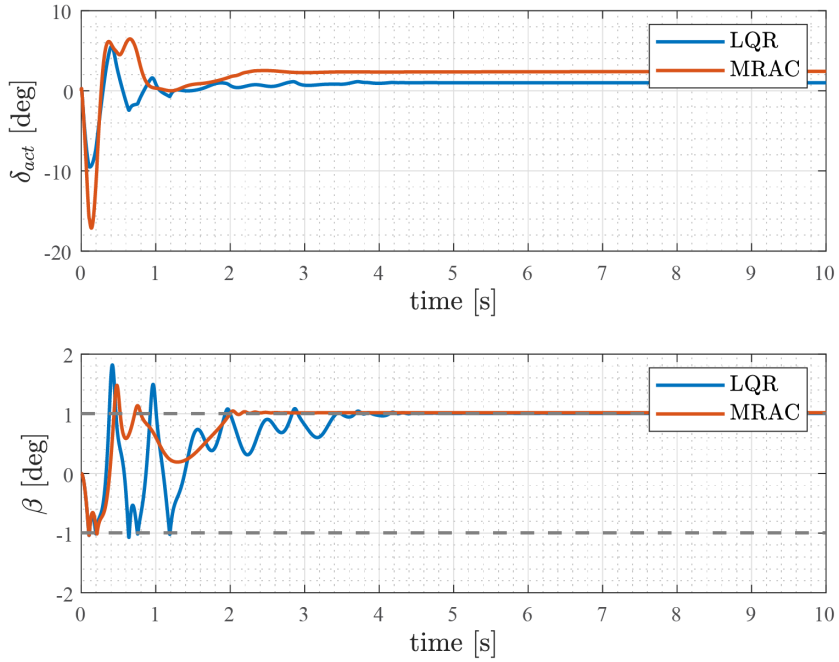

Figure 7.13 Control Input and Flap Deflection with Freeplay $U = 39.4\, ft/s$

Figure 7.14 shows the control surface rate for each controller. Similar to the linear system, the MRAC requires a much faster response than the LQR.

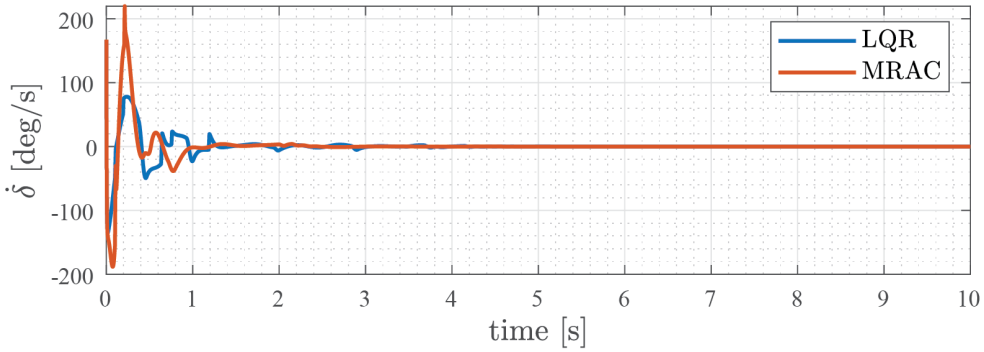

Figure 7.14 Control Surface Rate Nonlinear k_α at $U = 39.4\, ft/s$

Table 7.11 lists the 5% settling times in pitch and plunge for the LQR and the MRAC with actuator freeplay present. This again shows that the MRAC is more effective at attenuating transience than the LQR; the settling time in plunging reduces by 78% and the settling time in pitching reduces by 64%.

Table 7.11 Settling Time (5% Steady-State) with Actuator Freeplay

	h	α
LQR	4.40 s	4.39 s
MRAC	0.99 s	1.58 s

Furthermore, comparing the data in Table 7.11 to the data in Table 7.9 shows that the introduction of freeplay causes the settling times of the LQR to increase by approximately 80% while the settling times of the MRAC are relatively unchanged.

Actuator Bandwidth Study

Another consideration is the effect of actuator bandwidth on the effectiveness of the control system. As the controller is a regulator, the performance is quantified by the RMS error of the system response to an initial condition over a ten second simulation. The controller performance was evaluated for first-order and second-order actuator dynamics using a fast actuator, i.e. a step command, as the baseline. When considering the second-order actuator, the equivalent "bandwidth" is achieved by varying the damping where $a \approx k/c$ for a massless system. Figure 7.15 shows the RMS error vs. bandwidth for closed-loop simulations with a linear k_α at $39.4\, ft/s$ in the absence of freeplay.

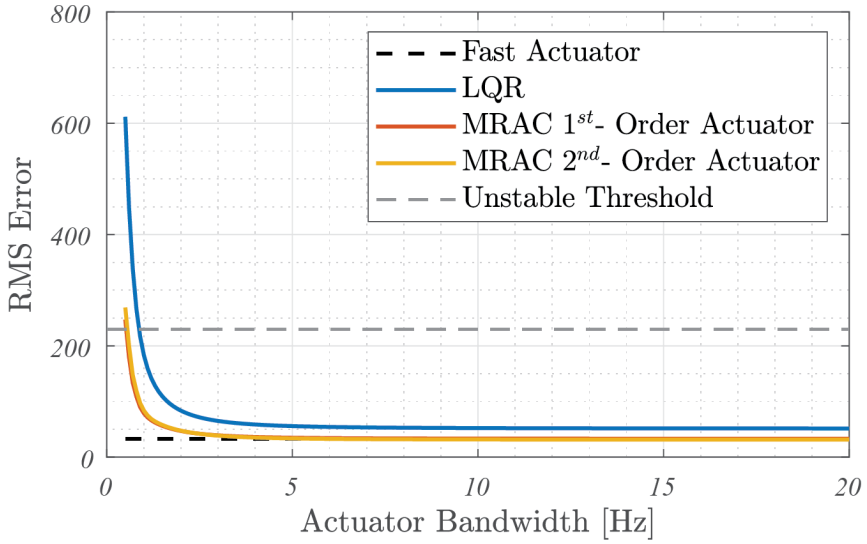

Figure 7.15 RMS Error vs. Actuator Bandwidth for System with Linear k_α at $U = 39.4\, ft/s$

The dashed black line indicates the RMS error when using a fast actuator, i.e. minimum possible error in the response. The dashed grey line is the unstable threshold, where error above this line indicates that the system diverges. This shows that the MRAC responses have less error than that of the LQR for a given bandwidth. Although, the error does not begin to increase for either controller until the bandwidth is reduced below $3Hz$. Over the entire range of actuator bandwidth, the MRAC settles the system faster as indicated by the RMS error, and remains stable for smaller values of actuator bandwidth when compared to the LQR. In addition, there is little difference in the response between an MRAC with a first-order actuator or second-order actuator.

Figure 7.16 shows the closed-loop LQR and MRAC pitch and plunge displacements for a $1\,Hz$ actuator. In this scenario, the MRAC is more effective than the LQR at damping the oscillations.

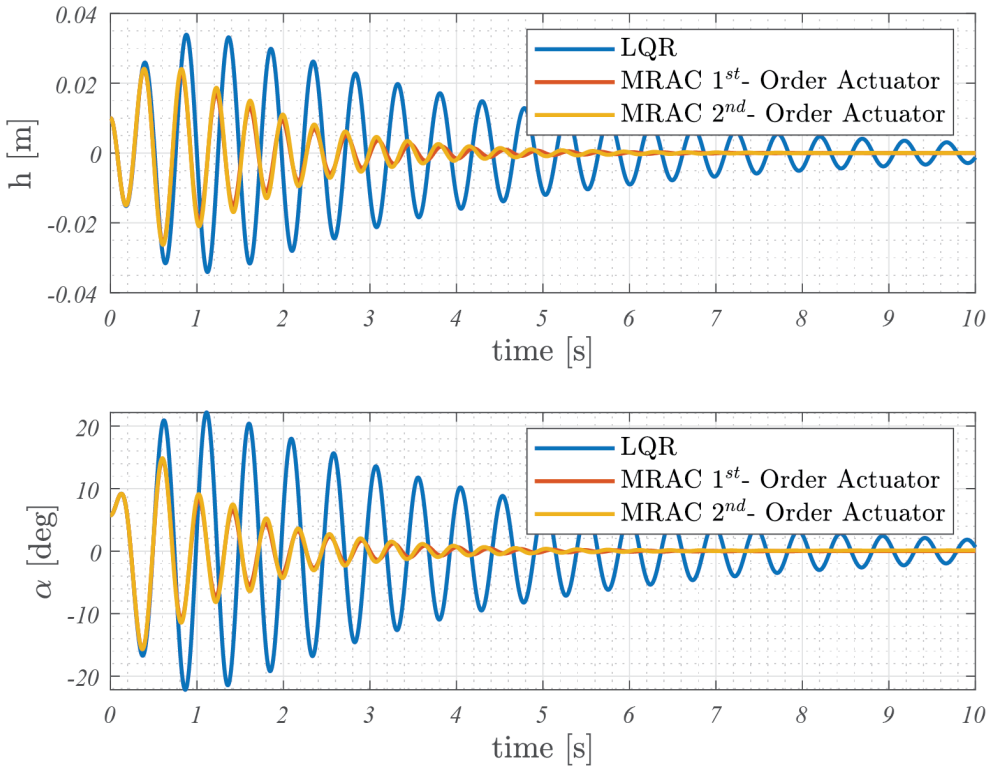

Figure 7.16 Closed-Loop Response with Linear k_α and $a_{srv} = 1Hz$

Figure 7.17 shows the actual control input for an actuator bandwidth of $1Hz$. There are relatively small differences between the amplitudes for the commanded deflection and actual deflection for the second-order actuator, but there is a small phase shift.

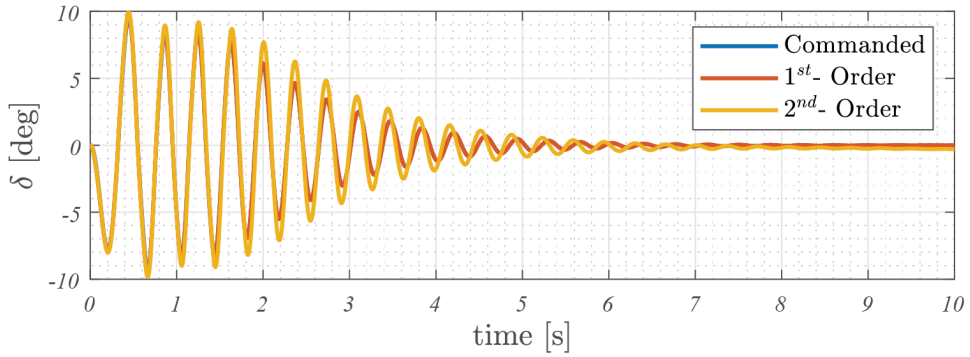

Figure 7.17 MRAC Control Input for Linear k_α and $a_{srv} = 1Hz$

Figure 7.18 shows the closed-loop LQR and MRAC pitch and plunge displacements for

an actuator bandwidth of $10\,Hz$. For higher bandwidths, the differences in the responses to an LQR and MRAC are less extreme, but the MRAC still outperforms the LQR.

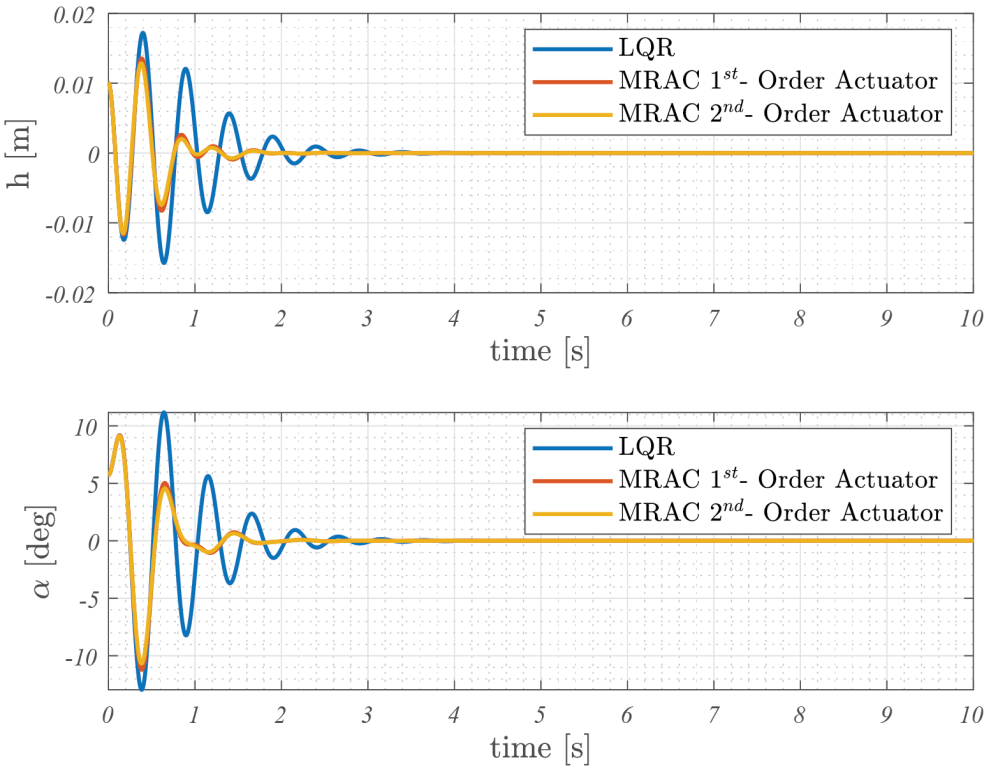

Figure 7.18 Closed-Loop Response with Linear k_α and $a_{srv} = 10Hz$

Figure 7.19 shows the control input for an actuator bandwidth of $10Hz$. For higher bandwidths, there is a negligible difference between the first-order and second-order dynamics.

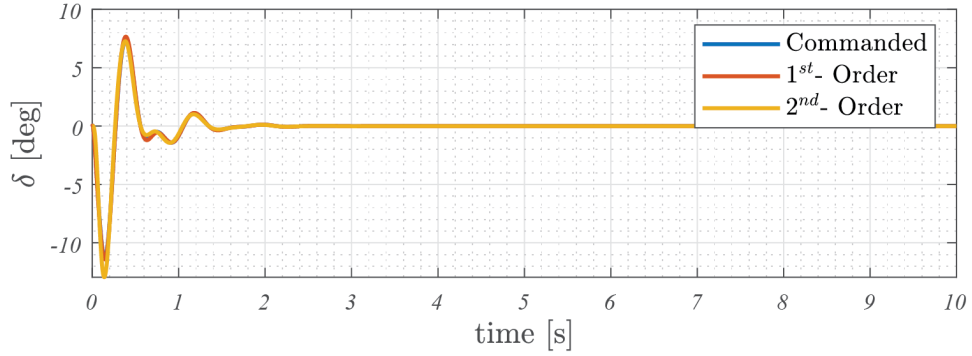

Figure 7.19 Control Input and Flap Deflection with Linear k_α and $a_{srv} = 10Hz$

Next, a system with nonlinear torsional stiffness is studied in the same manner as just decribed. This system differs from the linear system in that the baseline MRAC is unable to stabilize the system. Through experimentation, it was found that increasing the adaptation rates to $[\Gamma_y] = 10[\Gamma_y]_0$ provides a more desirable response. Figure 7.20 shows the RMS error vs. bandwidth for closed-loop simulations with a nonlinear k_α at 39.4 ft/s in the absence of freeplay.

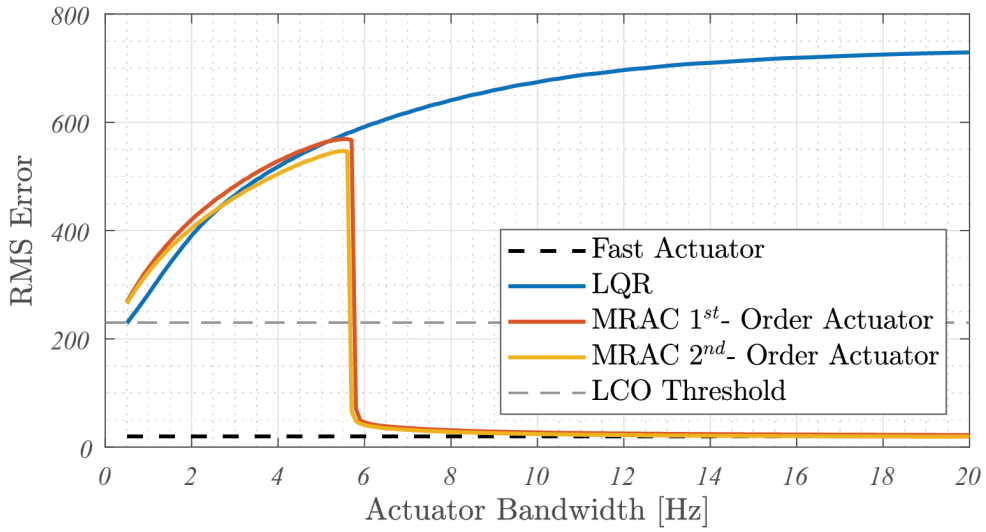

Figure 7.20 RMS Error vs. Actuator Bandwidth for System with Nonlinear k_α at $U = 39.4\, ft/s$

The LQR is unable to stabilize the system for any actuator bandwidth. Conversely, the MRAC with both first-order and second-order actuator dynamics is able to stabilize the system for all bandwidths above $6Hz$. Below $6Hz$, the performance suddenly degrades and is no longer able to stabilize the system. The addition of the nonlinear spring creates a condition where the MRAC is no longer feasible, causing the RMS error to suddenly increase as the system is no longer quadratically stable. Similar to the linear system, there are minimal differences in the performance of the MRAC when comparing first-order and second-order actuator dynamics.

Finally, the system with linear torsional stiffness and freeplay is studied. Figure 7.21 shows the RMS error vs. bandwidth for closed-loop simulations with a linear k_α and freeplay

at $39.4\,ft/s$.

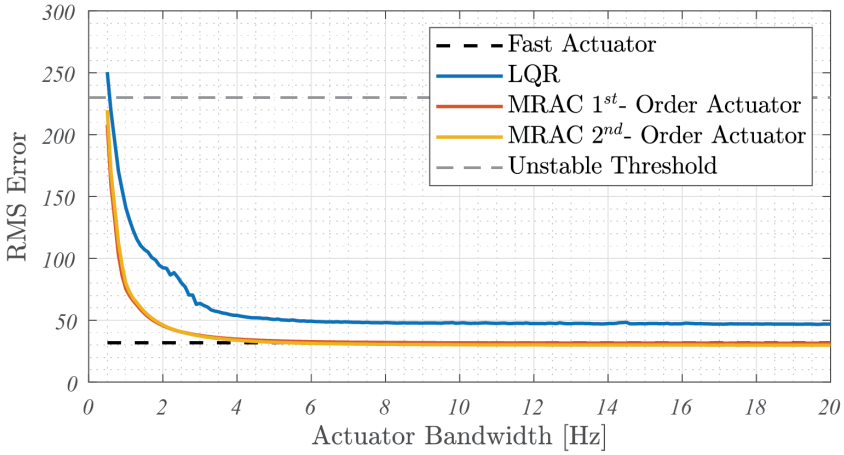

Figure 7.21 RMS Error vs. Actuator Bandwidth for System with Linear k_α and Freeplay at $U = 39.4\,ft/s$

The results in Figure 7.21 show a similar behavior to the system without freeplay as the torsional stiffness is a primary driver of the dynamics. However, the difference in the LQR response is highlighted in the region of lower actuator bandwidth where higher levels of error are introduced below $4Hz$.

Overall, a direct model reference adaptive controller is able to provide a more desirable response than a poorly tuned LQR. In each case, the MRAC drives faster settling times than the LQR and shows robustness when nonlinear torsion and freeplay are introduced. In addition, an actuator bandwidth study shows an MRAC will provide faster settling times than an LQR, particularly with slow actuators.

7.2 Elastic Wing

This section presents results for the open-loop and closed-loop simulations for a cantilevered flexible wing. A representative wing is created to mimic the geometry of a Learjet 24, while the structural characteristics are approximated to provide "aircraft-like" behavior while serving as a test bed for adaptive control. Table 7.12 lists the geometric data used to build the wing aerodynamic panel.

Table 7.12 Wing Geometric Data

Parameter	Symbol	Value
Span	b	$35.6ft$
Root Chord	c_r	$4.0ft$
Tip Chord	c_t	$2.5ft$
Leading Edge Sweep	Λ_{LE}	$10\,^\circ$
Inboard Aileron Break	η_i	$0.7(b/2)$
Outboard Aileron Break	η_o	$0.8(b/2)$
Aileron Chord	c_f	$0.2\,c$

Table 7.13 gives the wing structural data used in the simulations.

Table 7.13 Wing Structural Data

Station (in)	M (lb_f)	EI $(lb_f \cdot in^2)$	GJ $(lb_f \cdot in^2)$	I_α $(lb_f \cdot in^2)$	S_α $(lb_f \cdot in)$
0	316.5	3.570×10^6	2.244	455.7	126.6
20.7	224.6	2.948×10^6	1.866	293.8	85.6
55.0	140.1	2.082×10^6	1.347	165.7	50.8
82.6	102.3	1.557×10^6	1.024	108.8	35.2
110.2	80.1	1.152×10^6	0.770	76.1	26.0
137.7	66.7	0.839×10^6	0.571	56.3	20.4
165.3	55.6	0.603×10^6	0.417	41.4	16.0
192.8	35.6	0.427×10^6	0.302	23.1	9.6
213.5	11.1	0.329×10^6	0.235	6.2	2.8

The first three bending and torsion modes are calculated using the matrix iteration method detailed in Section 3.4. Table 7.14 gives the natural frequencies of the modes retained in the solution.

Table 7.14 Wing Natural Frequencies

Mode No. -	Label -	Natural Freq. (Hz)
1	First Bending	4.03
2	First Torsion	7.74
3	Second Torsion	15.11
4	Second Bending	16.45
5	Third Bending	38.60

Figure 7.22 shows the mode shapes of the first three bending modes.

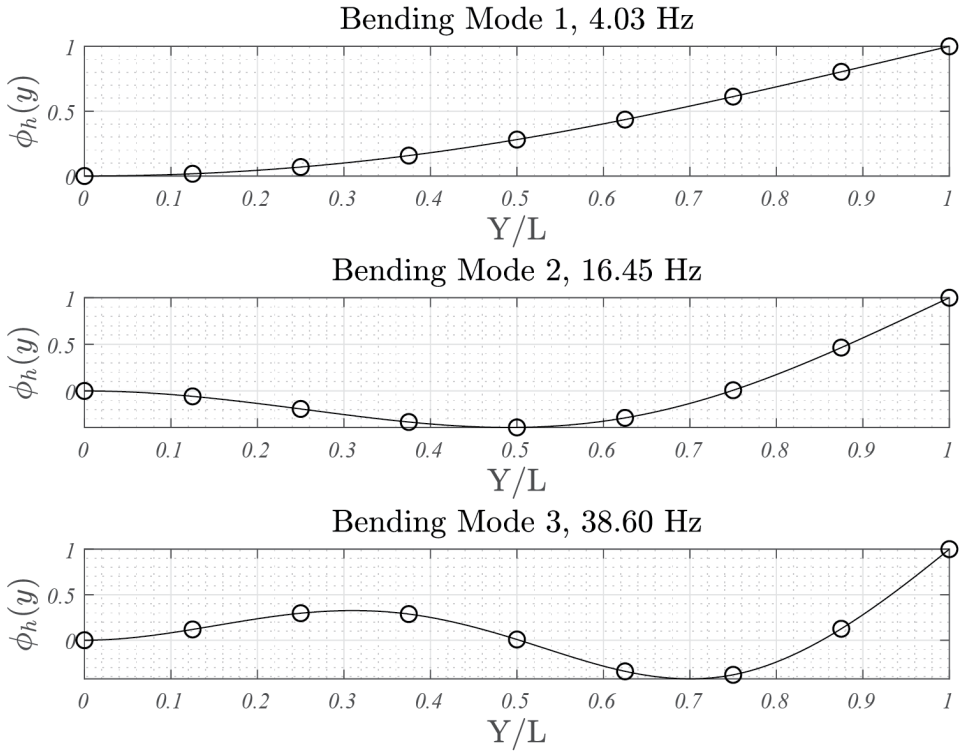

Figure 7.22 Elastic Wing Bending Mode Shapes

Figure 7.23 shows mode shapes of the first two torsional modes.

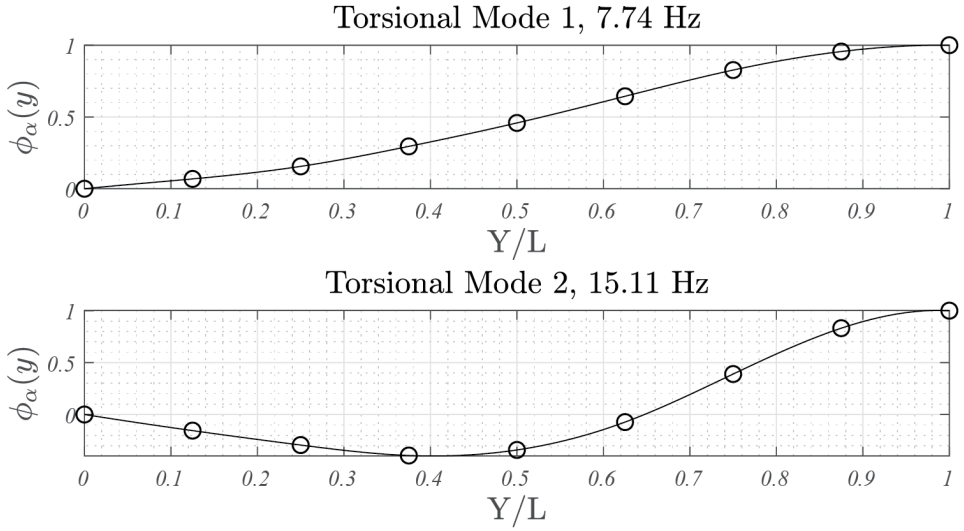

Figure 7.23 Elastic Wing Torsional Mode Shapes

A flutter study of the open-loop system is conducted to determine the unstable airspeed. All flutter simulations are performed with a structural damping coefficient of $g = 0.03$ and a second-order actuator with $10\,Hz$ bandwidth. Figure 7.24 shows the V-F and V-g curves for the system with linear torsional stiffness in the absence of freeplay.

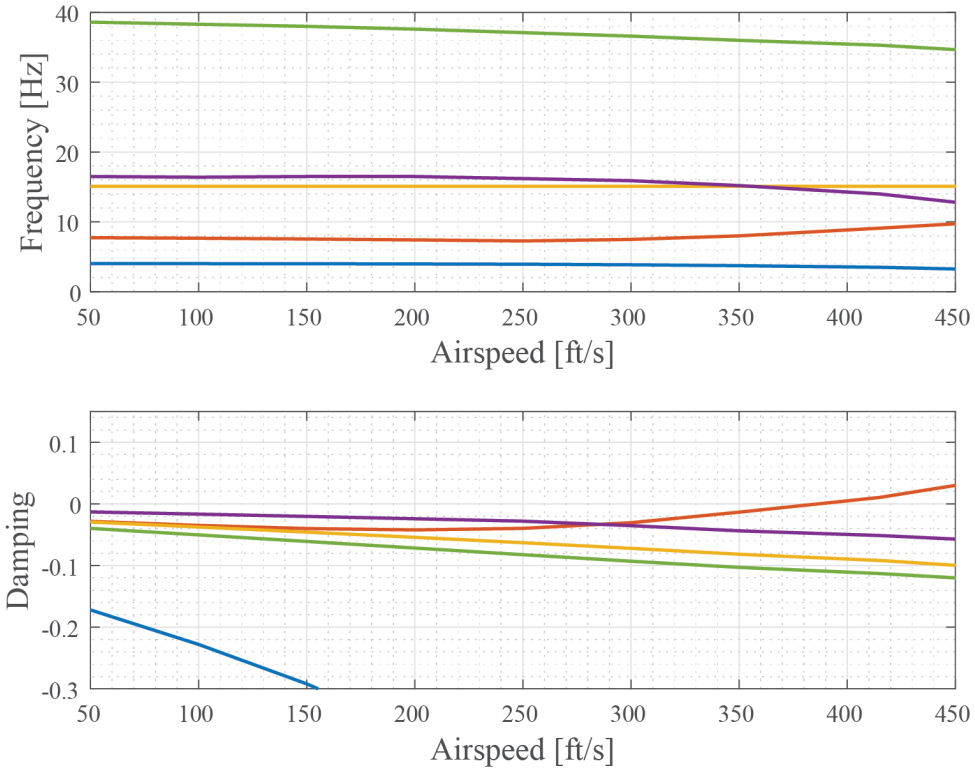

Figure 7.24 Elastic Wing V-F and V-g Curves

Based on the the V-g plot, the flutter speed of the wing, where the first torsional mode becomes unstable, is approximately $400\,ft/s$. This is the airspeed at which all flutter simulations are performed. Figure 7.25 shows the physical response of the system to an initial condition. The response appears to be a nonlinear response and reaches an LCO. This is due to the nature of the application of the loads to the structure, where they are in essence follower forces. The pressure forces on each box are always normal to the surface, so at high twist angles the forces primarily point in the direction of flow, which is not a DOF considered in the analysis. Thus, the greater the angle of twist, the less the DOFs are excited.

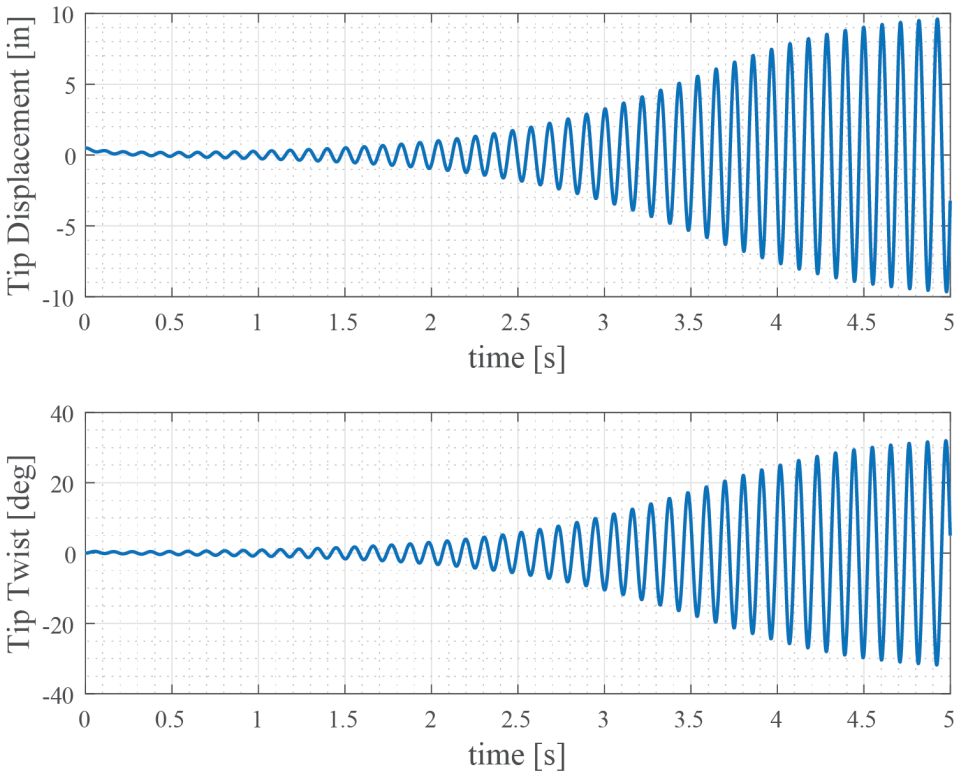

Figure 7.25 Elastic Wing Open-Loop Response to Initial Condition $V = 400\,ft/s$

The initial condition is implemented as either a unit displacement or unit rotation of a single mode. The flutter characteristics of the system are found to be independent of the perturbed mode. Based on this, it is inferred that the flutter characteristics should be independent of gust length, as shorter gusts will perturb the higher frequency modes and longer gusts will perturb lower frequency modes. To verify this, the open-loop response of the system to a gust is simulated for a series of gust lengths. Figure 7.26 shows the system response to a $30\,ft$ gust.

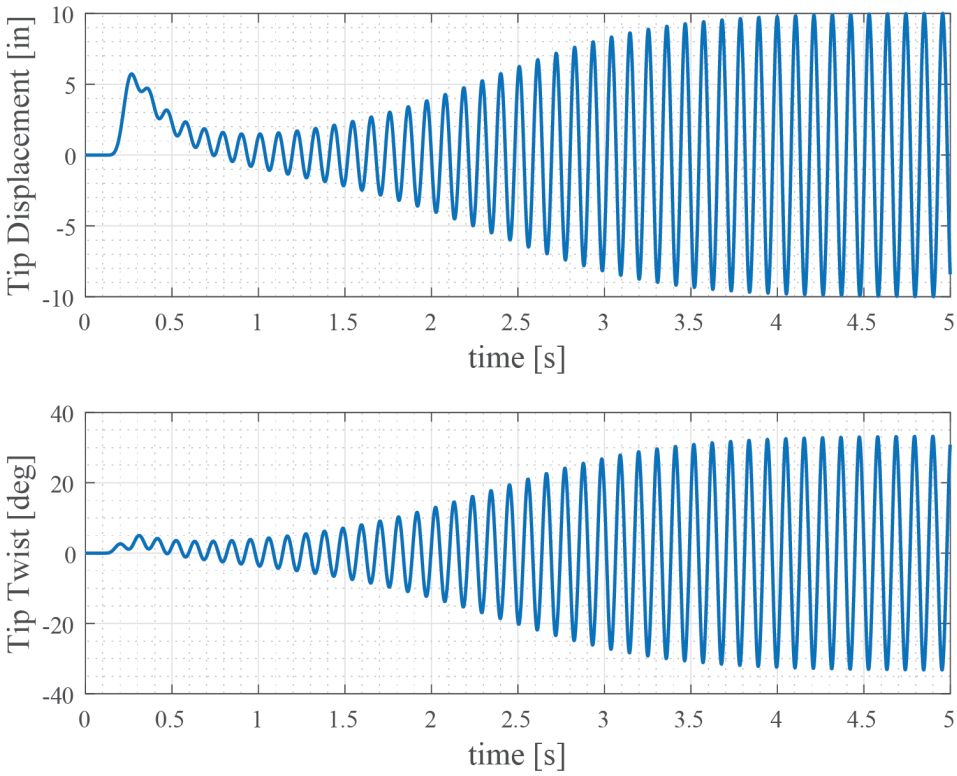

Figure 7.26 Elastic Wing Open-Loop Response to 30 ft Gust $V = 400\,ft/s$

At $400\,ft/s$, the frequency of the gust is approximately $6.7\,Hz$ and thus only excites the lower frequency modes. The gust length can be reduced to increase its frequency, however the minimum gust length defined in 14 CFR §25.341 [34] is 30 ft and therefore is the shortest gust used in this analysis. Figure 7.27 shows the system response to a 100 ft gust.

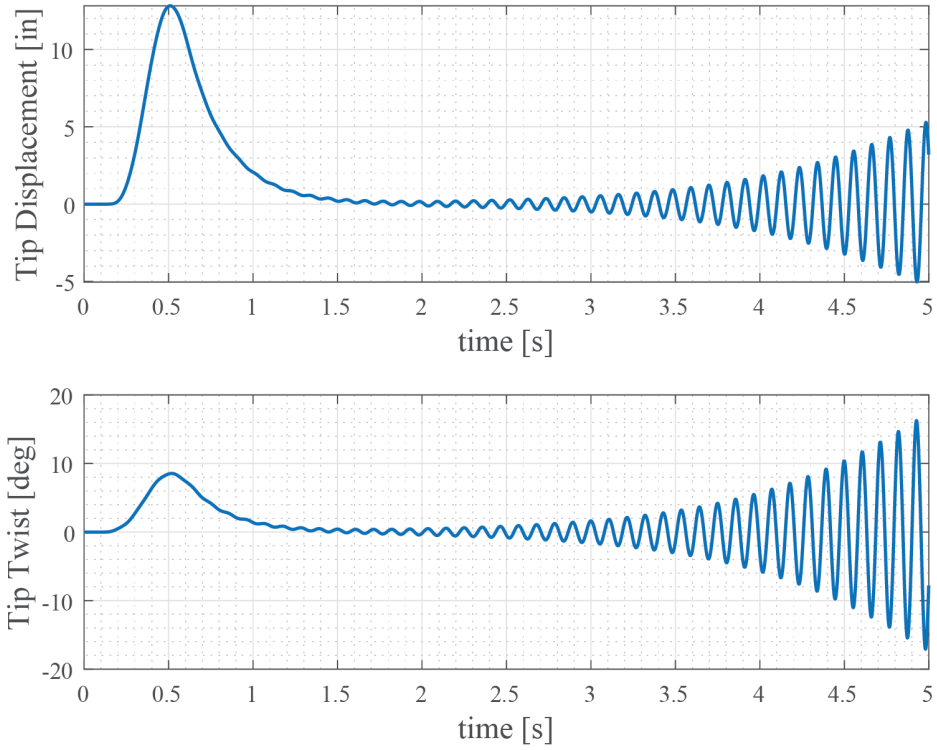

Figure 7.27 Elastic Wing Open-Loop Response to 100 ft Gust $V = 400\,ft/s$

At 400 ft/s, the frequency of the gust is approximately 2 Hz and has difficulty exciting the flexible dynamics; the system requires a very large simulation time for the instabilities to be seen. Therefore, the 30 ft gust is used to excite the system for all further simulations.

Now the closed-loop response with an LQR and MRAC are evaluated. The flutter simulations are set up such that the leading edge of the gust impacts the system at $t = 0.05s$ and the controller becomes active at $t = 0.50s$. This allows adequate time for the unsteady dynamics to build up before the controller must stabilize the system. In reality, the controller would always be on, leading to improved responses as the unstable dynamics do not have time to build up. If left for too long, the dynamics build up to a point where the controller is no longer able to stabilize the system, and the control surface will saturate. This highlights the need for the controller to always be active.

First, an LQR controller is tuned at a stable airspeed to increase the damping in the

system. This flight condition is chosen to be at $V = 300\,ft/s$. Similar to the two-dimensional system, the tuning matrices $[Q]$ and $[R]$ are diagonal and defined as follows

$$[Q] = \begin{bmatrix} Q_1 & \cdots & 0 \\ \vdots & \ddots & \vdots \\ 0 & \cdots & Q_n \end{bmatrix} \qquad [R] = \begin{bmatrix} R_1 & \cdots & 0 \\ \vdots & \ddots & \vdots \\ 0 & \cdots & R_q \end{bmatrix}$$

The LQR is tuned with the $[Q]$ and $[R]$ matrices given in Tables 7.15 and 7.16.

Table 7.15 Three-Dimensional $[Q]$ Tuning Values

Tuning Parameter	Value	Tuning Parameter	Value
Q_1	0.50	Q_7	0.15
Q_2	0.10	Q_8	0.10
Q_3	0.10	Q_9	0.10
Q_4	$100\left(\frac{180}{\pi}\right)$	Q_{10}	2.50
Q_5	$10\left(\frac{180}{\pi}\right)$	Q_{11}	1.00
Q_6	0.00	Q_{12}	0.00

Table 7.16 Three-Dimensional $[R]$ Tuning Values

Tuning Parameter	Value
R_1	2.00

Figure 7.28 shows the open-loop and closed-loop response to the LQR at $V = 300\,ft/s$ to illustrate the additional damping added by the control system. As the first torsional mode is the flutter mode, the focus is adding torsional damping. Figure 7.29 shows the control input and elastic flap deflection for this case. The commanded control deflection and actual control deflection appear to coincide as the elastic flap deflection is relatively small.

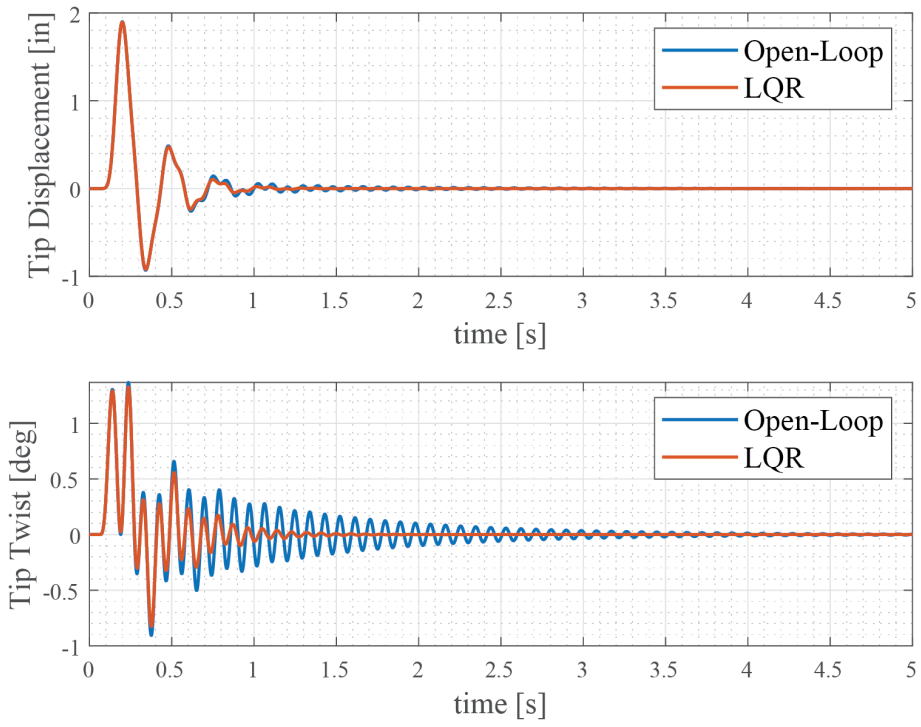

Figure 7.28 Open-Loop and LQR Response at $V = 300\, ft/s$

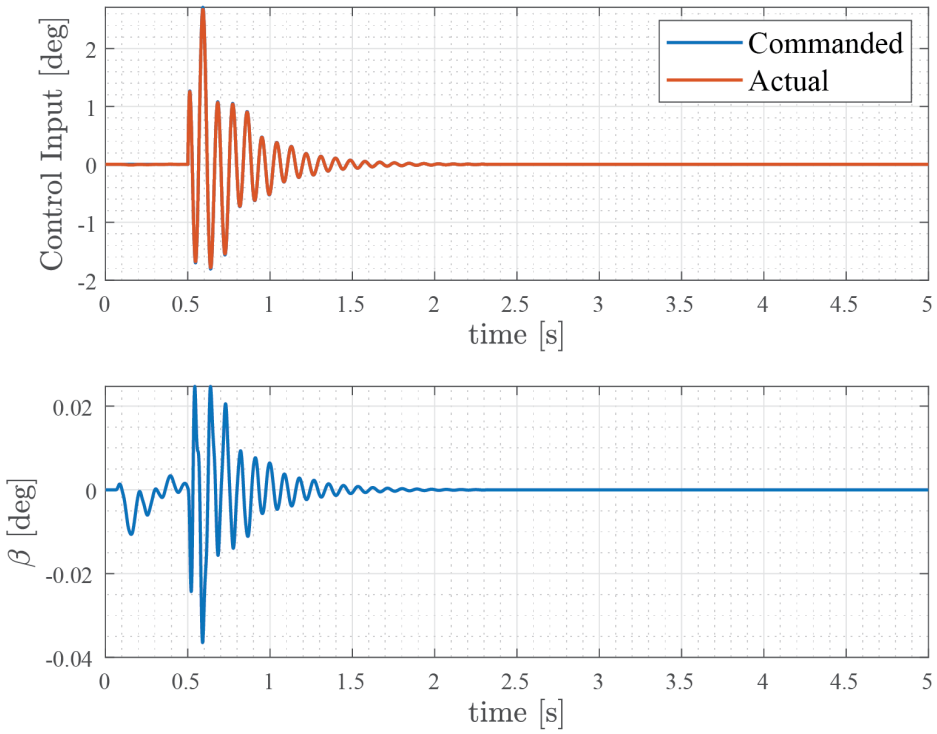

Figure 7.29 LQR Control Input and Elastic Flap Deflection at $V = 300\, ft/s$

Next the MRAC is developed for an airspeed of $V = 400\, ft/s$ to compare its performance to a poorly tuned LQR controller. The baseline adaptation rates and initial gains are

$$[\Gamma_y]_0 = \begin{bmatrix} \Gamma_1 & \cdots & 0 \\ \vdots & \ddots & \vdots \\ 0 & \cdots & \Gamma_n \end{bmatrix} \qquad [K_{x_0}] = \begin{bmatrix} K_{x_1} & \cdots & K_{x_N} \end{bmatrix}$$

The MRAC is tuned with the adaptation rates given in Table 7.17

Table 7.17 Three-Dimensional $[\Gamma_y]_0$ Tuning Values

Adaptation Rate	Value	Adaptation Rate	Value
Γ_1	1.00	Γ_7	0.05
Γ_2	0.10	Γ_8	0.10
Γ_3	0.10	Γ_9	0.10
Γ_4	12.00	Γ_{10}	1.00
Γ_5	1.00	Γ_{11}	1.00
Γ_6	0.10	Γ_{12}	0.10

and the initial gains in Table 7.18.

Table 7.18 Three-Dimensional $[K_{x_0}]$ Gains

Initial Gain	Value	Initial Gain	Value
K_{x_1}	-0.0053	K_{x_7}	0.0391
K_{x_2}	-0.0488	K_{x_8}	0.0092
K_{x_3}	-0.0864	K_{x_9}	-0.0232
K_{x_4}	-0.0250	$K_{x_{10}}$	-0.1805
K_{x_5}	-0.2136	$K_{x_{11}}$	-0.1140
K_{x_6}	0.000	$K_{x_{12}}$	0.0000

Next, the closed-loop response with an LQR and MRAC is studied. Figure 7.30 shows the response with each controller active. This shows that both controllers are able to stabilize the system, but the MRAC is more effective at increasing the damping and settles the system more quickly.

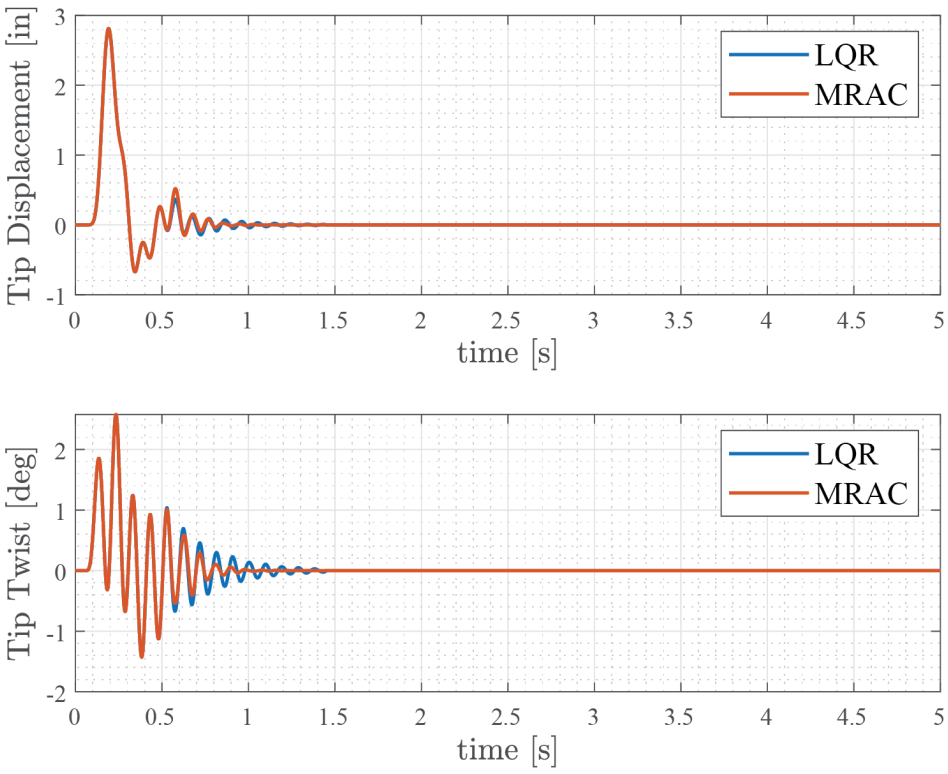

Figure 7.30 Elastic Wing Closed-Loop Response at $V = 400\, ft/s$

In addition to the bending and torsion responses, the control deflection and elastic flap deflection are analyzed. Figure 7.31 shows the actual flap deflection and elastic flap deflection. The MRAC provides a more aggressive input, which aids the settling time but leads to more elastic flap deflection.

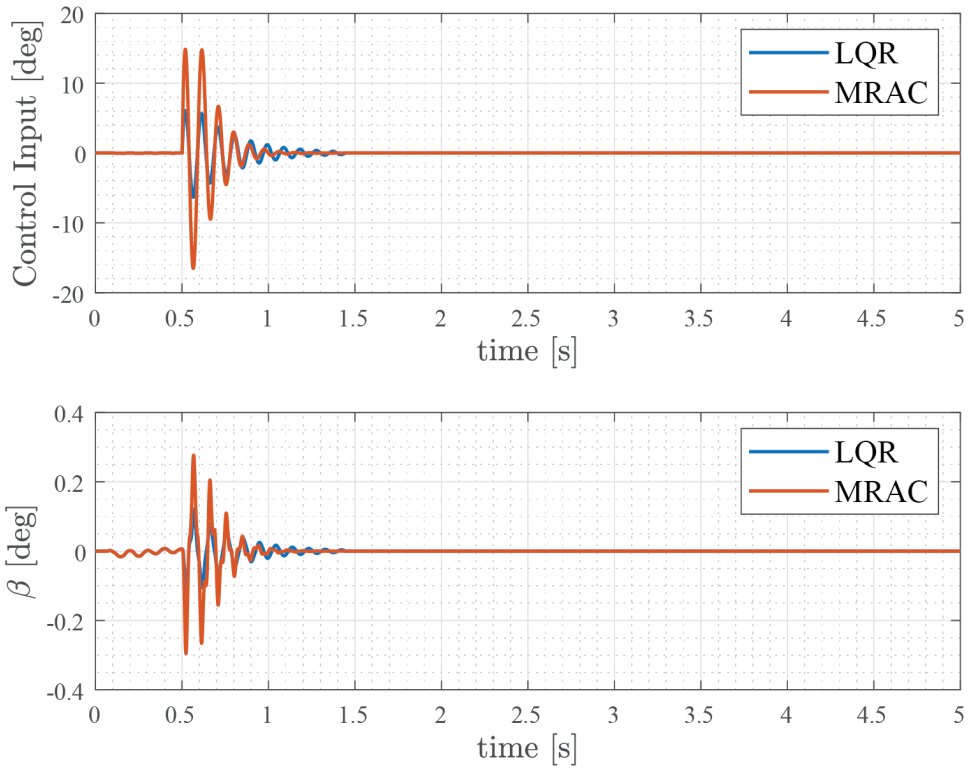

Figure 7.31 Elastic Wing Control Input and Flap Deflection at $V = 400\, ft/s$

Table 7.19 gives the 5% settling times for the vertical tip displacement and tip twist for the LQR and MRAC, respectively. This reinforces the assertion that the MRAC is more effective at attenuating transience; the settling time for wing bending is reduced by 6% and the settling time for wing torsion is reduced by 25%. One reason for the increased attenuation of wing torsion could be attributed to the higher adaptation rates placed on the torsional modes, as shown in Table 7.17.

Table 7.19 Elastic Wing Settling Time (5% Steady-State)

	h	α
LQR	0.731 s	1.01 s
MRAC	0.688 s	0.76 s

Examining the time histories over a shorter span provides greater insight into system response. Figure 7.32 shows the response over a one second span.

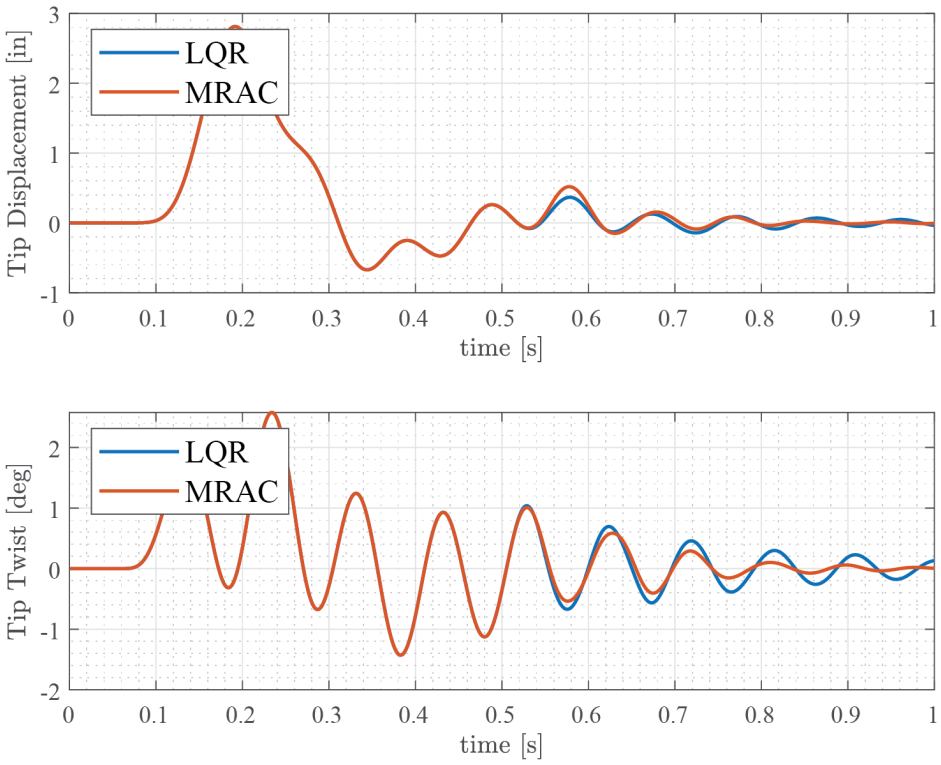

Figure 7.32 Elastic Wing Closed-Loop Response at $V = 400\, ft/s$ Zoomed

Figure 7.33 shows the control input and elastic flap deflection over a one second span. The MRAC initially commands a greater positive deflection than the LQR. This causes the small increase in the tip displacement but reduction in the tip twist shown in Figure 7.32.

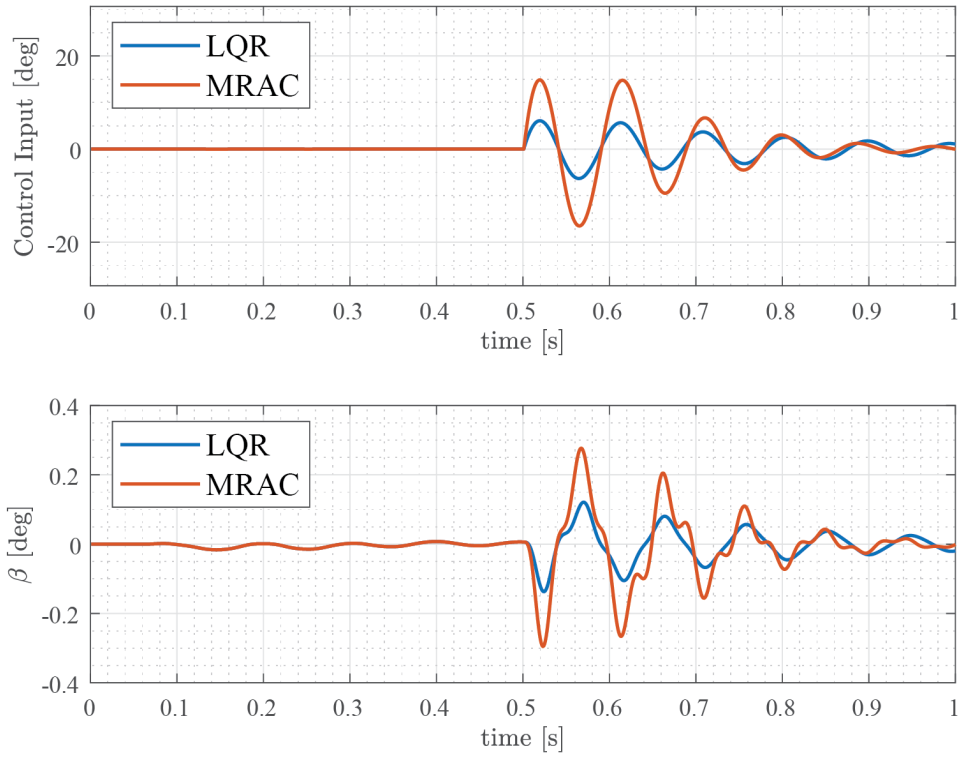

Figure 7.33 Elastic Wing Closed-Loop Response at $V = 400\, ft/s$ Zoomed

This clarifies the relationship between the wing twist and flap deflection. It is important to note the values of Q used to tune the baseline LQR controller for this configuration. As the unstable mode is the first torsional mode, the controller was tuned to add torsional damping. At 0.5 seconds, when the controller is activated, the wing has a positive torsional rate. The controller deflects the control surface in the positive direction (trailing edge down) to produce a negative torsional moment, counteracting the torsion rate.

For cases with nonlinear torsional stiffness, the same polynomial as the two-dimensional case is used, but scaled for the first torsion modal stiffness. The resulting polynomial coefficients are

Table 7.20 Elastic Wing First Torsion Stiffness Polynomial Coefficients

Coefficient	Value
k_{α_0}	2.19×10^4
k_{α_1}	-4.48×10^5
k_{α_2}	2.89×10^7
k_{α_3}	-1.88×10^8
k_{α_4}	3.79×10^8

The open-loop response of the system with a torsional nonlinearity is simulated in Figure 7.34. The introduction of the nonlinear stiffness causes the system to diverge more quickly and reach an LCO of approximately $\pm 40°$ of tip torsion and ± 12 in of tip deflection.

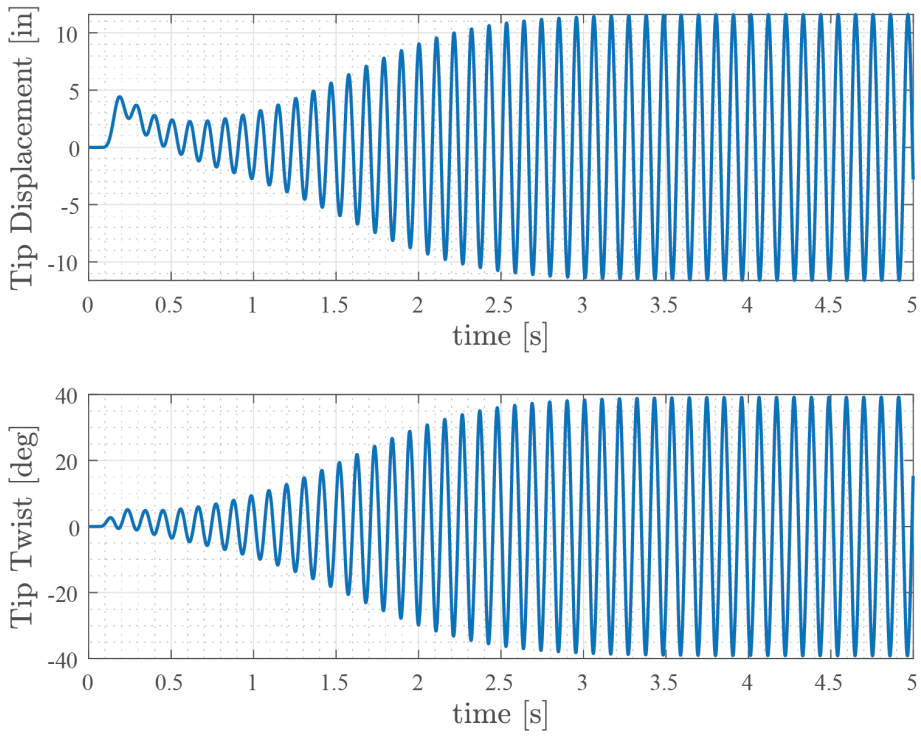

Figure 7.34 Elastic Wing Open-Loop Response with Torsional Nonlinearity at $V = 400 ft/s$

Next, the closed-loop response with an LQR and MRAC is studied. Figure 7.35 shows the closed-loop tip displacement and twist with nonlinear torsion for the LQR and MRAC. Both controllers are able to stabilize the system but the MRAC settles the system faster than the LQR.

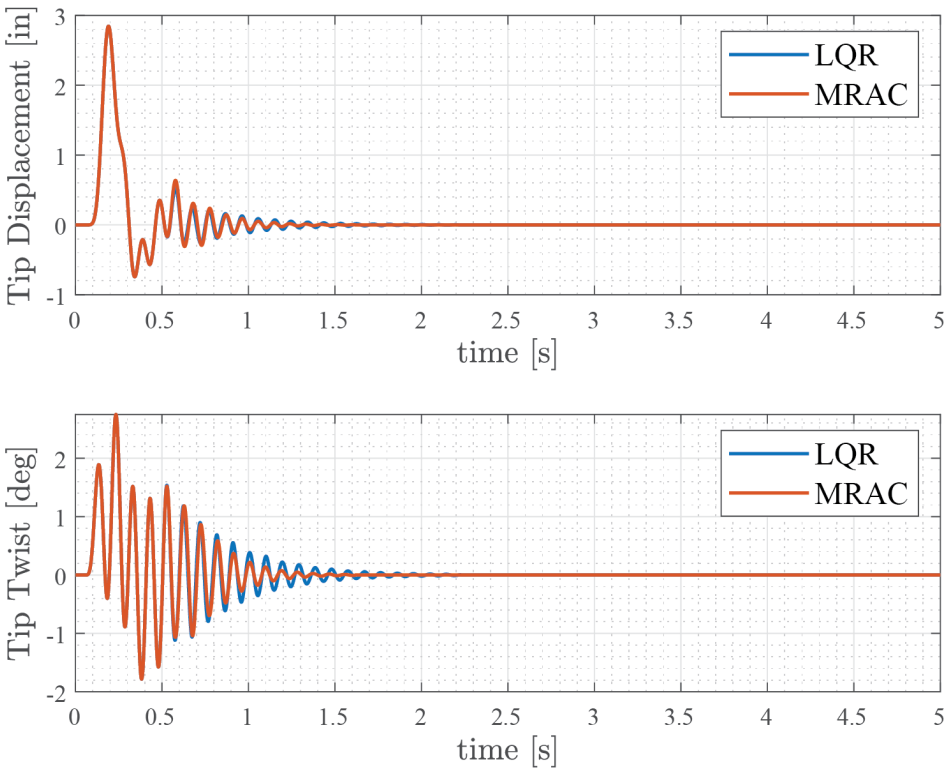

Figure 7.35 Elastic Wing Closed-Loop Response with Torsional Nonlinearity at $V = 400 ft/s$

Figure 7.36 shows the control input and flap angle for the LQR and the MRAC. The MRAC commands a more aggressive control input, which aids in settling the system, but causes more elastic flap deflection.

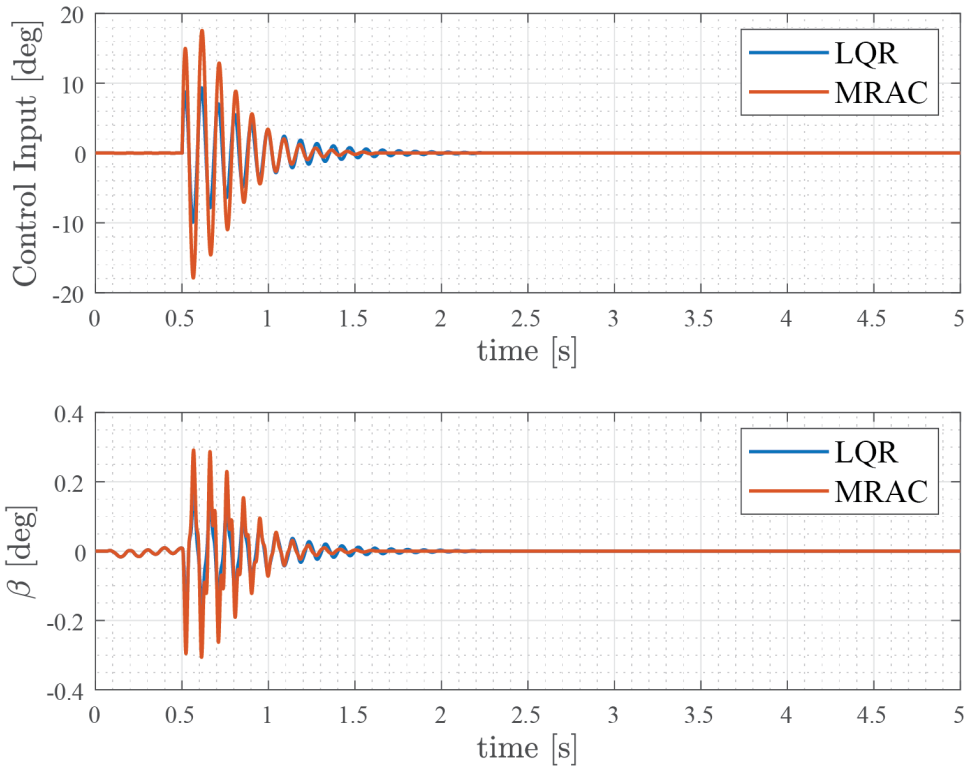

Figure 7.36 Elastic Wing Control Input and Flap Deflection with Nonlinear Torsional Stiffness at $V = 400 ft/s$

Table 7.21 gives the 5% settling times for the vertical tip displacement and tip twist for the LQR and MRAC, respectively. This reinforces the assertion that the MRAC is more effective at attenuating transience; the settling time in wing bending reduces by 15% and the settling time in wing torsion reduces by 27%. However, the cost of this reduction in settling time is an increase in the required control surface deflection.

Table 7.21 Elastic Wing Settling Time (5% Steady-State) with Nonlinear Torsion

	h	α
LQR	1.43 s	1.76 s
MRAC	1.22 s	1.29 s

Next, the system is analyzed with linear torsional stiffness and freeplay. For this case, the simulations are run with freeplay limits of $\pm 1°$. Figure 7.37 shows the open-loop response

of the system with freeplay present. When comparing the response to the baseline linear system in Figure 7.26, the freeplay appears to provide some attenuation as the maximum tip displacement reaches 7 inches as compared to 10 inches. Similarly, the tip twist reaches a maximum of 22° as compared to 30° in the baseline system.

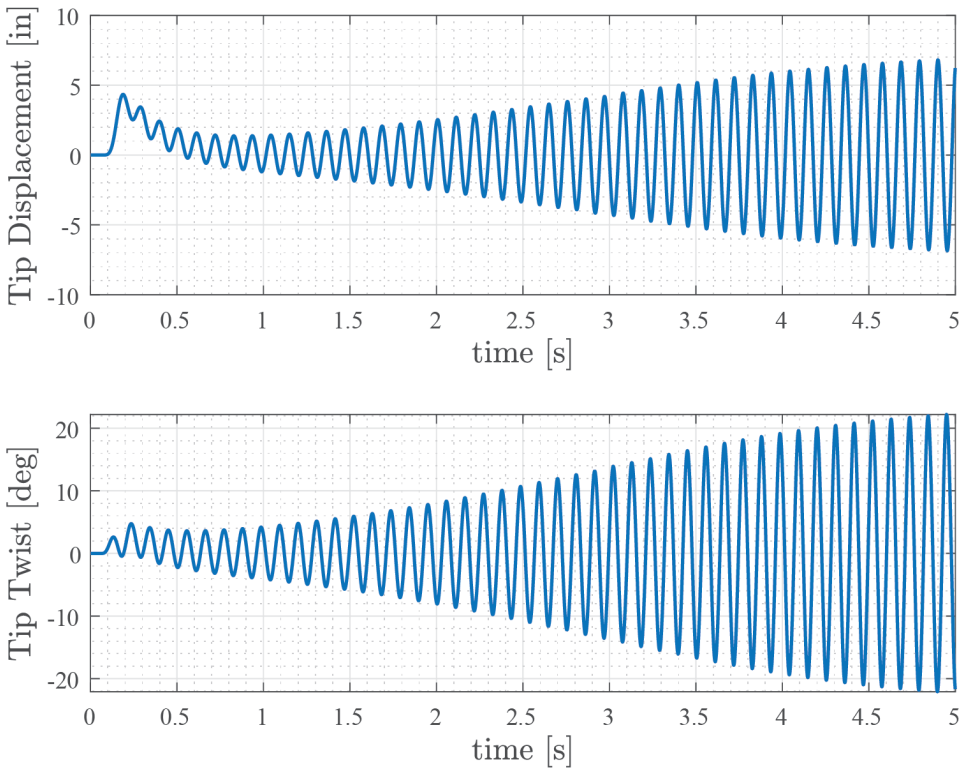

Figure 7.37 Elastic Wing Open-Loop Response at with Freeplay at $V = 400 ft/s$

Figure 7.38 shows the actual control surface displacement and the freeplay angle for this case. As there is no commanded control surface deflection, the actual deflection is equal to the freeplay angle. This shows that the flap oscillates within the freeplay limits until approximately 2.5 seconds, upon which it reaches the freeplay limit and rebounds. This initiates a more aggressive oscillation, as the flap impacts and then rebounds off of the upper and lower freeplay limits.

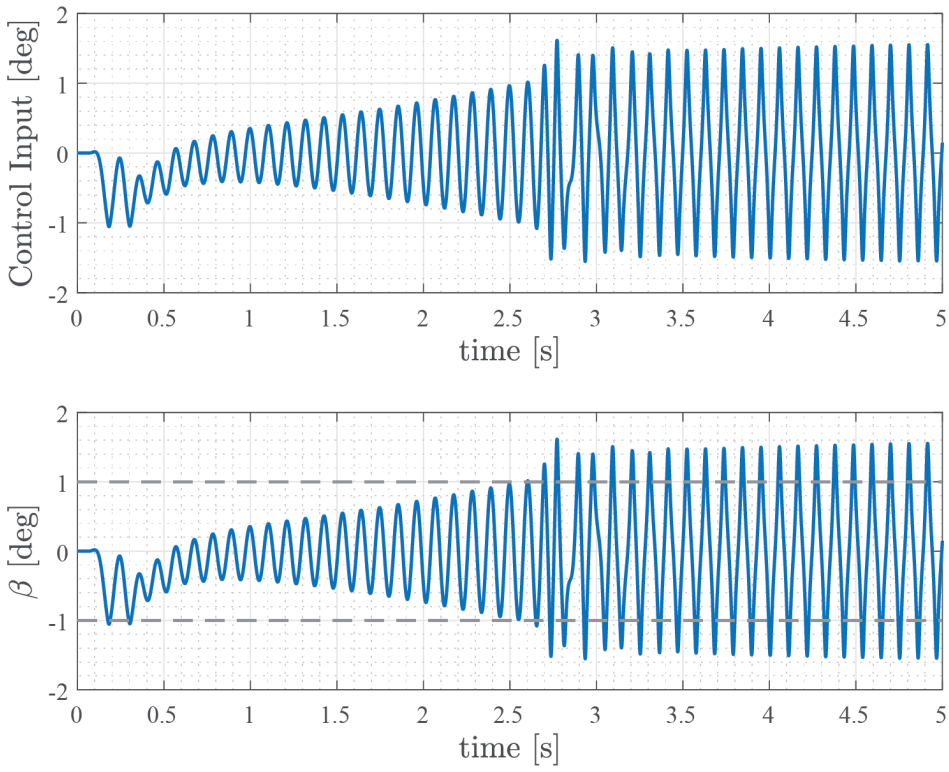

Figure 7.38 Elastic Wing Control Input and Flap Deflection at with Freeplay at $V = 400ft/s$

Figure 7.39 shows the closed-loop tip displacement and twist with freeplay for the LQR and MRAC. Both controllers are able to stabilize the system, but the MRAC settles the system quicker than the LQR. For both controllers, after the initial oscillation subsides, the system reaches an equilibrium point; the freeplay angle of the LQR case is $\beta = -0.42°$ and the tip twist is $\alpha = -0.015°$; the freeplay angle of the MRAC case is $\beta = -0.45°$ and the tip twist is $\alpha = -0.017°$. Figure 7.40 shows the control input and flap angle for the LQR and the MRAC. The MRAC commands a more aggressive control input, which aids in settling the system, but causes more elastic flap deflection. This causes a more aggressive rebound off of the freeplay limits. For both cases, the drift in the control surface is visible where it settles at an aerodynamic equilibrium point.

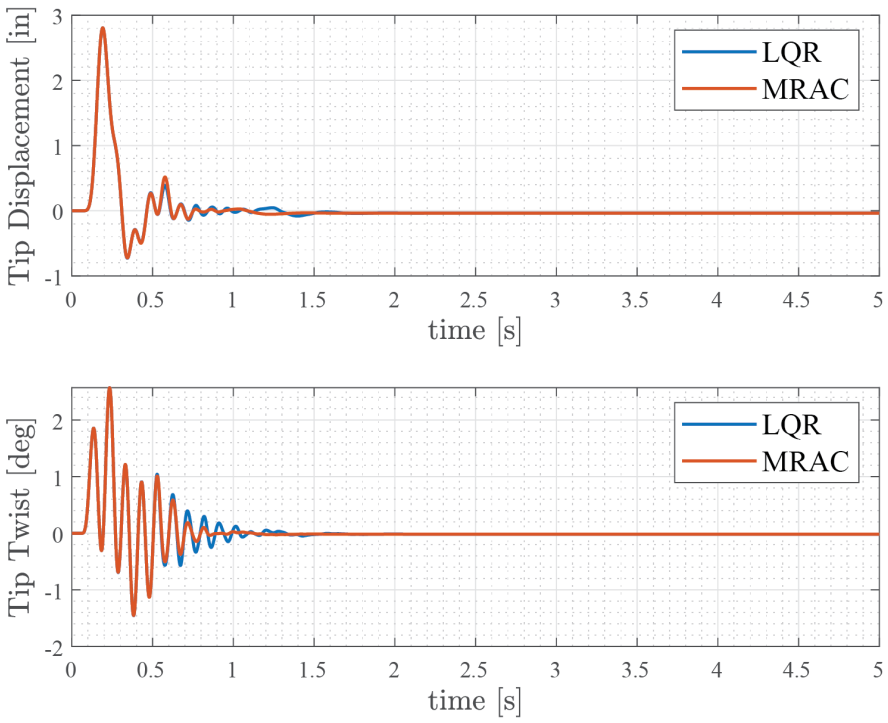

Figure 7.39 Elastic Wing Closed-Loop Response with Freeplay at $V = 400 ft/s$

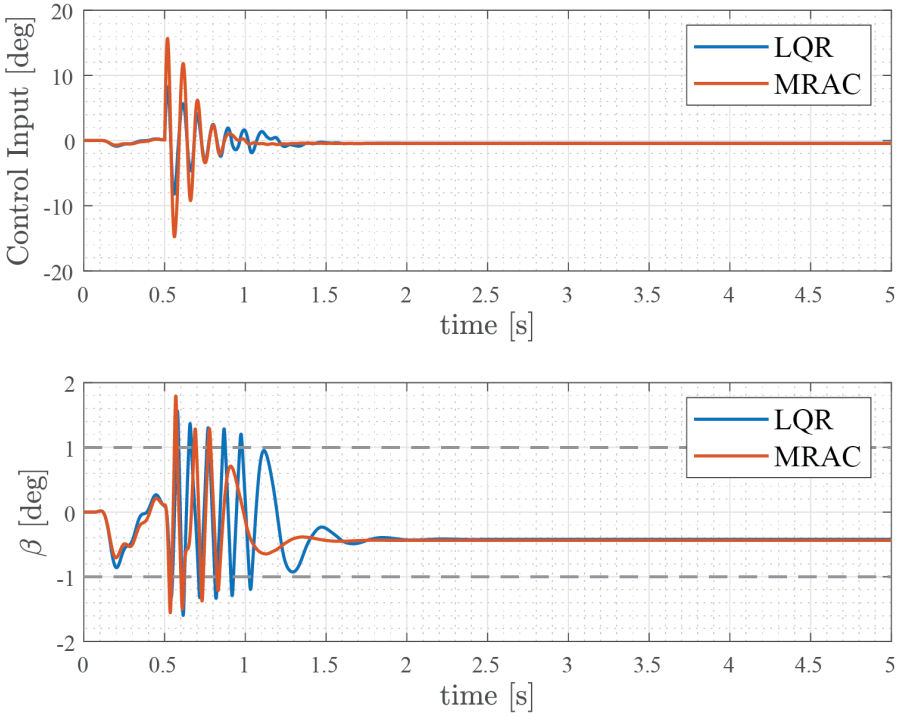

Figure 7.40 Elastic Wing Control Input and Flap Deflection at with Freeplay at $V = 400 ft/s$

Table 7.22 gives the 5% settling times for the vertical tip displacement and tip twist for the LQR and MRAC, respectively. This reinforces the assertion that the MRAC is more effective at attenuating transience; the settling time in wing bending reduces by 15% and the settling time in wing torsion reduces by 20%.

Table 7.22 Elastic Wing Settling Time (5% Steady-State) with Freepaly

	h	α
LQR	0.875 s	1.026 s
MRAC	0.736 s	0.820 s

Overall, a direct model reference adaptive controller is able to provide a more desirable response than a poorly tuned LQR. In each case, the MRAC drives faster settling times than the LQR and shows robustness when nonlinear torsion and freeplay are introduced.

7.3 Elastic Wing and Aircraft

This section presents the results for the open-loop and closed-loop simulations for a flexible wing aircraft. This utilizes the same wing as Section 7.2 with the addition of the aircraft rigid body dynamics. Table 7.23 provides the estimated structural and mass properties required for the full aircraft simulations. These values include the properties of the wing.

Table 7.23 Aircraft Structural Data

Parameter	Value
W	$12,000\, lb_f$
I_{xx}	$28000\ slug - ft^2$
I_{yy}	$18800\ slug - ft^2$
I_{zz}	$47000\ slug - ft^2$
I_{xz}	$1300\ slug - ft^2$

Table 7.24 provides the estimated aerodynamic coefficients required for full aircraft simulations.

Table 7.24 Aircraft Aerodynamic Coefficients

Parameter	Value
T_{max}	$5,900\,lb_f$
C_{M_0}	0.0316
C_{M_α}	-0.64
$C_{L_{\delta_e}}$	0.46
$C_{M_{\delta_e}}$	-1.24
C_{L_q}	4.7
C_{M_q}	-15.5

Since the wing used in these simulations is identical to that of Section 7.2, additional V-g analyses are not required. The primary focus of this section is to understand the impact of the flutter suppression system on rigid-body dynamics. To quantify the effects of the elastic coupling on the rigid-body dynamics, a similar set of simulations to Section 7.2 is performed. However, as the response of the wing with a torsional nonlinearity is similar to that of the wing with linear torsional stiffness, the only coupled cases being analyzed are: the elastic wing with linear torsional stiffness; the elastic wing with linear torsional stiffness and freeplay.

First, the trim condition of the aircraft must be found. This is calculated by applying the steady-state condition to Eq. (3.181) through Eq. (3.185) with the equilibrium aerodynamic forcing described in Eq. (4.33). For a given flight condition, the angle of attack is set, and the elastic steady-state solution is calculated as well as the required elevator deflection to maintain the angle of attack. This process is repeated until the balance of forces in the vertical direction is satisfied. For the stable condition of $V = 300\,ft/s$, this is an angle of attack of 4.32° and an elevator deflection of 2.44°. For the unstable condition of $V = 400\,ft/s$, this is an angle of attack of 3.48° and an elevator deflection of 1.77°.

Next, the open-loop response of the full aircraft is simulated for a $30\,ft$ gust. The simulation is unstable for speeds at or above the flutter speed and quickly diverges. Therefore, the open-loop response is only analyzed for the stable condition of $V = 300\,ft/s$. Figure 7.42 shows the open-loop response of the elastic states to a $30\,ft$ gust. Figure 7.42 shows selected

rigid-body perturbation states of interest. This includes pitch rate Δq, pitch angle $\Delta\theta$, and altitude Δh. The elastic disturbance is somewhat evident in the rigid-body states. However, due to the inertia of the aircraft and differences in the frequencies, the elastic motion does not have a significant effect on the aircraft as a whole.

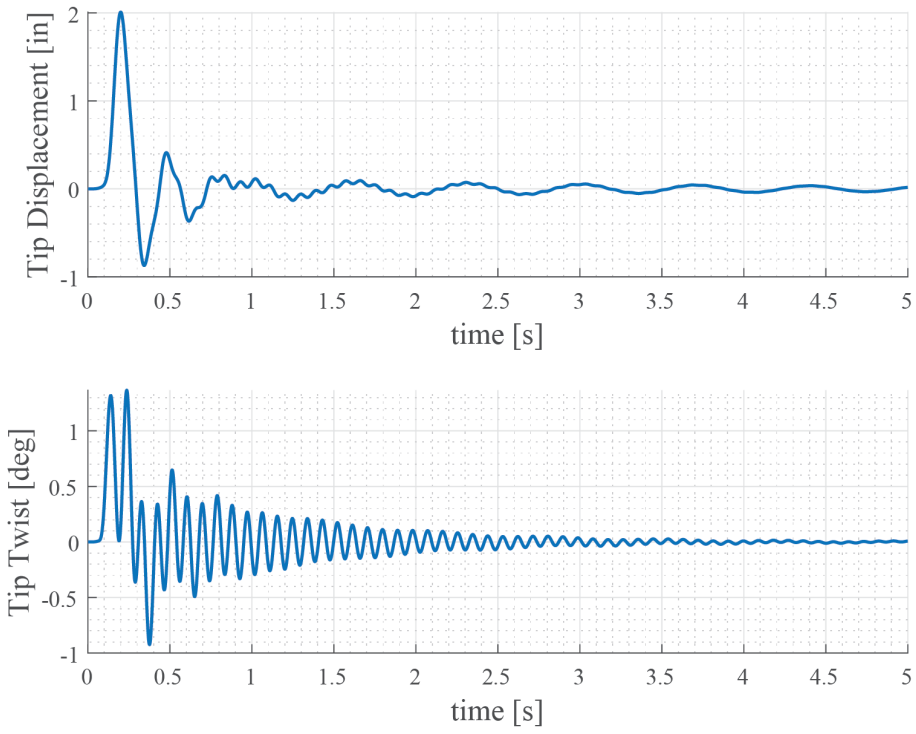

Figure 7.41 Aircraft Open-Loop Elastic Response at $V = 300 ft/s$

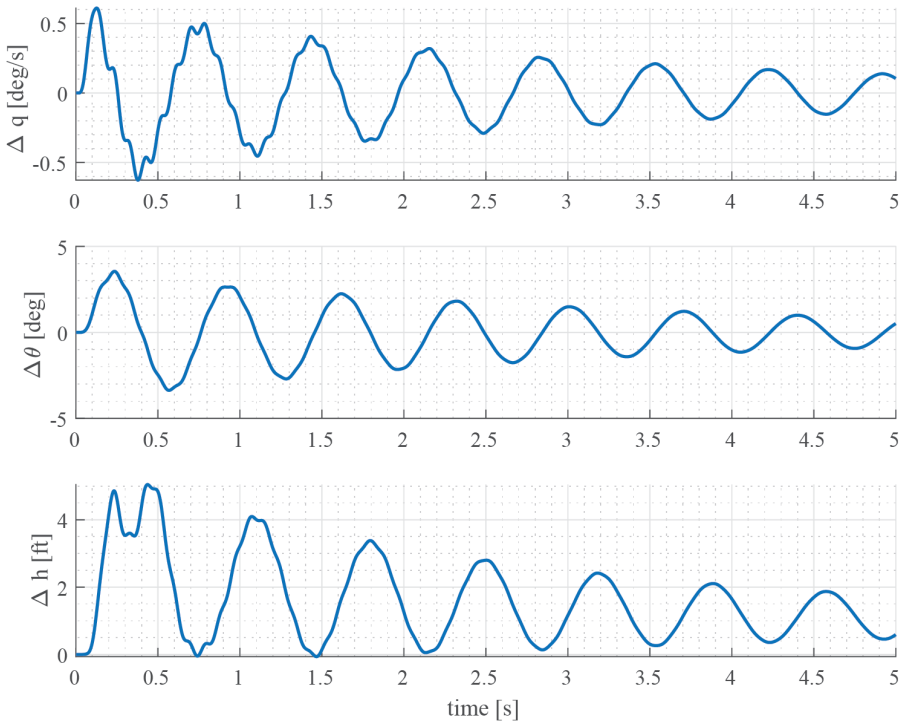

Figure 7.42 Aircraft Open-Loop Rigid-Body Response at $V = 300 ft/s$

Next, the aircraft is simulated at the flutter speed with an MRAC active. Figure 7.43 shows the closed-loop response of the elastic states. After the controller attenuates the vibration due to the gust, artifacts of rigid body motion are still evident. As the aircraft pitches about its equilibrium point, the change in lift leads to some wing bending and torsion.

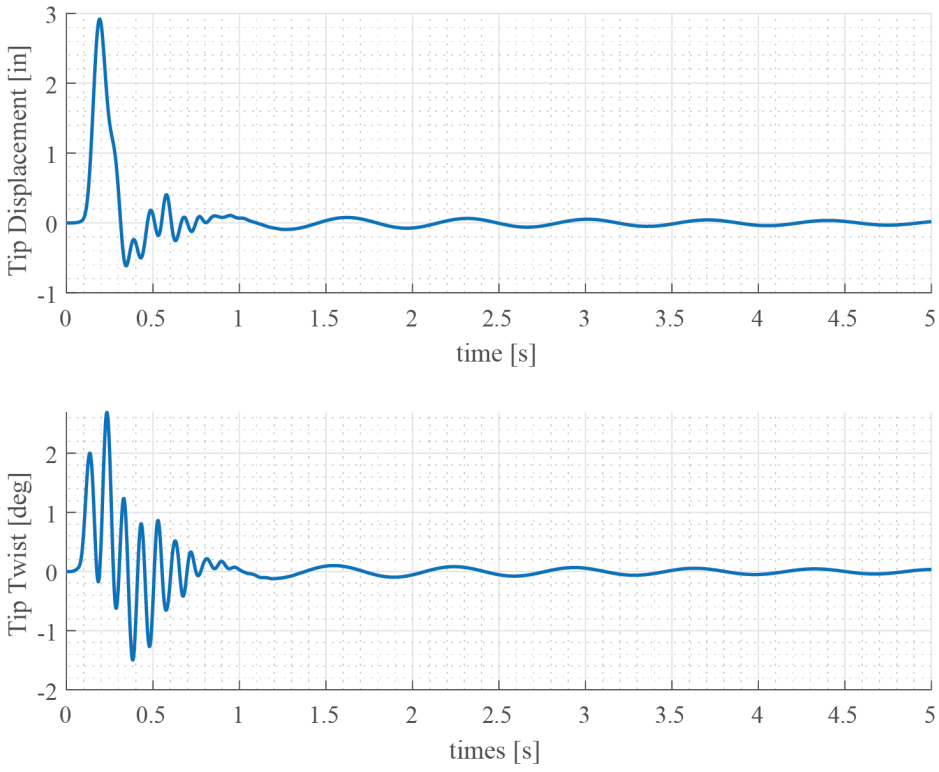

Figure 7.43 Aircraft Closed-Loop Elastic Response at $V = 400 ft/s$

Figure 7.44 shows the rigid-body perturbation states with the MRAC active. Small oscillations appear in the pitch rate due to wing torsion, however, the pitch angle and change in altitude are relatively undisturbed.

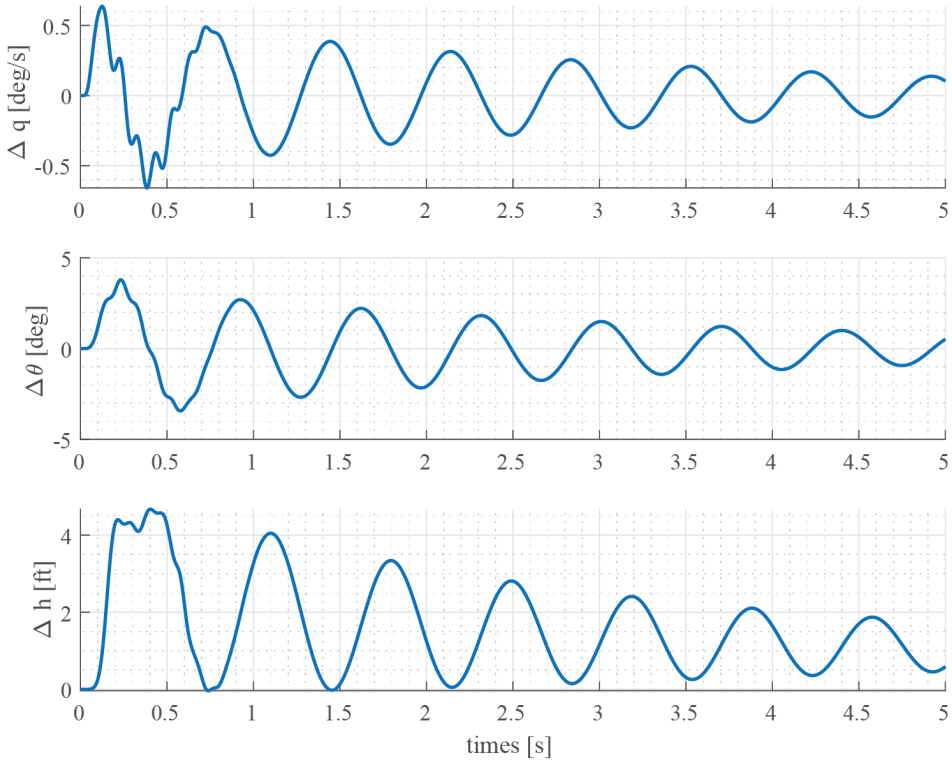

Figure 7.44 Aircraft Closed-Loop Rigid-Body Response at $V = 400 ft/s$

Figure 7.45 shows the closed-loop response of the elastic states with freeplay present. Similar to the baseline case, once the initial oscillations are damped out, some artifacts of rigid-body motion are still present. Figure 7.46 shows the closed-loop rigid-body perturbation states. Similar to the baseline case, there is some elastic motion present in the pitch rate response. However, the flexible excitation only has minor effects on the overall rigid-body motion. In this case, the MRAC provides a more aggressive response to attenuate wing bending and this reduction in lift appears in the Δh response.

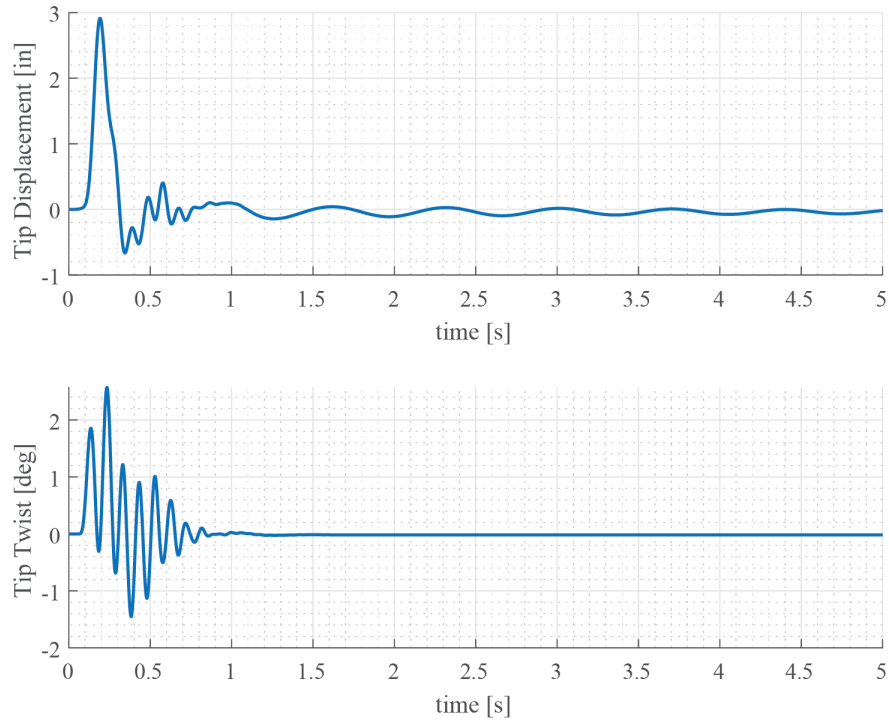

Figure 7.45 Aircraft Closed-Loop Elastic Response at $V = 400 ft/s$

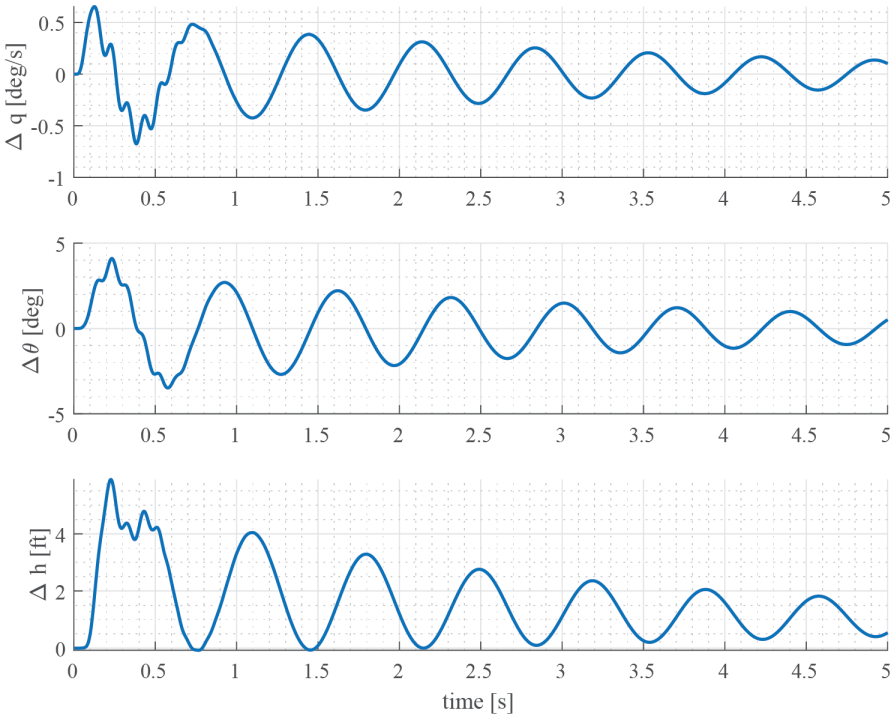

Figure 7.46 Aircraft Closed-Loop Rigid-Body Response at $V = 400 ft/s$

Combining a flexible wing with rigid-body aircraft motion does not degrade the performance of the MRAC. In the cases presented, byproducts of the elastic motion can be seen in the rigid-body response; however, it has little effect on the overall rigid-body motion. On the contrary, rigid-body motion drives a small elastic response.

8 Conclusions

This work details the process for the development and analysis of direct model reference adaptive control for active flutter suppression and load alleviation. The development of structural dynamics models for a pitch-plunge-flap airfoil, a cantilevered elastic wing with N flexible modes, and a longitudinal-only rigid-body aircraft model with a flexible wing are presented. Additional complexities are modeled in the form of nonlinear torsional stiffness and actuator freeplay. These dynamics models serve as a test bed for direct model reference adaptive control and offer a method of direct comparison to a linear controller.

The structural dynamics of the elastic wing are developed using energy methods. The first step is applying unit load analysis to develop the flexibility influence coefficients of the structure. Once this is known, a matrix iteration solution to the structural eigenvalue problem is used to calculate the uncoupled modes of vibration. Then, a modal transformation is used to reduce the structure into generalized coordinates where the structural dynamics calculations are carried out. The development of the longitudinal-only rigid-body aircraft equations of motion is also presented in addition to the methods used to couple rigid-body and flexible dynamics.

Once a structural dynamics model is developed for all three systems, the aerodynamics are derived. The pitch-plunge-flap airfoil utilizes quasi-steady aerodynamics, while unsteady vortex-lattice aerodynamics are used in the solutions for the cantilevered elastic wing and the flexible wing aircraft. A detailed development of the unsteady vortex-lattice method is presented as well as the steps for its implementation in time-domain aeroelastic simulations.

Next, a direct model reference adaptive controller is presented. This controller allows freedom to dictate the behavior of the system over a wide range of flight conditions without gain scheduling. In addition, this controller can provide a level of fault tolerance to unmodeled dynamics, nonlinearities, and disturbances. For active flutter suppression, the reference model is selected to reflect the dynamics at a flutter free point in the flight envelope. An LQR is used to calculate the initial gains of the adaptive controller.

The airfoil model serves as the natural first step in understanding the adaptive control of aeroelastic systems. This system is simulated with linear torsional stiffness, nonlinear torsional stiffness, and freeplay. In addition, first-order and second-order actuator dynamics are implemented. Simulation studies showed that: both an MRAC and poorly tuned LQR are able to suppress the onset of flutter for the linear stiffness case; the LQR is unable to suppress LCO, unlike the MRAC; overall, the MRAC attenuates vibration more effectively than the LQR over a wide range of actuator bandwidths, but requires more aggressive control inputs; the performance of the MRAC is unaffected by the inclusion of second-order actuator dynamics or actuator freeplay.

The three-dimensional wing reinforces the results found in the airfoil simulations. The system is simulated at its flutter speed and its response to a vertical gust is evaluated. This includes the response with linear torsional stiffness, nonlinear torsional stiffness, and actuator freeplay. Simulation studies showed that an LQR and MRAC are able to suppress the onset of flutter but the MRAC is more robust to nonlinearities and freeplay.

The aircraft model is used to understand the effects of the flutter suppression system on rigid-body aircraft motion. Results show that flexible dynamics have little effect on the rigid-body dynamics due to the inertia of the aircraft and the differences in the frequencies at play. On the other hand, rigid-body motion does affect flexible dynamics as changes in aerodynamic forces lead to elastic deformations. The novel contributions of this work include:

1. A comprehensive study of the effectiveness of a model reference adaptive controller to suppress flutter in the presence of first-order and second-order actuator dynamics over a wide range of bandwidths, and actuator freeplay.
2. The development of an unsteady vortex-lattice solver for use in time-domain aeroelastic simulation of three-dimensional systems.
3. The application of direct model reference adaptive control to mitigate flutter in three-dimensional systems.

REFERENCES

[1] Bisplinghoff, R. L., Ashley, H., and Halfman, R. L., *Aeroelasticity*, Dover, 1996.

[2] Katz, J., and Plotkin, A., *Low-Speed Aerodynamics*, Cambridge, 2010.

[3] Scanlan, R. H., and Rosenbaum, R., *Aircraft Vibration and Flutter*, Dover, 1968.

[4] Flomenhoft, H. I., "A Method for Determining Mode Shapes and Frequencies above the Fundamental by Matrix Iteration," *Journal of Applied Mechanics*, Vol. 17, No. 3, 1950, pp. 249–256.

[5] Clough, R., and Penzien, J., *Dynamics of Structures*, Computers and Structures Inc., 2010.

[6] Theodorsen, T., "General Theory of Aerodynamic Instability and the Mechanism of Flutter," Tech. rep., NACA, 1936.

[7] Theodorsen, T., and Garrick, I. E., "Nonstational Flow About a Wing-Aileron-Tab Combination Including Aerodynamic Balance," Technical Report 736, NACA, 1942.

[8] Smilg, B., and Wasserman, L. S., "Application of Three-Dimensioal Flutter Theory to Aircraft Structures (With Corrections for the Effects of Control Surface Aerodynamic Balance and Geared Tab)," Tech. rep., Air Corps War Department, 1942.

[9] Bland, S. R., "Development of Low-Frequency Kernel-Function Aerodynamics for Comparison with Time-Dependent Finite-Difference Methods," Technical Memorandum 83283, NASA, May 1982.

[10] Ashley, H., and Zartarian, G., "Piston Theory - A New Aerodynamic Tool for the Aeroelastician," *Journal of the Aeronautical Sciences*, 1956.

[11] Albano, E., and Rodden, W. P., "A Doublet-Lattice Method for Calculating Lift Distributions on Oscillating Surfaces in Subsonic Flows," *AIAA Journal*, Vol. 7, No. 20, 1969, pp. 279–285.

[12] Edwards, J. W., "Unsteady Aerodynamic Modeling and Active Aeroelastic Control," Ph.D. thesis, Stanford University, Feb. 1977.

[13] Fung, Y. C., *An Introduction to the Theory of Aeroelasticity*, Dover, 2008.

[14] Corporation, M. S., *MSC Nastran 2017.1 Aeroelastic User's Guide*, 2017.

[15] Karpel, M., "Design for Active and Passive Flutter Suppression and Gust Alleviation," Contractor Report 3482, NASA, Nov. 1981.

[16] Hodges, D. H., and Pierce, G. A., *Introduction to Structural Dynamics and Aeroelasticity*, Cambridge, 2011.

[17] Etkin, B., and Reid, L. D., *Dynamics of Flight and Stability and Control*, John Wiley Sons, inc., 1996.

[18] Theodorsen, T., and Garrick, I. E., "Mechanism of Flutter a Theoretical and Experimental Investigation of the Flutter Problem," Technical Report 685, NACA, 1940.

[19] Haddadpour, H., and Firouz-Abadi, R., "Evaluation of quasi-steady aerodynamic modeling for flutter prediction of aircraft wings in incompressible flow," *Journal of Thin-Walled Structures*, Vol. 44, 2006, pp. 931–931.

[20] Roger, K. L., and Hodges, G. E., "Active Flutter Suppression - A Flight Test Demonstration," *Journal of Aircraft*, Vol. 12, No. 6, 1975.

[21] Buttrill, C. S., Zeiler, T. A., and Arbuckle, P. D., "Nonlinear Simulation of a Flexible Aircraft in Maneuvering Flight," , 1987.

[22] Behal, A., Marzocca, P., Rao, V., and Gnann, A., "Nonlinear Adaptive Control of an Aeroelastic Two-Dimensional Lifting Surface," *Journal of Guidance, Control, and Dynamics*, Vol. 29, No. 2, 2006.

[23] Nguyen, N. T., *Model-Reference Adaptive Control: A Primer*, Springer, 2018.

[24] Ko, J., Kurdila, A. J., and Strganac, T. W., "Nonlinear Control of a Prototypical Wing Section with Torsional Nonlinearity," *Journal of Guidance, Control, and Dynamics*, Vol. 20, No. 6, 1997, pp. 1181–1189.

[25] Andrighettoni, M., and Mantegazza, P., "Multi-Input/Multi-Output Adaptive Active Flutter Suppression for a Wing Model," *Journal of Aircraft*, Vol. 35, No. 3, 1998.

[26] Mattaboni, M., Quaranta, G., and Mantegazza, P., "Active Flutter Suppression for a Three-Surface Transport Aircraft by Recurrent Neural Networks," *Journal of Guidance, Control, and Dynamics*, Vol. 32, No. 4, 2009.

[27] Nguyen, N., and Hashemi, K., "Multi-Objective Flight Control for Ride Quality Improvement for Flexible Aircraft," *AIAA SciTech Forum*, 2020.

[28] Leatherwood, J. D., Dempsey, T. K., and Clevenson, S. A., "A Design Tool for Estimating Passenger Ride Discomfort withing Complex Ride Environments," *Human Factors*, 1980.

[29] Li, D., Xiang, J., and Guo, S., "Adaptive Control of a Nonlinear Aeroelastic System," *Aerospace Science and Technology*, Vol. 15, 2011, pp. 343–352.

[30] Zeng, Y., and Singh, S. N., "Output Feedback Variable Structure Adaptive Control of an Aeroelastic System," *Journal of Guidance, Control, and Dynamics*, Vol. 21, No. 6, 1998, pp. 830–837.

[31] Zhang, K., Marzocca, P., and Behal, A., "Adaptive Aeroelastic Control of a Nonlinear Airfoil with Multiple Flaps Under Unsteady Flow," *Journal of Vibration and Control*, Vol. 23, No. 10, 2017, pp. 1593–1606.

[32] Nguyen, N., Swei, S., and Ting, E., "Adaptive Linear Quadratic Gaussian Optimal Control Modification for Flutter Suppression of an Adaptive Wing," *AIAA Infotech @ Aerospace*, 2015.

[33] Downs, P. S., "Development of a State-Space Aeroelastic Model of a Flexbile T-tail Aicraft for Flutter Analysis," Master's thesis, Embry-Riddle Aeronautcial University, 2020.

[34] "Airworthiness Standards: Transport Category Airplanes," Title 14, Code of Federal Regulations § 25.341, 2024.

PUBLICATIONS

Downs, P., Greiner, G., and Prazenica, R., "State-Space Aeroelastic Model Development for Preliminary Design and Flutter Estimation," *AIAA Aviation*, 4 Aug. 2021.

Downs, P., Prazenica, R., "Adaptive Control of a Wing Planform for Flutter Suppression and Ride Quality Improvement," *AIAA SciTech*, 5 Jan. 2022.

Downs, P., Prazenica, R., "Adaptive Control of a Flexible Wing for Flutter Suppression and Disturbance Rejection," *AIAA SciTech*, 23 Jan. 2023.